



FACHBEREICH PHYSIK
BERGISCHE UNIVERSITÄT
WUPPERTAL

Investigation of clusters and precipitates in
reactor pressure vessel steels
by X-ray absorption spectroscopy

Sebastiano Cammelli

Dissertation zur Erlangung des Doktorgrades des
Fachbereichs Mathematik und Naturwissenschaften

in der Fachgruppe Physik
an der Bergischen Universität Wuppertal

Die Dissertation kann wie folgt zitiert werden:

urn:nbn:de:hbz:468-20131211-101625-6

[<http://nbn-resolving.de/urn/resolver.pl?urn=urn%3Anbn%3Ade%3Ahbz%3A468-20131211-101625-6>]

To Maddalena, Marianna e Alessandro

"Fatti non foste a viver come bruti,
ma per seguir virtute e canoscenza"
Dante Alighieri - Inferno - Canto XXVI

"Ihr seid bestimmt, nicht Tieren gleich zu leben,
Nein, Tugend zu erringen und Erkenntnis"

"Ye were not form'd to live the life of brutes,
But virtue to pursue and knowledge high"

Summary

The goal of the study is the investigation of the build-up of copper clusters in reactors pressure vessel (RPV) steels. The study comprises tests on RPV surveillance samples provided by a nuclear power plant, and on RPV reference samples. The reference steels, named Japanese Reference Quality (JRQ), were provided by the International Atomic Energy Agency (IAEA). Moreover the study was completed with the investigation of some unirradiated binary alloys.

To better understand the mechanism of cluster build-up in a simplified system, tests were performed on the binary alloy Fe-Cu containing 1.3 at % Cu. The samples were annealed at 775 K for different times. They were analysed using x-ray absorption fine structure (XAFS) spectroscopy at the Cu K-edge, x-ray diffraction (XRD) and transmission electron microscopy (TEM). The results show that Cu cluster formation occurs even with short annealing times. These clusters with a diameter of a few nm have been observed to switch easily from bcc Fe-like to fcc Cu-like structure. While a short annealing time of 2.5 h at 775 K does practically not change the good dilution of Cu in the bcc Fe matrix, an annealing treatment for 312 h leads to large fcc Cu precipitates. A linear combination analysis suggests that in the sample annealed for 8 h, Cu clusters are formed mostly in the same structure as the bcc matrix. A coexistence of bcc and fcc clusters is obtained for 115 h of annealing. TEM indicates the presence of precipitates with a diameter up to 60 nm for an annealing time of 312 h, and XRD provides complementary data about the clusters size distributions in differently annealed samples.

The reactor pressure vessel (RPV) reference steel from IAEA submitted to neutron irradiation in a research reactor and subsequently thermally annealed and re-irradiated was investigated by XAFS spectroscopy. It could be expected that Cu and Ni atoms form nano-clusters. In the unirradiated sample and in the irradiated sample no significant clustering is detected. In all irradiated and subsequently annealed samples an increase of Cu and Ni atom densities are recorded around the x-ray absorbing atoms. Furthermore, the density of Cu and Ni atoms determined in the first and second shell around the absorber is found to be affected by irradiation and the annealing treatment. The comparison of the XAFS data at the Cu and Ni K-edges shows that these elements are in a bcc structure like the Fe host lattice. However, the local irradiation damage reduces the number of next neighbour atoms around copper; while the annealing reduces the number of vacancies. The number of Cu and Ni atoms around (Cu or Ni) absorbers then increases. The IAEA samples are very well characterised due to earlier analysis by atom probe tomography (APT) at the Oak-Ridge National Lab (ORNL) and mechanical tests, at the Paul Scherrer Institut. The possibility to compare XAFS and APT provided an invaluable opportunity to understand the differences and similarities among the two techniques. XAFS and APT are both very sensitive to nanostructures and both are element selective techniques. XAFS is highly sensible to the average environment of the absorber element, within < 0.5 nm, so it delivers information about the short range order. The results show a general agreement and the differences were considered within the experimental error.

Finally, surveillance samples from a Swiss nuclear power plant (KKG Kernkraftwerk Gösgen) were analysed by XAFS. The number of Cu and Ni atoms determined in the first and second shell around the absorbers is affected by irradiation and temperature. The comparison of the EXAFS data at the Cu and Ni K-edges shows that these elements are

in a crystallographic structure similar to bcc Fe. There are indications that the formation of Cu and Ni clusters differs significantly; irradiation damage reduces the next neighbour number for both elements. Clusters were detected only around copper atoms: the number of Cu atoms in the first two shells was found to increase with the irradiation time.

With EXAFS it could be verified that neutron irradiation in a power reactor leads to small changes of the local atomic environment around the investigated Cu and Ni atoms.

Moreover, most of the local structural changes are obtained for the sample with the longest irradiation time. This lets assume that the reduction of the number of next neighbours in the bcc structure around Cu and Ni in the steel matrix is steadily increasing with the years of irradiation in the reactor. However it can be expected that the elevated temperature helps refilling the irradiation induced vacancies by a permanent annealing process. The detailed EXAFS analysis has demonstrated that the number of Cu atoms in the local vicinity of copper is enriched during irradiation in the power plant, while the local atomic environment around nickel seems to be less affected.

Cu and Ni atoms behave similarly in the IAEA samples, but they show differences in the power reactor samples. The reasons for the different behaviour reside in the different irradiation processes: IAEA samples were strongly irradiated and then annealed at high temperature, while the KKG samples were irradiated at a higher temperature than the IAEA samples without any post irradiation annealing. Obviously neutron irradiation forms many vacancies and vacancies clusters, which are easily filled by solute atoms. In case of irradiation in the power reactor, there are fewer vacancies and the temperatures involved are lower than the annealing temperature of the IAEA reference samples; the atom cluster formation of Cu is slowed down and Ni is even less affected.

Zusammenfassung

Das Ziel dieser Studie ist die Untersuchung der Bildung von Kupferclustern in Reaktordruckbehälterstählen (RPV). Die Studie beinhaltet RPV Überwachungsproben, Proben des IAEA RPV-Referenzstahls mit verschiedenen Bestrahlungs- und Temperungsstadien (JRQ) und Modelllegierungen mit verschiedenen thermischen Behandlungen.

Um den Mechanismus der Clusterbildung in einem vereinfachten System besser zu verstehen zu können, wurde eine FeCu-Legierung mit 1.3 at.% Cu untersucht. Die Proben wurden bei 775 K für verschiedene Zeiten getempert. Sie wurden mit Hilfe von Röntgenabsorptionsspektroskopie (XAFS) an der Cu K-Kante, der Röntgenbeugung (XRD) und Transmissionselektronenmikroskopie (TEM) analysiert. Die Resultate zeigen, dass Cu-Cluster sogar nach kurzer Temperung auftreten. Die einfache Umwandlung dieser Cluster mit einem Durchmesser von einigen Nanometern von der kubischraumzentrierten (bcc) Eisenstruktur zu der kubischflächenzentrierten (fcc) Cu-Struktur wurde beobachtet. Während eine kurzen Temperung von 2.5 h bei 775 K die gute Dispersion der Kupferatome in der bcc Eisenmatrix nicht ändert, führt eine Temperung für 312 h zu großen fcc Cu-Ausscheidungen. Eine lineare Kombinationsanalyse legt nahe, dass in der Probe, die für 8 h getempert wurden, Cu-Cluster meistens mit der gleichen Kristallstruktur wie die bcc Matrix gebildet werden. Eine Koexistenz von bcc und fcc-Clustern wird für 115 h Temperung erreicht. Die Existenz von Ausscheidungen mit einem Durchmesser bis 60 Nanometer während einer Glühdauer von 312 konnte im TEM beobachtet werden und XRD lieferte ergänzende Details über die Clustergrößenverteilungen in verschiedenen getemperten Proben.

Der in einem Forschungsreaktor neutronbestrahlte und danach getemperte und wiederbestrahlte Referenzstahl für Reaktordruckbehälterstähle (RPV) der IAEA wurde mit Hilfe Röntgenabsorptionsspektroskopie untersucht. Es kann angenommen werden, dass Cu- und Ni-Atome Nanocluster bilden. In der unbestrahlten Probe und der bestrahlten Probe wurde keine bedeutende Clusterbildung beobachtet. In allen bestrahlten und danach getemperten Proben wurde eine Zunahme der Cu- und Ni-Dichte um die untersuchten Atome festgestellt. Außerdem wurde ein Einfluss der Bestrahlungs- und Temperbehandlung auf die Dichte der Cu- und Ni-Atome in der ersten und zweiten Schale beobachtet. Der Vergleich der XAFS Daten an den Cu und Ni K-Kanten zeigt, dass diese Elemente in einer bcc Struktur wie der Fe-Matrix sind. Jedoch verringert der lokale Bestrahlungsschaden die Zahl der Nachbaratomen um Kupfer; während das Tempern deren Anzahl wieder erhöht. Die IAEA-Proben wurden bereits sehr gut durch frühere Analyse mit Hilfe von Atomsondentomographie (APT) am Oake-Ridge National Lab (ORNL) und an den mechanischen Tests am Paul Scherrer Institut charakterisiert. Der Vergleichs von XAFS und APT bietet eine gute Möglichkeit, die Unterschiede und die Gemeinsamkeiten der beiden Techniken zu verstehen. XAFS und APT sind beide in der Lage Nanostrukturen aufzulösen, sind elementspezifisch. XAFS ist in der Lage die durchschnittliche Umgebung des Absorberatoms in weniger als <0.5 nm zu charakterisieren, also die kristalline Nahordnung. Die Ergebnisse zeigen eine generelle Übereinstimmung, die Unterschiede wurden als innerhalb des experimentellen Fehlers liegend eingestuft.

Auch Überwachungsproben von einem Schweizer Atomkraftwerk (KKG Kernkraftwerk Gösgen) wurden mit Hilfe von XAFS analysiert. Die Anzahl der Cu- und Ni-Atome in der ersten und zweiten Schale um den Absorber wird durch die Bestrahlung und Temperatur beeinflusst. Der Vergleich der EXAFS Daten an den Cu und Ni K-Kanten zeigt, dass diese Elemente in einer kristallographischen Struktur sind, die ähnlich zu bcc Eisen ist. Es gibt Anzeichen für einen erheblichen Unterschied der Bildung der Cu- und Ni-Cluster; Bestrahlungsschäden verringern die Anzahl der Nachbaratome für beide Elemente. Cluster wurden nur für Kupfer gefunden: Die Anzahl der Cu-Atome in den ersten zwei Schalen nahm mit der Bestrahlungszeit zu. Mit EXAFS konnte bestätigt werden, dass die Neutronbestrahlung in einem Leistungsreaktor zu kleinen Veränderungen des lokalen Atomumfelds um die untersuchten Cu- und Ni-Atome führt. Die größten lokalen Strukturveränderungen wurden für die Probe mit der längsten Bestrahlungszeit beobachtet. Dies lässt den Schluss zu, dass die Verringerung der Anzahl der Nachbaratome in der bcc Struktur um Cu- und in Ni-Atome in der Stahlmatrix sich ständig mit der Bestrahlungszeit im Reaktor erhöht. Jedoch kann angenommen werden, dass die erhöhte Temperatur dazu beiträgt, die durch Bestrahlung erzeugten Leerstellen durch einen dauerhaften Temperprozess wieder zu füllen. Die ausführliche EXAFS Analyse hat gezeigt, dass die Anzahl der Cu-Atome in der unmittelbaren Nähe der Cu-Atomen während der Bestrahlung im Kraftwerk ansteigt, während das lokale Umfeld um Nickel weniger beeinflusst zu werden scheint.

Cu- und Ni-Atome zeigen ein ähnliches Verhalten in den IAEA-Proben, aber ein unterschiedliches in den Leistungsreaktorproben. Die Gründe für das unterschiedliche Verhalten sind die verschiedenen Bestrahlungsprozesse: IAEA-Proben wurden stark bestrahlt und dann bei hohen Temperaturen getempert, während die KKG Proben bei einer höheren Temperatur als die IAEA-Proben ohne ein nachgeschaltetes Tempern bestrahlt wurden. Offensichtlich bewirkt Neutronbestrahlung die Bildung vieler Leerstellen und Leerstellencluster, die leicht durch gelöste Legierungselemente gefüllt werden. Im Falle der Bestrahlung im Leistungsreaktor, gibt es weniger Leerstellen und die Temperaturen, sind niedriger als die Tempertemperatur der IAEA-Referenzproben; die Clusterbildung von Kupfer wird verlangsamt und Ni ist noch weniger betroffen.

Content

1. Introduction.....	13
1.1 Motivation.....	13
1.2 Method.....	13
1.3 Structure of the thesis.....	14
2. Background	15
2.1 Material.....	15
2.2 Analysis	15
2.2.1 Macroscopic approaches	15
2.2.2 EXAFS.....	18
2.2.3 EXAFS analysis of (Fe,Cu) model alloys.....	18
2.2.4 XAFS analysis of (Fe,Cu), (Fe,Cu,Mn), (Fe,Cu,Ni).....	19
2.2.5 APT studies of RPV.....	19
2.2.6 PAS studies of RPV.....	21
2.2.7 SANS studies of RPV.....	22
3. Theory	23
3.1 Materials.....	23
3.1.1 Matrix damage.....	23
3.1.2 Homogeneous cluster model.....	24
3.1.3 Particles, clusters and precipitates.....	25
3.1.4 Heterogeneous cluster model.....	27
3.1.5 Cluster size distribution	28
3.2 X-ray absorption fine structure (XAFS)	30
3.2.1 X-ray absorption and matter.....	30
3.2.2 Absorption coefficient and threshold energy E_0	33
3.2.3 The EXAFS spectrum.....	34
3.2.4 Free mean path $\lambda(k)$	34
3.2.5 Thermal disorder, Debye Waller factor.....	35
3.2.6 $\tilde{\chi}(R)$: the Fourier transform of $\chi(k)$	35
3.2.7 Quality factor.....	35
3.3 Limit of XAFS spectroscopy.....	36
3.3.1 Temperature consideration: anharmonic corrections...36	
3.3.2 Polydispersity.....	37
4. Experimental	38
4.1 Studied samples.....	38
4.1.1 Binary alloy samples	38
4.1.2 JRQ samples	38
4.1.3 Kernkraftwerk Gösgen (KKG) samples.....	39

4.2 Samples Analysis.....	40
4.2.1 EXAFS at ANKA (FKZ)	40
4.2.2 EXAFS at SLS (PSI)	40
4.2.3 TEM at LNM (PSI)	42
4.2.4 XRD at SLS (PSI)	42
4.2.5 Software	43
5. Results.....	44
5.1 Binary alloy	44
5.1.1 EXAFS results	44
5.1.2 TEM and EDS analysis.....	47
5.1.3 XRD data analysis and simulations.....	48
5.2 JRQ samples: matrix damage.....	49
5.2.1 Atomic environment around Fe	50
5.2.2 Atomic environment around Mn, Ni and Cu.....	51
5.3 JRQ samples: cluster formation.....	55
5.3.1 XANES: Cu and Ni K-edge.....	55
5.3.2 EXAFS: Cu K-edge.....	56
5.3.3 EXAFS: Ni K-edge.....	57
5.4 KKG samples: cluster formation.....	58
5.4.1 XANES: Cu and Ni K-edge.....	58
5.4.2 EXAFS: Cu K-edge.....	59
5.4.3 EXAFS: Ni K-edge.....	61
6. Discussion	63
6.1 Binary alloy	63
6.1.1 Comparison of precipitate and size distribution.....	63
6.2 RPV steel	65
6.2.1 JRQ samples (EXAFS and APT)	65
6.2.2 RPV cluster size distribution.....	66
6.2.3 Post annealing treatment.....	67
6.2.4 KKG samples: effect of irradiation at 575 K.....	68
6.3 Key questions.....	71
6.3.1 Do very small aggregates already exist in the as received, solution (...)?.....	71
6.3.2 How do the precipitates form (solid solution \Rightarrow small clusters \Rightarrow precipitates)?	72
6.3.3 How do other atoms, e.g. Ni, Mn, influence the formation of the Cu precipitates?	72
6.3.4 How do the precipitates behave on post-irradiation thermal annealing and re-irradiation?	73

6.3.5 What is the limiting size and concentration of aggregates-precipitates markedly affecting the mechanical proprieties?	74
7. Conclusion.....	75
8. References	78
9. Variable indexes and symbols.....	85
10. Acknowledgements	88
11. Curriculum Vitae	89

1. Introduction

1.1 Motivation

In nowadays society, the energy demand is increasing. One of the key strategies to deal with energy concerns the prolongation of the lifetime of the nuclear reactor park. This strategy requires agreement from the authorities. The regulatory organizations are concerned by safety of the power plants and regulations are consequently required to ensure reactor operation in a safe way.

During operation the reactor pressure vessel (RPV) of light water reactors is subjected to factors which lead to aging of the ferritic steel structures. Besides high temperature and high pressure, neutron irradiation is the main reason for material degradation. With the increase of the operation time, the ability of the steel to absorb impact energy decreases and the temperature for the ductile-brittle transition rises. This shift may lead to a situation where the safe operation of a nuclear power plant during transients can be affected. The reason for the ductile-brittle transition temperature shift (ΔT_{DBT}) can be found in the specific micro-structural deformation behaviour of ferritic steels and in the formation of small clusters of alloying elements hindering ductile deformation [1].

Today, running research activities on reactor pressure vessel (RPV) steel aging concern the influence of the chemical composition on the formation of irradiation induced micro-structural changes and the embrittlement behaviour [2].

This thesis concerns RPV steel and the analysis of the atomic environment of the main constituents with a special regard on Cu and Ni atoms.

In this work the role of Cu and Ni in the cluster formation under different conditions of neutron irradiation and annealing treatment has been investigated as well as the production of interstitials and vacancies. These key features impact on the mechanical properties of the steel.

1.2 Method

Many experimental techniques have been applied to investigate RPV steels. These analytical techniques can be compared for their performance/detection limit in term of size and the order of magnitude of the clusters/precipitates concentration that can be detected. Transmission electron microscopy (TEM), positron annihilation spectroscopy (PAS), small angle neutron scattering (SANS) and atom probe tomography (APT) are the most applied experimental techniques. Their limitations are presented in Chapter 2.

Even if studies on RPV steels started during the 80s, nowadays there is the possibility to perform high quality measurements using third generation synchrotrons, facilities that can provide a very high flux of photons on a very small surface. X-ray absorption spectroscopy (XAS) is the experimental technique chosen to investigate the clusters evolution in RPV steels. This experimental technique has been chosen for different reasons: it is a selective technique, so it is possible to investigate the environment around the absorber atoms (Cu and Ni); it is a short-range technique, so it helps to detect small structures as nanoclusters, it is not destructive, so the samples are not damaged and modified during the experiments. Moreover, the theory of XAFS and the software for the data analysis had an enormous progress in the last two decades and this technique has never been applied to real irradiated RPV steels.

1.3 Structure of the thesis

The thesis is divided in seven Chapters. In the first, a short introduction is provided.

In the Chapter 2, the degradation of RPV steels is introduced through the variation of two parameters: the ductile to brittle transition temperature (DBTT) and the toughness. Moreover a detailed description of the main results found in literature by experimental analysis is presented. At the beginning some semi-empirical studies are introduced with the aim to connect some macroscopic information (i.e. solute concentration, neutron fluence) to the DBTT. Then some preliminary results obtained by XAFS on a binary alloy are presented. Some important results obtained by APT, PAS and SANS, found in literature, are shown with a special regard to the limitation of the experimental techniques.

Chapter 3 concerns the applied theory: in the first part are introduced the main characteristics of the solid solution and the model used by EXAFS to evaluate the presence of clusters and precipitates. Two models are described: the first is used in case of fcc clusters embedded in bcc matrix, the second is applied for bcc clusters in a bcc matrix and it is used even to quantify the presence of vacancies near the absorber atoms. X-ray diffraction (XRD) was used for the inactive samples and a brief description of the method used to calculate the cluster size distribution, based on the XRD patterns, is given.

In the second part of Chapter 3, a detailed description of XAFS spectroscopy and its limitations is given.

In Chapter 4 experimental details are given. The inactive and the active samples are introduced as well as the beamline Micro-XAS, where most of the experiments were performed.

Chapter 5 concerns the results of the thesis: the inactive samples show a phase change, which is investigated by XAFS, TEM/EDS and XRD. In the active samples, the matrix damage and the cluster formation of solute atoms is described in detail. Moreover it is shown how the behavior of Cu and Ni atoms depend on the neutron irradiation and on the annealing time and temperature.

Chapter 6 deals with the discussion of the results and the comparison with other literature studies with special regard on cluster size distribution.

In Chapter 7 the conclusions are reported.

2. Background

This chapter provides a first look at the properties of the material analyzed and at the experimental techniques used to analyze reactor pressure vessel (RPV) steel with a special regards to the few XAFS publications on binary and ternary alloy. It has to be reminded that before this work, XAFS spectroscopy has never been applied at RPV steel.

2.1 Material

RPV steels are iron alloys which present at least the 2-3 at % of solute elements. Many elements are diluted in the Fe matrix in order to improve the properties of the steel. The distribution of these impurities in the iron matrix is affected by the neutron irradiation and by the high temperature of the reactor, and changes can modify tremendously the life time of the steel.

With the increase of the operation time, the ability of the steel to absorb impact energy decreases; a decrease of the toughness of the steel is expected. A second important parameter is the ductile-brittle transition temperature shift (ΔT_{DBT}) that rises with the operation time. The increase of ΔT_{DBT} and the loss of toughness are strictly connected and in general the main consequence is a worsening of the mechanical proprieties of the steel, thus a dumping of the potential operation time of the reactor.

High temperature and neutron irradiation are the main reason for material degradation. Qualitatively the variation of the ductile to brittle temperature T_{DBT} might be associated to the total damage that affects the steel during the operation. In a simplified system the total damage can be considered as composed of two independent components: the first is the matrix damage is due to the irradiation; the second depends on the precipitation formation. As it is shown in the next pages these two components are not purely independent: the matrix damage and the presence of vacancies help the precipitates formation.

2.2 Analysis

Many different experimental techniques have been applied to RPV studies in the past. It is possible to divide the literature in two branches according whether the techniques are macroscopic or micro/nano-scopic oriented. In the first branch the main issue is the calculation of the ductile to brittle transition temperature shift (ΔT_{DBT}) or of the fracture toughness of the material; basically these experiments involve techniques enable to obtain information on the microstructures, e.g. the measure of the Seebeck coefficient [3]. An attempt to connect ΔT_{DBT} to the neutron fluence, the thermal treatment and the concentration of the solutes elements was performed by Debarberis *et al.* through a semi-empirical approach and it is introduced in section 2.2.1.

In the second approach the used techniques are able to obtain important information about micro-nano structures. These techniques present some limitations thus it is suggestible to combine them as it was performed for positron annihilation spectroscopy (PAS) and small angle neutron scattering (SANS) [4], PAS and atom probe tomography (APT) [5], transmission electron microscopy (TEM) and PAS [6], APT and SANS [7], and ATP, PAS, SANS and TEM [8, 9]. In this Chapter it is given a brief description of some results obtained with a macroscopic and micro-nano approach.

These analytical techniques are compared for their performance/detection limits in term of size and the order of magnitude of the clusters/precipitate concentration that can be detected. The comparison is extended for EXAFS and it is shown in Table 2.1.

Table 2.1

The diameter and the precipitate density of the smallest detectable clusters for each technique commonly used to investigate RPV.

Detection lower limits	Diameter [nm]	Precipitates density [cm ⁻³]
TEM	~ 1	~ 10 ¹³
PAS	~ 0.6	~ 10 ¹⁴
SANS	~ 1.2	~ 10 ¹⁵
ATP	~ 0.5	~ 10 ¹³
EXAFS	0.2 – 0.7	~ 10 ¹⁵

Table 2.1 needs more explication because the limits of the respective techniques are actually not so well defined. Transmission electron microscopy for instance is able to image small clusters with the size indicated in Tab 2.1, but only if clusters and matrix are composed of elements with a significantly different atomic number Z in order to increase the contrast. PAS is suit to detect vacancy-defects, but clusters are more difficult to be detected and some results are doubtful (see Section 2.2.6). By SANS investigations it is possible to determine cluster size, composition and density, but clusters need to be larger than a nm. Although only a limited fraction of atoms can be detected (the efficiency is ~ 60 % in a certain volume), ATP is one of the most promising technique for the determination of the cluster size and density but it cannot detect vacancies. EXAFS limitations are discussed in detail in Chapter 3.

2.2.1 Macroscopic approaches

Here two studies are presented. In the first the mechanical degeneration of the RPV is due to different interaction mechanisms such as [10]:

1. Neutron and gamma rays interaction,
2. Thermal treatments,
3. Different composition: variation of Cu, Ni and P. The effect of irradiation and thermal treatment is stronger if the concentration of these elements is larger.

Strong neutron irradiation causes large atom cascade: many atoms change their positions and many pair defects (interstitial atoms and vacancies) are produced. Typically the recombination rate is strong, but it is worth to point out that neutron irradiation at low energy is not less dangerous because the recombination is definitely lower. The matrix damage increases constantly with the fluence. The recombination is clearly dependent on thermal treatments: high temperatures and prolonged treatments are needed to recover matrix damages.

For a given exposure, Cu, Ni and P are recognized to be the most deleterious element for the degradation of the mechanical proprieties. Many equations have been found empirically to connect the Cu and P concentration and the damage of the neutron fluence to the variation of ΔT_{DBT} . These equations were updated including even the Ni concentration. The equations are:

$$CF = [P + 0.07Cu] \times [Ni - 0.1]^a + b \quad (2.1)$$

$$\Delta T_{DBT} = CF \times F^{1/3} \quad (2.2)$$

ΔT_{DBT} is the ductile to brittle transition temperature shift, CF is the chemistry factor, F is the neutron fluence ($E > 0.5$ MeV), P , Cu and Ni are the phosphorous, copper and nickel concentrations respectively. Note that these equations were tested only a little number of samples that have the same characteristic as RPV steels (~ 30) and it was verified that it gives a good estimations even on real RPV steels.

The increasing of the ΔT_{DBT} with the concentration of Ni was found to be linear if the concentration of Ni atoms is below 1.1 at %; over this limit the effect of Ni impurity becomes very strong and needs to be reconsidered. Fortunately most of the RPV materials do not have such large Ni concentration.

It should be noted that this linearity is valid for any Cu concentration (≤ 0.4 wt %) (see Fig 2.1).

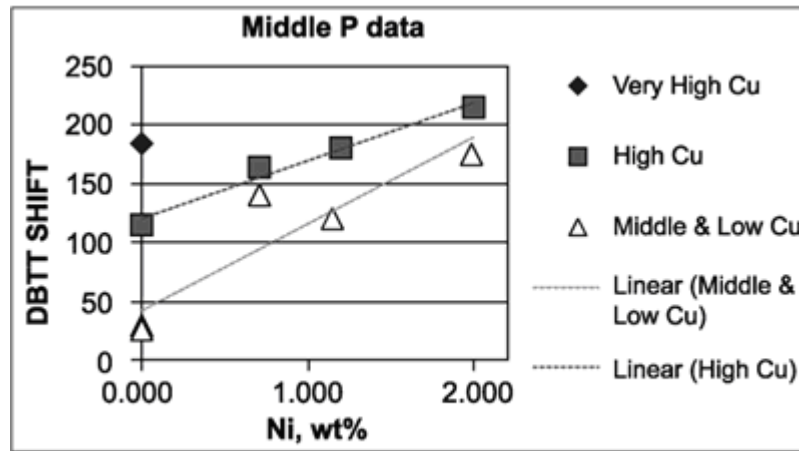


Figure 2.1: The variation of T_{DBT} shift vs the weight percentage of Ni atoms in the RPV steel for different percentage of Cu. Obtained from Debarberis *et al.* [10], note that middle and low Cu refers to a percentage between 0.005 wt % and 0.1 wt %, high Cu means 0.4 wt %, very high Cu means 1 wt %.

From Fig 2.1 the linear proportion between the Ni concentration and the increasing of ΔT_{DBT} for a given Cu concentration is expected. This linearity is valid for the Cu and Ni concentration of the RPV steels analyzed herein.

The second example [11] is based on some slightly different assumptions and is an attempt to provide a quantitative description of the different embrittlement mechanisms. Three different reasons are discussed:

1. Matrix damage (cascades, vacancies, interstitials, dislocation rings)
2. Irradiation induced clusters or precipitations (comprising Cu, Ni and/or Mn)
3. Segregations (P-segregations on grain boundaries are very important)

In [11] the shift of the ductile to brittle transition temperature ΔT_{DBT} is described as depending on the mentioned factors and the neutron fluence F . Basically ΔT_{DBT} is considered as composed of three factors, one for each point. The shift of ΔT_{DBT} due to the matrix damage is called $\Delta T_{DBT-Matrix}$. Copper plays an important role in cluster formation because its solubility is very low ($\sim 0.007\%$ [12]) in pure iron at the typical irradiation and

temperature of reactor. It can lead, even in the case of very low Cu contents, to unexpected large Cu clusters and the increasing of the ΔT_{DBT} due to Cu precipitates is called $\Delta T_{DBT-Cu-Precipitate}$. Phosphorus segregates from the matrix on the grain boundaries forming some nano-clusters. Cu is generally reputed more dangerous than phosphorous even because its concentration is much higher. The shift of the ΔT_{DBT} due to the phosphorous is called $\Delta T_{DBT-P-Segregation}$.

The precipitation and segregation part of the embrittlement go into saturation with increasing fluence while the matrix damage rises slower and continuously. The semi-mechanistic description is as follows:

$$\Delta T_{DBT-Matrix} = a \cdot F^m \quad (2.3)$$

$$\Delta T_{DBT-Cu-Precipitates} = b \cdot (1 - e^{-F/F_{sat}}) \quad (2.4)$$

$$\Delta T_{DBT-P-Segregation} = c \cdot \left[0.5 + 0.5 \cdot \tanh\left(\frac{F - F_{start}}{d}\right) \right] \quad (2.5)$$

The advantage of this description is that it includes the different kinds of embrittlement in RPV steels depending on the fluence [13]. Additionally it delivers interesting explications for the re-irradiation behaviour. A drawback concerns the use of many parameters (a , b , c , d , m , F_{sat} , F_{start}) that only partially have a physical meaning as, for instance, F_{start} the starting fluence for P segregation. Some of the parameters depend on the chemical composition. In [14, 15] the results are correlated with the change of mechanical properties. In another publication [16] the semi-mechanistic model is further developed and takes into account also RPV welds steel.

All these formulas and methods point out the importance of some elements (Cu, Ni, P...) and of some phenomena, such as neutron fluence. Nevertheless, these formulas are semi-empirical equations and they do not seem to provide complete and exhausting explications of the relation between the formation of nano-structures (i.e. nano-clusters) and the ΔT_{DBT}

2.2.2 EXAFS

Two studies are introduced in this section, the first concern a preliminary study performed on a binary alloy Fe-Cu and it is presented in 2.2.2 [17]. The second concerns some binary, ternary and quaternary alloy [18].

2.2.3 EXAFS analysis of (Fe,Cu) model alloys

A preliminary experiment has been performed on a binary alloy Fe Cu in order to verify the capability of EXAFS on such diluted samples. The samples were prepared at the SCK-CEN, Mol Belgium and more detailed information can be found in Ref [17]. After alloying to the desired compositions, they were pre-annealed for 4 hours under argon ambient at 1075 ± 5 K and then quenched in water from the annealing temperature.

Three samples have been analyzed and their composition is reported in Tab 2.2. One of them was annealed at 775 ± 5 K for 1 h and then quenched to room temperature. Here only the data at the Cu K edge are discussed.

The collected data have been analyzed with two different models. In the first the only Fe atoms surround the absorber. This approximation, which might look rough, can provide reliable results only if the Cu atoms are perfectly diluted in the matrix, thus their contribution in the first and second shell around the Cu absorbers is expected to be not

significant. The second model foresees the presence of Fe and Cu atom in the environment. These elements are weighted by a parameter ‘x’, which provides a quantitative evaluation about the presence of Cu atoms around Cu absorbers.

Table 2.2

The main results from [17], the importance of Cu atoms in the first shell around Cu absorber increase significantly. The sample named Fe-1.0 wt % Cu An was annealed at 775 ± 5 K for 1 h before been quenched. There are 8 atoms in the first shell of a bcc solid.

	Fe-0.3 wt % Cu	Fe-1.0 wt % Cu	Fe-1.0 wt % Cu An.
Cu-Fe paths ($\pm 10\%$)	7.4	6.9	6.7
Cu-Cu paths ($\pm 10\%$)	0.8	1.1	1.4

The quality of the two applied model was evaluated by the \mathcal{R} quality factor [19] and it has been shown that the model that involves both Cu and Fe atoms, gives much better results. The discrepancy between the two models becomes larger increasing the Cu content in the sample or submitting the sample to an annealing treatment.

Moreover EXAFS spectroscopy showed to be sensitive to small changes in the atomic environment and that no crystalline phase changes are expectable.

2.2.4 XAFS analysis of (Fe,Cu), (Fe,Cu,Mn) and (Fe,Cu,Ni)

This section is mostly based on the study performed by Maury *et al.* [18]. In this study some iron alloy are investigated with a high percentage of solute, compared to the RPV alloys. Many binary and ternary samples are analyzed with different concentrations: Cu percentage is between 1.26 and 1.50 ± 0.04 at %, Mn is around 1.37 at % and Ni is around 1.5 at %. For each composition a series of samples is annealed at different temperatures in order to investigate the formation of clusters. The main results of this work are found from the analysis of the XANES spectra: at the Cu K edge, a progressive change from the typical bcc structure of the Fe matrix to the structure of the Cu bulk is observed in the binary (Fe,Cu) and in the ternary alloys (Fe,Cu,Mn) and (Fe,Cu,Ni). This means that the phase change from bcc to fcc is expected. The analysis of the Mn and Ni K edges revealed that the XANES spectra do not change with the increase of the annealing time. This means that these elements are expected to not take a part in the cluster formations and they are considered as in solid solution. Nevertheless their role is far to be merely passive: the ternary alloys showed a portion of fcc significantly larger than the binary (Fe,Cu).

These promising results point out a difference between the behaviour of solute elements. Unfortunately the EXAFS analysis could not provide results more precisely because of the quality of the data collected. Since the understanding of the phase change from bcc to fcc is not completely clear, the high quality of the samples produced and the enormous development of XAFS in the last decades, some binary alloy (Fe 1.34 at % Cu, annealed 2.5, 8, 115, 312h) have been analyzed during this thesis by XAFS, TEM/EDS and XRD. Their description and the gained results are introduced in details in the following chapters.

2.2.5 APT studies on RPV.

Atom probe tomography (APT) is one of the most applied techniques to investigate RPV steels. Binary (Fe Cu alloy), ternary or RPV steels were analyzed intensively by APT

because this experimental technique is particularly suited to identify cluster density and the cluster composition profile.

The first study presented here was performed on a binary alloy Fe 0.1 wt % Cu ion irradiated [20]. In order to verify the clustering dynamics, three different kind of irradiation were performed: electrons irradiation (energy: 3 MeV; fluence: $5 \times 10^{24} \text{ m}^{-2}$), Fe^+ (150 keV, from 8.5×10^{15} to $1.2 \times 10^{18} \text{ m}^{-2}$) and He^+ (1 MeV, $6.5 \times 10^{20} \text{ m}^{-2}$) ion irradiations were used to produce displacement cascades (DC) during the collisions.

Different intensities of DC were produced because they are responsible of a high number density of point defect clusters. It was verified that electron irradiation is not suited to produce DC and no clusters were found. Ion irradiation produces DC and Cu clusters appear only if radiation is able to produce an enough high number of defect clusters [20]. Another studies performed on real RPV steel by APT [21] pointed out the atomic distribution of the clusters on a weld and forging materials. The composition of the weld material and the atomic distribution in a cluster are represented in Table 2.3 and Fig 2.2.

Table 2.3

The composition of the weld material of the [21], the Cu concentration is 2 and 3 times larger than the RPV samples analyzed in this thesis.

	Cu	Ni	Mn	Si	P	C	S	Mo	Cr
Weld at %	0.24	0.56	1.5	1.01	0.03	0.42	0.03	0.23	0.06

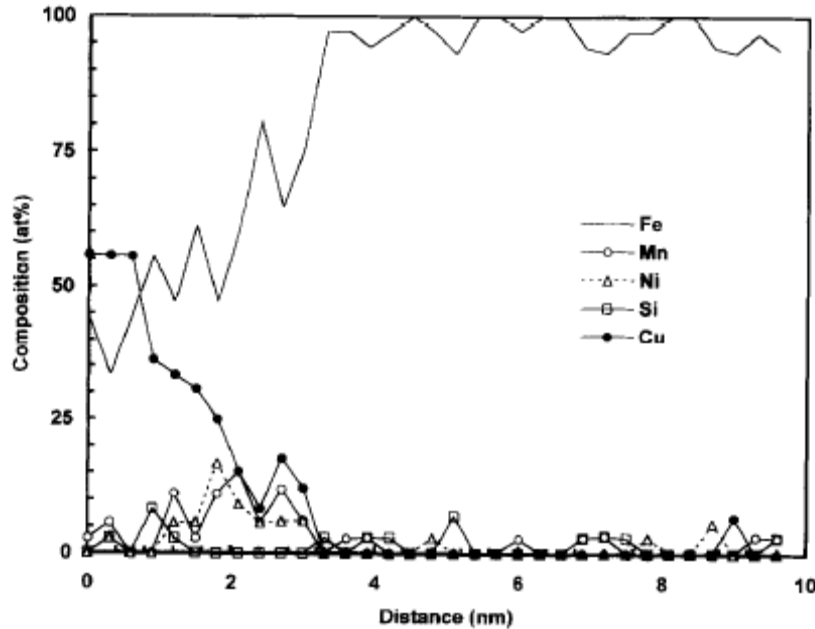


Figure 2.2: Composition profile through a portion of the copper cluster. The weld material was neutron irradiated ($3.5 \times 10^{19} \text{ cm}^{-2}$, $E > 1 \text{ MeV}$) and annealed (168 h, 725 K) [21].

It was observed that clusters have a high percentage of Cu atoms in the core. The amount of Cu decreases quickly and consequently the percentage of Fe increases. The cluster shows also a region, between 1.7 and 3.5 Å, where there is a significant amount of Ni and Mn atoms. The density of clusters was $\sim 10^{23}$ and $\sim 3 \times 10^{23} \text{ m}^{-3}$ after a neutrons fluence of 6.6×10^{19} and $3.47 \times 10^{19} \text{ per cm}^{-2}$. The composition of the clusters is independent by the

fluence. It is important to note that the cluster shown in Fig 2.2, with a diameter larger than 6 nm, has the same crystallographic structure of the matrix.

2.2.6 PAS studies on RPV

Positron annihilation spectroscopy (PAS) is applied intensively to RPV steels and similar alloys because it is sensitive to defects above all open-volume region in a material [22] as well as the chemical identity of the elements at the annihilations site [23]. The two works briefly presented here [24, 25] are an attempt to provide an overview on the combination of vacancies and solute atoms.

In the first work [24] some binary alloy (Fe, Cu) with different copper content (0.04 at %, 0.13 at % and 0.27 at %) were neutron irradiated ($8.3 \times 10^{18} \text{ cm}^{-2}$ which corresponds to 20 years for RPV in the pressurized water reactors) and then analyzed. In all the samples was found a strong aggregation between Cu atoms and vacancies: the vacancies are surrounded almost completely by Cu atoms (94 %, 92 % and 80 % for the 0.3 wt %, 0.15 wt % and 0.05 wt % samples respectively). It is interesting because all the samples showed clusters only after the irradiation (performed at 375 and 575 K) and none after the previous annealing treatment (4 h, 1100 K). Nagai *et al.* [24] affirm also that no clusters appear in the Fe 0.3 at % Cu sample annealed 312 h at 825 K, but this result is doubtful considering a study performed on similar samples presented in Chapter 5. In this study Nagai *et al.* verified that the widely accepted conditions for the post irradiation annealing treatment [26] (168 h, 730 K) are not enough. One of the most important results of Nagai *et al* concerns the temperature of the post irradiation annealing treatment: microvoids (aggregation of vacancies) disappear with an annealing treatment of 675 K. Copper precipitates recovery depends on the copper concentration: for the sample Fe 0.04 at % Cu it is at 875 K for the Fe 0.27 at % it is at 925 K. These recovery temperatures of the precipitates are consistent with the solubility limit of Cu in Fe [27].

In the second study [25], different binary alloys (Fe-C, Fe-Si, Fe-P, Fe-Mn, Fe-Ni and Fe-Cu) were irradiated by electrons ($2 \times 10^{18} \text{ cm}^{-2}$ with energy of 3 MeV) in order to produce only Frenkel defects (interstitial atoms and vacancies). It was verified that Ni (Fe 0.65 at % Ni) and P (Fe 0.07 at % P) alloy contributes to the formation of clusters of vacancies. Moreover irradiation induced vacancies form vacancy-solute-aggregation in C (Fe 0.9 at % C) and Cu (Fe 0.27 wt% Cu) alloy.

In the copper alloy especially, vacancies are found to be surrounded by a majority of copper atoms (80%), suggesting that large vacancy-multi-Cu-atom complexes occur. In case of neutron irradiation vacancies rich regions are produced in the collision-cascade of the primary knock-on atom, which favorites the aggregation [24]. In this study [25] the Cu atoms are detected to form aggregates at room temperature accompanying mono-vacancies without the collision-cascade.

In Si (Fe 0.9 at % Si), Mn (Fe 1.5 at % Mn) and P (Fe 0.07 at % P) there are not indication of association of vacancies with solute atoms. The annealing treatment effects have been investigated as well and it was verified that in all the alloys the vacancies recover at 625 K. As pointed out in [24] the recovery of the vacancies does not mean the recovery of the induced clusters.

2.2.7 SANS studies on RPV

Small angle neutron scattering is applied to binary (Fe,Cu), ternary (Fe, Cu, Mn) alloy and RPV steels. SANS is a valid experimental technique because can provide detailed information about the mean size and the composition of the cluster. Applied to binary and ternary alloy neutron irradiated ($1 \times 10^{23} \text{ m}^{-2}$ at 550 K), clusters are verified to be larger and less numerous in case of binary alloy [7]. If Mn is diluted in the samples, then the cluster density increases and smaller clusters rich of Mn are expected. Moreover with the assumption that the Cu-Mn precipitates are spherical and non-magnetic features in a saturated ferromagnetic iron matrix, and considering that the ratio between the nuclear and magnetic scattering is linear function of the precipitates mean composition, it is possible to estimate the cluster average composition. In the binary alloy two possibilities occur: the first with 98 % of Cu and 2 % vacancies, the second with 72 % of Cu, 20 % of Fe and 8 % of vacancies. In the case of ternary alloy the percentage of Cu is always very high, in the first case the mean cluster composition is: 94 % of Cu, 6 % of Mn and no Fe and vacancies. In the second case: 70 % of Cu, 10 % of Mn and 20 % of Fe with no vacancies. Comparison with the results obtained by APT affirms that significantly higher Cu amount is found in clusters by SANS [7].

In a second study [28], the role of Ni was investigated. RPV steels with a high amount of Ni were investigated in function of the neutron fluence. As found in [7] for the manganese, the radius of the mean cluster increases with the neutron fluence and it decreases with the amount of Ni. Moreover, the number of clusters density and the cluster volume fraction increase a lot for large content of Ni [28].

3. Theory

This chapter concerns the models applied to the material analysis and to the XAFS analysis in order to investigate the size, the elements and the distribution of solute atoms in the clusters. Two different models are applied, the first for the RPV materials and the second for inactive FeCu alloy. The second part of this chapter refers to the XAFS theory with a special regard to the main features and limit of this technique applied to clusters. The third part provides some details about the limitations of XAFS spectroscopy if applied to clusters investigation.

3.1 Materials

The ideal alloy would be one phase solid solution without defects. However the real alloy may consist of metallic matrix including precipitates of a different phase. The detection of clusters and eventual matrix damage is the main topic of this thesis.

3.1.1 Matrix damage

The study of the matrix damage is particularly difficult because of the partial information available by experimental technique used. Many nano-defects can be found in irradiated steel and, as seen in Chapter 2, most of them are caused by the atomic cascade due to the (fast) neutron irradiation. Basically the atom cascade changes the atoms distribution in the matrix and favorites the formation of vacancies. Vacancies are produced: some of them are recovered by surrounding atoms; some others can form groups of vacancies, particularly suited to be filled with solute atoms as shown in Section 2.2.5.

Considering some literature studies [24, 25] presented in Chapter 2 (Section 2.2.6), it is reasonable to consider that the vacancies detected in the steels (Sections 5.3 and 5.4) are not uniformly distributed in the samples, but they are highly concentrated near the absorbers, above all Cu absorbers. Nagai *et al.* [24, 25] proved that Cu atoms can form 'bounds' with vacancies stronger than the other solute elements. This phenomenon is particularly important because it favorites the formation of large Cu clusters.

The existence of vacancies makes the role of interstitial atoms rather important. Single interstitial atoms and vacancies affect strongly the interatomic distances between the surrounding atoms causing a shortening or a broadening respectively.

The experimental technique most intensively used in this thesis is XAFS and is presented in detail in Section 3.2. For the investigation of the matrix damage, it is rather important to point out that XAFS can detect defects on a nano-scale but it fails on large scale defects as grain boundaries distortion. Vacancies, interstitial atoms and nano-defects (i.e. bounds between vacancies and Cu atoms) can be revealed by EXAFS as:

1. a decrease of the number of first and second neighbors around the absorber;
2. the variation of the atomic distances;
3. an increase of the Debye-Waller factor.

Interstitial atoms are expected to contribute to the dumping of the amplitude of the EXAFS signal, roughly as vacancies do. The best way to investigate their influence concerns point 1 because significant distortion between i.e. Cu-Cu and Cu-Fe bounds are not expected to be significant since the matrix phase does not change.

The method used to investigate the matrix damage concerns point 1. The amplitude of the EXAFS signal produced by an active sample can be related to the amplitude of a reference by

$$\text{Amplitude (irradiated sample)} = \text{Amplitude (unirradiated reference sample)} * \alpha \quad (3.1)$$

where the Amplitude is the modulus of eq. 3.19 introduced in section 3.2.3.

Since the unirradiated reference samples have the largest amplitude the scaling factor α is always smaller than '1'. This model can be used in for different environments according whether composed of an element (i.e. pure Fe) or two elements (i.e. Fe and Cu). In the first choice there is a reduction of free parameters and the use of the same environment for all samples underline the differences among them. The use a more complex environment (with two elements) makes the data analysis more difficult and is preferred identifying differences of concentration in the environment of the absorbers. This model is used to investigate the presence of clusters.

3.1.2 Homogeneous cluster model

A simple model of steel (e.g. RPV) is introduced. The system selected is bcc. Steels composed of a high number of different solute elements, named $M_1 \dots M_N$, in the matrix composed of M_0 . Some simplifications need to be introduced.

1. Solute atoms are dissolved in the sample.
2. Not all elements are distinguishable by the analytical technique. So for example in order to distinguish M_1 and M_2 $\Delta Z \geq 2$ is required.
3. All elements are not suited to be investigated by the technique if they are much lighter than the matrix (for instance if $Z_{M3} \ll Z_{M0}$).

Considering a matrix composed of three elements M_0 , M_1 , and M_2 where M_0 composes the matrix and M_1 and M_2 are the solute element.

The environment of an element is investigated by mean of a selective technique. This means that it is possible to select an element, called 'absorber', i.e. M_1 . A selective technique is always able to distinguish different elements, because the selectivity is guaranteed by physical characteristic (i.e. absorption energy) typical of an element. According to point 2, two similar elements M_1 and M_2 are not distinguishable if $\Delta Z < 2$. This means actually that from the point of view of the absorbers atoms these elements behave similarly because of their almost identical size. Assuming that M_0 is different than M_1 ($\Delta Z \geq 2$) then M_1 can be surrounded by M_0 atoms, M_1 or M_2 . But M_1 and M_2 are undistinguishable so M_2 atoms count as they are M_1 .

M_0 and M_1 are weighted with two parameters: x and y where x represents the fraction of M_0 in the first shell and y in the second. Therefore $(1-x)$ and $(1-y)$ represent the fraction of M_1 in the first and second shell respectively. Therefore it follows:

$$N_{M_0} = N_{1,2} \left[\frac{8}{14} x + \frac{6}{14} y \right], \quad (3.2)$$

$$N_{M_1} = N_{1,2} \left[\frac{8}{14} (1-x) + \frac{6}{14} (1-y) \right], \quad (3.3)$$

where $N_{1,2}$ is the experimental sum of the next neighbours number in the two first shells in the bcc crystallographic lattice. The only boundary conditions are:

$$0 \leq N_{M_0} \leq 14 \quad \text{and} \quad 0 \leq N_{M_1} \leq 14, \quad (3.4)$$

x and y expected to be $0 \leq x \leq 1$ and $0 \leq y \leq 1$ but the first and the second shells convolute in the first main peak in the radial distribution the ΔR is too small to discriminate the 2 shells and they can not be considered separately. The high correlation of the two shells implies a high correlation of all the variables that refer to these shells.

Therefore the notation $N_{M_1M_2}$ will be used to identify the numbers of atoms M_1 plus M_2 in the 1st and 2nd shells.

3.1.3 Particles, clusters and precipitates

In this thesis the terminology used to identify aggregates of atoms is as follow:

1. Particle refers to all nano aggregates (clusters or precipitates). They have the same structure as the matrix.
2. Cluster refers to aggregate with the same structure as the matrix regardless their size but these are generally small.
3. Precipitate refers to aggregate with a structure different from that of the matrix regardless their size but they are supposed to be large.

Ideal dilution (e.g. the solute percentage is below 2 %) occurs if each solute atom is surrounded by atoms of the matrix (M_0). The first stage of cluster formations concerns the formation of particles, initially composed of a few atoms: dimers in case of a two atoms, trimers in case of three. These aggregates are in the same phase as the matrix. The clusters do not grow uniformly and many phenomena are involved. A crucial point concerns the definition of cluster. Different methods exist according to which technique is used, for example, Hyde introduced the ‘maximum separation method’ to evaluate the clusters size [29]. This method is based on the basic concept that the solute atoms are closer if they belong to clusters than if they belong to the matrix. Therefore two solute atoms are in a cluster if these atoms are within a maximum distance called D_{max} . This method detects all the aggregates with 2 or more solute atoms. A cutoff limit s_{min} is introduced to avoid considering clusters aggregates of a few atoms that randomly may occur and small particles. Both D_{max} and s_{min} may be evaluated by APT measurements and by simulations of a random solid solution respectively [30]. D_{max} was set to 0.5 nm [7]. A different method was applied by Radiguet *et al.* [20]: a sphere with radius 0.8 nm is built around each atom. In such volume, with a detection efficiency of 0.5, 100 atoms are expected. A cluster is detected if the Cu amount in the volume is larger than a threshold value (4 at %). These methods are very useful for APT, but they do not match perfectly with XAFS. It needs to be reminded that XAFS can investigate the composition mostly within 0.3 nm from the absorber. The conditions chosen by Miller *et al.* [7] and by Radiguet *et al.* [20] seem to concern clusters too diluted to be identified by XAFS. Moreover XAFS spectroscopy provides average information on all the absorbers in the samples, regardless whether they belong to clusters or to the matrix. By EXAFS clusters can be identified if the amount of solute atoms in the first and second shell is significant. Several factors may help cluster formation and coalescence; the most important is the insolubility of the solute in the matrix. High insolubility may bring the segregation of the solute atoms from the matrix. Other factors are mainly due to external treatments as annealing and irradiation. High insolubility and temperature treatment are responsible of

the formation of purer and purer clusters. Assuming that a solute element, i.e. M_1 , almost insoluble in M_0 , crystallizes in bulk structure different from that of M_0 , then it is expectable that a cluster of a certain size would try to crystallize in its bulk structure. The phase change, which corresponds to the cluster-precipitate change, depends on different parameters. High temperature treatment, high density of defects (i.e. caused by irradiation), large percentage of solute atoms and insolubility of solute may support the phase change.

The phase change is not an edge-phenomenon that always occurs if and only if the clusters reach a certain size, but it can occur for many different sizes. First of all the transformation between bcc-fcc is not abrupt, but it is composed of two intermediate steps, so that bcc-9R-3R-fcc. 9R is a 'structure close related to fcc and may be regarded as a close-packed structure a stacking fault every third plane' [31, 32]. In literature some 'structural transformations' are detected at about 6 nm [32] and an intermediate phase, called 9R, is claimed to appear if cluster size is between 4 and 18 nm [33]. The 9R structure approaches fcc structure through the 3R intermediate phase which is supposed to occur in the range of 18-30 nm. In this thesis just a few samples showed a mix of different phases and the small difference between 9R-3R-fcc were not reputed detectable. One of the main constrain of cluster-precipitate change is the purity of solute atoms inside the cluster itself. It has been shown in literature (see Chapter 2) that weld steel can reach 55 % of solute atoms in the inner part of the cluster (within 0.8 nm from the center, cluster radius is ~ 3 nm) and this percentage decreases constantly with the increase of the radial distance. Basically such cluster has a radius of 3 nm and it has the same phase as the matrix. It has been observed that smaller clusters but with a higher density of solute atoms changes phase (see Chapter 5, 6 and [34]).

The investigation of a cluster distribution has some issues connected with the polydispersity and with the incertitude on the number of atoms in the first shell N_l . N_l incertitude is generally ~ 10 %. In Figure 3.1 the relation between N_l is connected to the number of atoms in a cluster N_{at} for a fcc phase and for the bcc phase. In Figure 3.1, three different limits may be found:

1. $N_{at} < 150-200$ atoms;
2. $200 < N_{at} < \sim 1500$ atoms;
3. $N_{at} > 1500-2000$ atoms.

In (1.) range, N_l increases strongly with the increase of N_{at} . Assigning a nominal incertitude of 10% to N_l , the corresponding value of N_{at} is estimated with high precision. This region is suit to be investigated in detail as shown in [35].

In (2.) a nominal incertitude of 10% applied to N_l would include clusters with N_{at} dramatically different. For instance, a cluster of ~ 800 atoms would show in the first shell the same coordination number (± 10 %) as a cluster with ~ 200 atoms and one with more than 1600. Although the error applied to N_l for the first shell, under special conditions, such as high quality of the data and easy environment around the absorber, can be reasonably considered slightly lower than 10 % (from 5 to 10%), N_{at} would always be evaluated within a wide range of cluster sizes. In (2.), basically, an estimation of the mean cluster size may be performed but the incertitude, determined through incertitude of N_l , is expected to be very large.

In (3.), if nominal incertitude of 10 % is given to N_l , clusters with $\sim 1500 - 2000$ atoms ($\sim 3-3.6$ nm diameter) would result to have the same N_l as the bulk structure, as can be

deduced from Fig 3.1. Basically for such large clusters EXAFS results need to be considered as qualitative results.

Figure 3.1 is based on the work of M.A. Shandiz [36], the two functions (N_{1fcc} and N_{1bcc}) are calculated using some formulas deduced for different fcc and bcc cluster structure (cubic and octahedron). Since the clusters are expected to be sphere-like, Fig 3.1 concern clusters obtained from a 50 % of cubic and a 50 % of octahedron clusters.

In literature there are other studies about the relation between N_1 and N_{at} , in particular ref [37]. Comparing the curves from [36] and [37] it is possible to find some slight differences because different mathematical formulas have been applied to solve the issue. These differences are more pronounced for large clusters, but they are not in the region where EXAFS is more precise and accurate (1.).

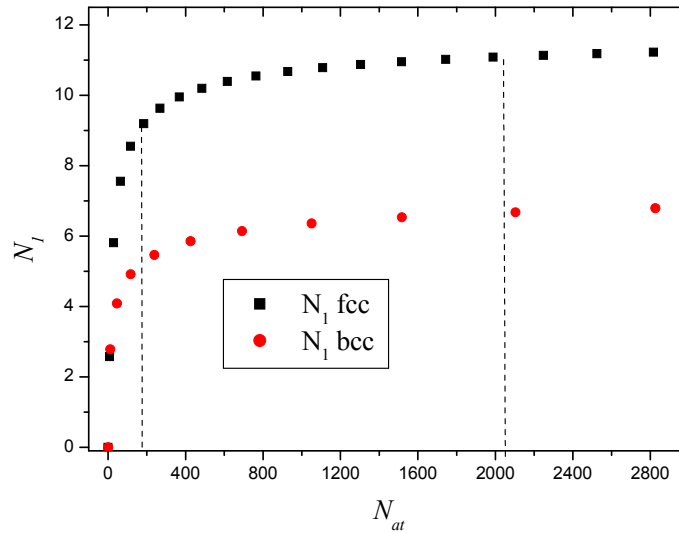


Figure 3.1: Number of atoms in the first shell as a function of the number of atoms in cluster. The curve is drawn considering N_{at} as composed of 50 % of cubic 50 % of octahedral fcc (black) and bcc (red) clusters. The dot lines shows the limits described in (1), (2) and (3).

3.1.4 Heterogeneous cluster model

The analysis of a heterogeneous system is here introduced for a simplified system composed of two elements M_0 , which is main component of the matrix ($\sim 99\%$) and the solute element M_1 ($\sim 1\%$). The system is composed of clusters, with the same phase as the matrix (i.e. bcc), and precipitates, with a different phase, embedded in the matrix (i.e. fcc). The clusters as well as the precipitates might be composed of a mix of M_0 and M_1 otherwise of pure M_1 . According to Schilling *et al.* [38], the existence of only two phases (bcc and fcc) are considered in this paper. Consequently no vacancies and interstitial defects are included in the data analysis. Although quite rigid, this assumption has proven to give accurate results [39-42]. Since in a bcc phase the first and the second shells are very close, their contribution convolutes in the first peak of the Fourier transform (FT) of the EXAFS spectrum. This means that the contributions of these two shells cannot be

distinguished and that they have to be considered as one shell containing 14 atoms (8 from the first shell, 6 from the second). In the fcc M₁-like their distance is larger: the FT of the EXAFS signal of these shells does not convolute, so only the first shell in the fcc phase is taken in to account in the model. It is defined:

1. n^{bcc} is the fraction of total atoms in the bcc phase around the absorber, $n^{fcc} \equiv (1 - n^{bcc})$ is the fraction of total atoms in the fcc phase around the absorber;
2. x is the fraction of M₀ atoms in bcc phase, $(1-x)$ is the fraction of M₁ atoms in bcc phase;
3. y is the fraction of M₀ atoms in fcc phase, $(1-y)$ is the fraction of M₁ atoms in fcc phase.

Finally $n_{M_0}^{bcc}$ is the fraction of M₀ atoms in the first shell around the absorber diluted in a bcc phase, i.e.:

$$n_{M_0}^{bcc} = n^{bcc} \cdot x ; \quad (3.5)$$

$$n_{M_1}^{bcc} = n^{bcc} \cdot (1 - x) ; \quad (3.6)$$

$$n_{M_0}^{fcc} = (1 - n^{bcc}) \cdot y = n^{fcc} \cdot y ; \quad (3.7)$$

$$n_{M_1}^{fcc} = (1 - n^{bcc}) \cdot (1 - y) = n^{fcc} \cdot (1 - y). \quad (3.8)$$

3.1.5 Cluster size distribution

Important particle parameters that will be used throughout this study are the individual particle mass m_i , diameter d_i and volume V_i , where the subscript i stands for the particle size class number. The density of the cluster is ρ_{Cl} [g cm⁻³].

The model needs to keep track of the concentration of clusters n_i for each size i in the matrix. Due to the assumptions of spherical clusters of density ρ_{Cl} , those quantities are easily inter-convertible by the Equations: $V_i = \pi d_i^3/6$ and $m_i = \rho_{Cl}V_i$. The variability of the density (ρ_{Cl}) with the size may be considered to reflect the change of the cluster structure going from the small crystalline cluster particles to the precipitate features.

In order to keep the problem tractable, maintaining at the same time a sufficient range of particle sizes, the scheme described by Houndslow *et al.* [43], which use geometric discrete distribution, is employed. The smallest clusters taken into account have a diameter d_0 (e.g. 0.3 nm). The corresponding volume of these clusters is $V_0 = \frac{\pi d_0^3}{6}$. All clusters having a volume between V_0 and $2V_0 = V_1$ form the first class of clusters. The next size class includes all clusters of volume V_1 to $2V_1 = V_2$, and so on. If two clusters, each having the same volume V_i , form a cluster size class that has the volume V_i , than larger clusters, with volume $>2V_i$, which is equal to V_{i+1} , belong to the upper next size class. The particle volume is divided into c intervals, such that the upper interval boundary is equal to twice the lower boundary: $V_i = 2V_{i-1}$, and V_0 is the minimum particle volume considered. Particles of size class i are therefore those with a volume

between V_{i-1} and V_i . The volume of class i particles ($1 \leq i \leq c$) is therefore given by:
 $V_i = 2^i V_0$.

The particle diameter, the most important parameter for particle characterization, can immediately be obtained for each size class: $d_i = 2^{i/3} d_0$. Particles smaller than size class 1 or larger than size class c do not exist and cannot be formed in this model. An interesting advantage of this scheme, other than being computationally convenient, becomes apparent if the particle size distribution is reported using a logarithmic size scale (see Fig 3.2):

$$\log(d_i) = \frac{i}{3} \log(2) + \log(d_0) \quad (3.9)$$

The relationship number of atom N_{at} vs size of cluster d may be obtained as a continuous function by considering the density of the cluster material ρ_{Cl} ignoring the crystallographic arrangement. In these conditions

$$N_{at} = \frac{A \rho_{Cl}}{\mathcal{M}_{M_i}} d^3 \quad (3.10)$$

where \mathcal{M}_{M_i} is the atomic weight of M_i (amu) and A is the Avogadro constant.

The relationship may also be obtained in a sequential way considering the crystallography of the cluster or that of the precipitate.

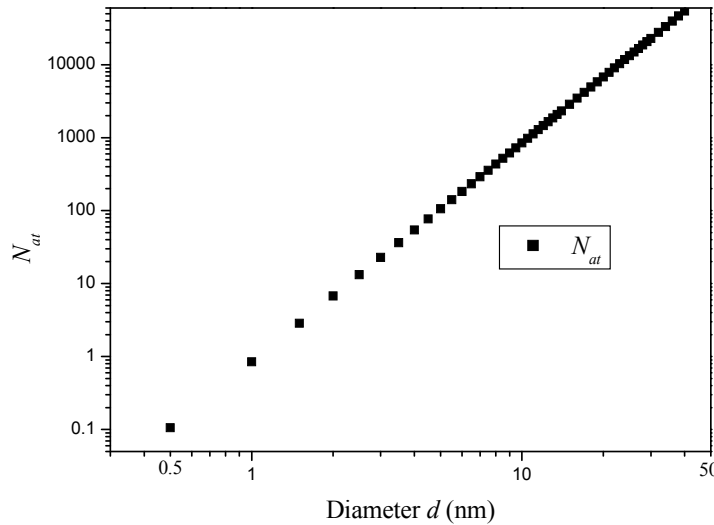


Figure 3.2: Number of atoms in a cluster vs of the diameter. The curve is obtained by equation 3.10.

Several phenomena are connected to the cluster distribution and formation, i.e. the phase coarsening. The theory of precipitate distribution is complex and it is not the main topic of the thesis, so only the main references will be provided and a brief description of the model applied, based on the XRD pattern, is shown in Chapter 6 (Section 6.1 and Fig 6.1).

The growth of a cluster is driven by a decrease of the total interfacial free energy of two-phase system. Larger precipitates may grow during the phase coarsening by absorbing some solute atoms from the matrix and they may also become purer removing atoms of different elements from the core of the cluster. The first model about growth of clusters was elaborated by Lifshitz, Slyozov and Wagner (LSW) [44, 45]. This model is based on the general idea that the total volume of the precipitates increases linearly with the time at a given temperature. In this model, the precipitates are considered so far away that there is not coarsening between precipitates. However in most of the experiments this does not happen and the interaction between precipitates cannot be excluded a priori. The LSW model considers that all precipitates, with the same size, have the same rate of growth. Basically the increase of their size is independent from the external structures, but it is verified that by Ardell's theory that the coarsening rate increases with the precipitates volume fraction [46]. Moreover if a cluster is close, within a certain radius, to other smaller clusters than its coarsening rate would be much higher than for a more isolated cluster. This and other stochastic events can influence strongly the overall theory and need to be taken in account [47]. In this work the precipitates distribution is investigated by XRD.

The applied model is thought for powder diffraction where the usual investigation by the Scherrer formula is not possible for the small size of the precipitates [48].

In case of powder diffraction there are experimental and theoretical proofs that the cluster sizes have a log-normal distribution [48, 49]. For the derivation of the size distribution we refer to [48] and this can be written as:

$$n\left(\frac{d}{2}\right) = \frac{1}{\frac{d}{2}\sqrt{2\pi\log(c)}} \exp\left[-\frac{\log^2(\xi\sqrt{c})}{2\log(c)}\right] \quad (3.11)$$

Where $\xi = d/d_{av}$ is the ratio between the diameter of a cluster d and the average precipitates diameter d_{av} , $c = 1 + 4\bar{\sigma}_R^2/d_{av}^2$ with $\bar{\sigma}_R^2$ is the standard deviation [48].

The size distribution introduced in formula 3.11 has the dimension of the inverse of a length in order to be normalized to unit if integrated all over the clusters diameter (from 0 to 100 nm) and it is represented by a continuous curve. By modeling, the distribution is divided by many columns (200), with step $\Delta d = 0.5$ nm. Finally the distribution is normalized by Δd and by the total volume of the sample, so that its dimension is $[\text{nm}^{-1}\text{cm}^{-3}]$. This normalization procedure is applied in Chapter 6.

3.2 X-ray absorption fine structure (XAFS)

X ray absorption spectroscopy (XAS) is intensively used in this work and this technique is presented in detail.

3.2.1. X-ray absorption and matter

There are five fundamental interactions of photons with atoms. Photoelectric absorption and Thomson scattering (elastic scattering) are the most important for small energies ($E < 100$ keV), Compton scattering (inelastic scattering) is the most relevant for energies around 1 MeV. At higher energies ($E > 10$ MeV) the formation of electron-positron pairs

becomes the first phenomenon while the probability of photoelectric absorption and the Thomson scattering decrease quickly to zero. Finally the photonuclear absorption is the last and less important phenomenon, it occurs around (10-50 MeV) and its cross section is much smaller than electron-positron pairs. The energies involved in all these phenomena depend strongly on the atomic number Z . Soft and hard x-rays are conventionally defined as the electromagnetic radiation with energies between 100 eV and 100 keV. In this range the photoelectric absorption is definitely the most relevant phenomenon.

There are energies for which the probability of an photoelectric absorption increase dramatically. These energies correspond to the binding energies of each orbital. As it was explained successfully by Einstein, the probability of absorption of x-rays is independent by the intensity of the radiation but it depends on its energy.

For a monoatomic sample the absorption coefficient is proportional to the cross section $\Omega(E)$ according to:

$$\mu(E) = A\rho\Omega(E)/\mathcal{M}_{M_i} \quad (3.12)$$

where $\mu(E)$ is the absorption coefficient, A is the Avogadro number, ρ is the mass density [g cm^{-3}] and \mathcal{M}_{M_i} is the atomic weight of the M_i elements. For a chemical compound $M_1 \dots M_i \dots$ with $z_1 \dots z_i \dots$ as respective proportional coefficients, the total absorption mass coefficient can be expressed as:

$$(\mu(E)/\rho)_{tot} = z_1(\mu(E)/\rho)_{M_1} \cdot A_{M_1}/\mathcal{M} + \dots + z_i(\mu(E)/\rho)_{M_i} \cdot A_{M_i}/\mathcal{M} + \dots \quad (3.13)$$

where \mathcal{M} is the molecular weight of the compound. With the increasing of the energy above the absorption edge, $\Omega(E)$ and $\mu(E)/\rho$ decrease and their trend can be empirically described by the Victoreen relation [50]:

$$\mu(E)/\rho = C\lambda^3 - D\lambda^4 \quad (3.14)$$

where the parameters C and D are functions of the atomic number Z and λ is, only in this formula, the wave length of the photons.

The absorption coefficient is measured generally by transmission or by fluorescence yield. In the case of monoatomic samples, such as metallic foil, the easiest way is by transmission. The intensity of the beam which passes through the sample decreases exponentially with the thickness of the sample l according to the law:

$$I = I_0 \exp[-\mu(E) \cdot l] \quad (3.15)$$

where I_0 is the intensity of the incident beam, I the beam intensity after the sample absorption and $\mu(E)$ is the absorption coefficient which depends on the energy of the incidents photons and on the sample composition.

I and I_0 can be measured, for example, by means of two ionization chambers placed before and after the samples. Generally the absorption coefficient $\mu(E)$ decreases with energy, interrupted only by some discontinuities that represent the absorption edges of the sample elements.

The edge at a higher energy, called K edge, is due to the absorption of the electrons in the orbital 1s. The L edge is at lower energies and concerns the electrons in the orbitals 2s and 2p. The L edge is split in three peaks L_1 , L_2 and L_3 for the absorption of electrons in 2s, $2p_{1/2}$ and $2p_{3/2}$ respectively. Its binding energy is higher than that of other electron and this is the reason for why more energy is needed. K edges usually are preferred because the resolution is higher due to the wideness of the k range compared to the L_3 spectra. K edge and L edges are also sensitive to magnetic fields [51, 52]. In this thesis only the K edge is analyzed.

Photons with energy higher than the binding energy are absorbed by the electrons in the corresponding orbital. The photoelectrons move in the conduction band and are scattered by the surrounding atoms.

The absorption energy, E_0 , is conventionally defined as the first peak of the absorption edge first derivative, and its value might slightly change compared to the bulk material due to valence change of the absorbing atoms by typically up to 10eV. Such shifts can be checked by collecting data of a reference foil simultaneous with the sample

The absorption edge is divided in three parts (see Fig 3.3):

1. the pre-edge region, limited to a few eV before the absorption energy E_0 (8979 eV for Cu).
2. the near edge region, refers to the first part of the absorption edge up to 50 eV above. This region is called XANES region, which means x-ray absorption near edge structure. This part of the spectrum is dominated by multiple scattering processes of photoelectrons emitted with low kinetic energy. XANES contains information on the electronic structure and geometry of the environment around the absorber atoms.
3. the last part is called EXAFS which means extended x-rays absorption fine structure, and it begins ~ 50 eV above the edge to about 1000 eV. The interpretation of EXAFS is generally simpler and much more consolidated than that of XANES, because it is mostly based on singles atomic scatterings whose understanding is easier.

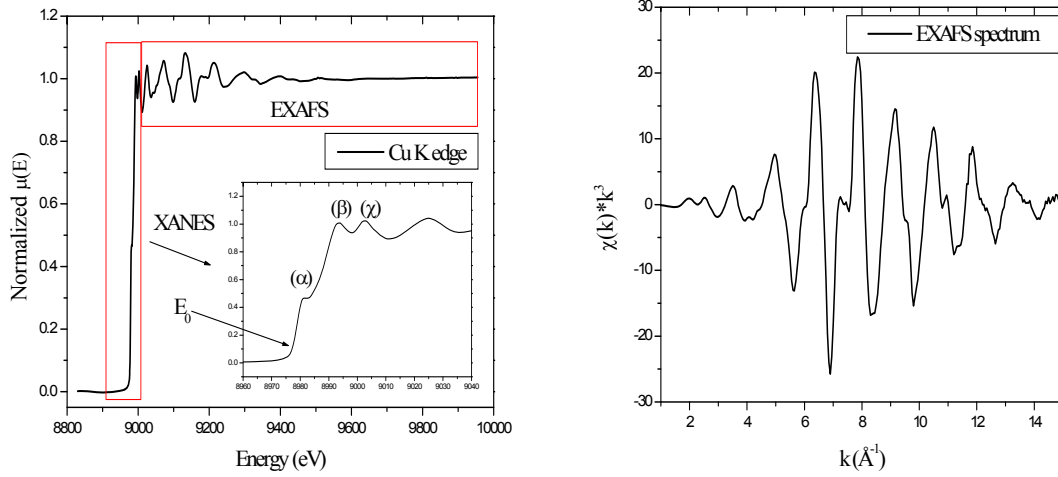


Figure 3.3: Normalized absorption edge of copper. In the inset the XANES part is shown (Left). The EXAFS oscillations extracted from the absorption spectra multiplied for a factor k^3 (right).

In this thesis the first part of the absorption spectrum, up to 50 eV above the E_0 , is called XANES. We refer to EXAFS whether only the second part, from 30 eV up to 1000 eV above the edge, is considered. We shall refer to XAFS when both XANES and EXAFS are considered.

As it was shown at the typical energies used, the photoelectric absorption is the main phenomenon. The theory of EXAFS is reviewed in several articles [53, 54]. RPV steel includes several elements $M_1, M_2 \dots M_N$ dissolved in the matrix of M_0 . A heat treatment and neutron irradiation can affect the atomic environment of $M_1, M_2 \dots M_N$ in the matrix and these changes can be investigated by an element specific technique as XAFS.

3.2.2 Absorption coefficient and threshold energy E_0

The absorption spectrum of an element is defined by the plot of $\mu(E)$ where E is the energy, μ the absorption coefficient. The threshold energy E_0 is determined by the first main peak of the absorption spectra first derivative, according to the criteria adopted by Ravel and Newville [55-57]. The threshold energy of a pure metal (M_i) is called $E_0^{M_i}$, for a RPV alloy E_0 . $E_0^{M_i}$ and E_0 depend on the chemical environment: a difference might mean the formation of a different structural phases with a consequent significant change in the atomic distances.

The energy shift ΔE_0 is defined as:

$$\Delta E_0 = E_0 - E_0^{M_i}. \quad (3.16)$$

The normalized part $\chi(E)$ of the x-ray absorption coefficient is written as:

$$\chi(E) = \frac{\mu(E) - \mu_0(E)}{\mu_0(E)}, \quad (3.17)$$

where the oscillatory part of the absorption coefficient $\mu(E) - \mu_0(E)$ is normalized to the structureless background μ_0 [53].

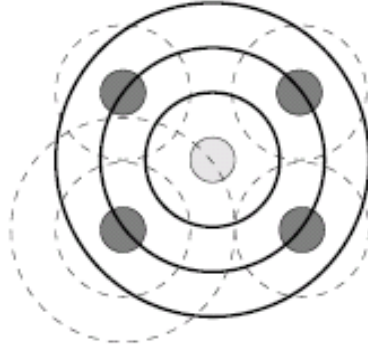


Figure 3.4: Qualitative representation of the scattering of a photoelectron. The atom hit by a photon with energy $h\nu$ represents the absorbing atom. The photoelectron propagates away from the absorbing atoms with a wavelength given by the De Broglie relation. The solid lines represent the crest of this wave. The photoelectron may scatter from the neighboring atom(s). The crests of the scattered wave are represented by the dashed lines. A maximum (minimum) in the absorption probability for the x ray occurs when the wavelength of the photoelectron, determined by the x ray energy, and the path of the photoelectron which is the distance to and from the neighboring atoms, corresponds to constructive (destructive) interference between the photoelectron waves at the absorbing atom.

3.2.3 The EXAFS spectrum

After having isolated the EXAFS oscillations from the absorption spectrum, it is useful to express $\chi(E)$ as a function of the wave number k defined as:

$$k = \sqrt{2m(E - E_0)/\hbar^2} \quad (3.18)$$

where m is the electron mass.

The EXAFS equation, considering i individual scatterings, is given by [54]:

$$\chi(k) = \sum_i \frac{N_i S_0^2 |F_i(k)|}{kr_i^2} e^{-\frac{2r_i}{\lambda(k)} - 2k^2 \sigma_i^2} \sin(2kr_i + 2\delta_i(k) + \Phi_i(k)), \quad (3.19)$$

where r_i is the modulus of the distance \vec{r}_i between the absorber and the shell i , N_i is the number of atoms in the shell i , S_0^2 is the amplitude reduction factor, the factor $F(k) = |F_i(k)|e^{i\Phi_i(k)}$ is the backscattering amplitude, $\delta_i(k)$ is the central atom partial phase shift of the final state, $\lambda(k)$ is the mean free path of the photoelectron; $e^{-2k^2 \sigma_i^2}$ is a reduction factor due to thermal and statistic disorder called Debye-Waller coefficient and σ_i^2 is the mean square relative displacement of the i shell.

3.2.4 Free mean path $\lambda(k)$

An important term in the XAFS equation, which affects strongly the range of the technique, is the finite lifetimes of the photoelectron and the core hole. Because the XAFS spectrum is caused by the interference between the original photoelectron and the scattered part of the photoelectron wave, the degradation of the wave due to inelastic scattering destroys its coherence and the XAFS spectrum as well. This can be interpreted as the limited lifetime of the photoelectron. The net effect of the finite core hole lifetime and the finite lifetime of the photoelectron can be combined in an exponential decay of the XAFS signal, written as:

$$e^{-2R/\lambda(k)}$$

where $\lambda(k)$ is the effective mean free path of the photoelectron. The limited range of the photoelectron permits a short range order description of EXAFS in crystalline materials [53, 54].

3.2.5 Thermal disorder, Debye Waller factor

The characteristic absorption time of an x ray is a few orders of magnitude smaller than the frequencies of the atomic vibrations. Moreover the data acquisition takes much longer periods. It means that the mean EXAFS contribution provided by a single atom, at a distance r_i , needs to take in account the entire possible configurations $r_i(t)$ that may affect the atomic distance r_i .

The simplest case consists of two assumptions:

- all the atomic distances of a certain shell are the same for all the atoms;
- the thermal fluctuations are small and they can be considered as harmonic (harmonic approximation).

Being r_0 the position of the absorber atom and r_i the position of an atom in the matrix in the i^{th} shell, if $\mathbf{u}(r_0)$ is the displacement vector of the absorber and $\mathbf{u}(r_i)$ the displacement for an atom at a distance r_i , then

$$r_i(t) = |r_i| + (\mathbf{u}(r_i) - \mathbf{u}(r_0)) \cdot \mathbf{r}_i + O(r^2); \quad (3.20)$$

thus introducing the harmonic approximation:

$$\exp[ik((\mathbf{u}(r_i) - \mathbf{u}(r_0)) \cdot \mathbf{r}_i)] = \exp[-2\sigma_i^2 k^2] \quad (3.21)$$

where $\exp[ik((\mathbf{u}(r_i) - \mathbf{u}(r_0)) \cdot \mathbf{r}_i)]$ is the average of the thermal disorder, called also Debye-Waller factor, and σ_i is the mean square relative displacement of the i shell [58-60].

3.2.6 $\tilde{\chi}(R)$: the Fourier transform of $\chi(k)$

In order to obtain the radial distribution function a Fourier transform (FT) of the experimental EXAFS function $\chi(k) \cdot k^n \cdot W(k)$ needs to be performed. Here k^n is a function used to amplify the EXAFS oscillations at higher k values and $W(k)$ is a ‘window’ function utilized to isolate a special range in the EXAFS spectrum. The analysis is performed fitting the FT of the experimental EXAFS function $\tilde{\chi}(R)$ with a theoretical model based on the ab-initio calculations for scattering phases and amplitudes using a special code e.g. FEFF [61]. It has to be clarified that $\tilde{\chi}(R)$ is a radial distribution function of R . R is a distance (Å) affected by a phase shift that rises from the FT of Eq. 3.19.

3.2.7 Quality factor

The number of information that can be obtained from fitting the FT of the experimental EXAFS depends on the Fourier Transform range (ΔR) and on the fitting space range in the k -space (Δk) [62]. Both these quantities are determined by the window function used in the fit: $W(k)$ and $W(R)$ are used to isolate the contribution of the first and second neighbours in the R space. The total number of independent data points n_I that can be fitted simultaneously is given by $n_I = (2/\pi)\Delta k \cdot \Delta R + 2$ [63] and this is the maximum

numbers of parameters that can be determined by a fit to the spectrum. The reduced χ^2 function is calculated [64]:

$$\chi^2 = \frac{n_I}{2N\sigma_N^2(n_I - P)} \sum_{i=1}^N |\chi^c(R_i) - \chi^e(R_i)|^2, \quad (3.22)$$

where the complex form of $\chi(R_i)$ is used and the sum is over the N point in the range of ΔR ; $\chi^c(R)$ and $\chi^e(R)$ are the calculated and experimental XAFS spectra transformed in R -space (both real and imaginary parts). The number of parameters used in the fit is P . The quality of the fit can be judged by χ^2 . If a correct model is used and if noise is dominated by random fluctuation, then $\chi^2 \approx 1$ is expected. There are some cases, such as for concentrated samples, in which random noise can be very small and a systematic error can dominate. So, it is introduced a new parameter, called \mathcal{R} quality factor, to evaluate the quality of the fit between data provided by the theoretical model and experimental data:

$$\mathcal{R} = \frac{\sum_i |\chi^c(R_i) - \chi^e(R_i)|^2}{\sum_i (\chi^e(R_i))^2} \quad (3.23)$$

\mathcal{R} is a pure number, it has to be as small as possible, in general $\mathcal{R} = 0.01$ means that theory and data differ only by 1% [62].

3.3 Limit of XAFS spectroscopy

In this section the limits of the XAFS spectroscopy applied to clusters are shown. Mainly there are mostly two issues that concern the study of clusters and absorption spectroscopy: the first refers to anharmonic corrections that have to be introduced to avoid underestimating the mean cluster size. The second refers to polydispersity and it is strictly connected to the impossibility to recognize, by data analysis, if an XAFS spectrum is provided by a poly-disperse clusters distribution or by mono-disperse clusters. It is important to point out that this problem is an intrinsic problem of XAFS, thus it is independent of the quality of the data.

3.3.1 Temperature consideration: anharmonic corrections

Generally the clusters smaller than 200 Å have a rather large fraction of atoms at the surface compared to those in the core. So a decrease of number of first neighbors, due to the absorber position at the surface of the cluster, can be easily determined by EXAFS. It should not be forgotten that most of the EXAFS studies are based on the Gaussian-like pair distribution. Unfortunately, molecular dynamics simulations have showed that atom move inside a small clusters of Cu anharmonically [65]. Consequently, a new and non-Gaussian pair distribution function is needed. Generally in the data analysis, the first part of the EXAFS spectra ($k < 3 \text{ \AA}^{-1}$) is not treated because is complicated by multiple scattering and a non perfect background removal. Nevertheless this part is important using a non-Gaussian pair distribution function. The anharmonic behavior is visible on the FT of the EXAFS signal [66] and generally brings a significant underestimation of the cluster sizes. This behavior increases and has to be taken in account with the decreasing of the cluster sizes and with the increasing of the temperature. For low temperature, such as 15 K, the non-Gaussian pair distribution function does not differ significantly to the commonly used Gaussian pair distribution function (see Fig. 3.5). In this case the

foreseen underestimation is lower than the $\sim 5\%$ and it is within the experimental error. So for the samples analyzed at low temperature these corrections will not be considered. For the samples analyzed at room temperature the number of atoms in the first and second shell is affected by a large uncertainty (larger than the nominal 10%), so that this correction will not bring a significant change and it will not be considered as well.

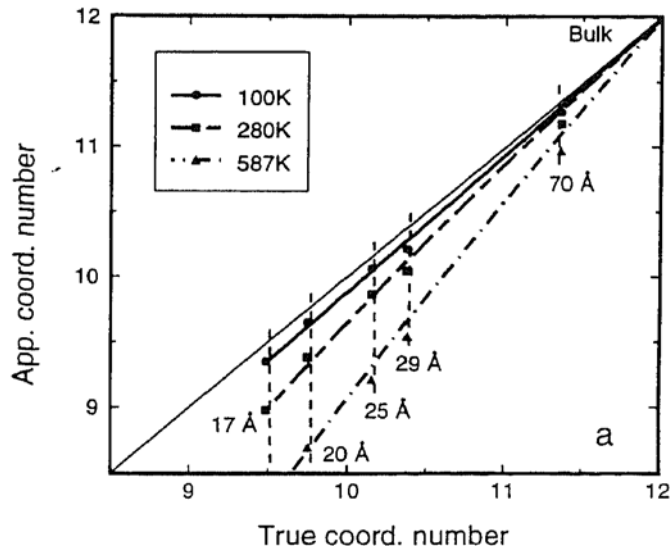


Figure 3.5: Relation between the apparent first shell coordination number determined from the standard EXAFS analysis and the true coordination number determined from molecular dynamic simulations for Cu clusters (Data from [66])

3.3.2 Polydispersity

It has to be pointed out that x ray absorption spectroscopy provides an absorption edge spectrum, which is the average of the contributions of a large number of absorbers. If absorbers form clusters embedded in a matrix, some of the atoms would occupy the core of the clusters while the others the surface, which corresponds to the interface between the cluster and the matrix. The importance of the contributions of the atoms laying in the interface depends on their relative number compared to the number of atoms in the core [37]. The number of atoms in the core increases faster than the number of those on the interface with the increase of the cluster radius. So for large clusters the atoms in the interface become less important [42, 67-69]. XAFS spectroscopy is a powerful technique to investigate clusters, but it is insensitive to polydispersity: the results given by mixing clusters, which have 13 and 1415 atoms, are similar to the coordination number associated with a cluster of 147 atoms [70].

An improvement in the determination of the mean size and shape of small particles by EXAFS was done by Jentys [37] who provided an empirical method about how to calculate the numbers of coordination in the first five shells in function of the total number of atoms involved in the cluster N_{at} (see Fig 3.1). A detailed analysis about polydispersity issue and its solution for cluster smaller than 135 atoms is shown in [35].

4. Experimental

In this thesis three series of samples are analyzed: first is composed of inactive samples (binary alloy, Fe Cu) and the second and the third of active reactor pressure vessel steel. The analyses were performed at different synchrotron facilities and in the laboratory of nuclear material at PSI.

4.1. Studied samples

4.1.1 Binary alloy samples

Four binary alloy (Fe,Cu) samples were elaborated by LETRAM/SRMA, CEA, Saclay (see Tab 4.1). A chemical analysis revealed a composition of: 1.34 ± 0.04 at % Cu. In the first step the samples were cold rolled to a thickness of ~ 25 μm and then cleaned in a $\text{H}_2\text{O}_2 + 5\%\text{HF}$ bath. In the second step, the samples were annealed for 24 h at 1110 K (samples A and D) or 1090 K (samples B and C) under H_2 . Finally the samples underwent thermal ageing under H_2 at a temperature of 775 K for 2.5, 8.0, 115 and 312 h (samples A, B, C and D respectively), see [18].

Table 4.1

Four inactive binary samples are investigated. The composition is Fe 1.34 ± 0.04 at % Cu. The last thermal aging is reported.

Elements	Sample A	Sample B	Sample C	Sample D
Time (h)	2.5	8.0	115.0	312.0
Temperature (K)	775	775	775	775

4.1.2 Japanese Reference Quality (JRQ) samples

The material investigated is an iron based ferritic steel (A533 grade B) designated as JRQ [71]. The chemical composition of the material is given in Table 4.3. The samples were prepared during the implementation of an International Atomic Energy Agency (IAEA) co-ordinated research project on behaviour of RPV steels under neutron irradiation [71].

Table 4.2

Elemental composition of the JRQ[71] steel material. The iron fraction is the balance.

Elements	C	Si	P	S	V	Cr	Mn	Ni	Cu	Mo
Weight %	0.18	0.24	0.017	0.004	0.002	0.12	1.42	0.84	0.14	0.51
Atom %	0.83	0.47	0.03	0.007	0.002	0.13	1.43	0.79	0.12	0.30

The JRQ steel was produced as described in Ref. [71] and only a short description is provided here. In the first step the material was rolled, and subsequently normalized at 1175 K, quenched from 1155 K, tempered at 940 K for 12 hours, and then stress relieved at 895 K for 40 hours. The normalization is a thermal treatment used to refine grains which have become coarse through work-hardening, to improve ductility and toughness of the steel. A reference unirradiated sample, here denominated REF_JRQ and four irradiated samples have been obtained. The irradiated samples were submitted to different neutron irradiation and annealing treatments. The irradiation was performed at the PSI

research reactor 10 MW SAPHIR and the re-irradiation at the University of Michigan Ford Nuclear Reactor (FNR) according to the parameter summarized in Table 3. The samples were irradiated with an average neutron flux of $\sim 4 \times 10^{10} \text{ cm}^2 \text{ s}^{-1}$. Thank to the position where the samples were placed, the flux on the surveillance samples was 100 times larger than the flux on the RPV. All irradiations were performed at a temperature of 560 K. The sample K116 (designation I as Irradiated) was submitted to a neutron fluence of $5 \times 10^{19} \text{ cm}^{-2}$ ($E \geq 1 \text{ MeV}$). The sample K612 (IA: Irradiated and Annealed) was submitted to a long annealing treatment (735 K for 168 h). The sample M646 (IAR: Irradiated, Annealed, Re-irradiated) was irradiated in the first step with a significant smaller neutron fluence of $0.85 \times 10^{19} \text{ cm}^{-2}$, then it was annealed for a short period (735 K for 18 h) and then it was re-irradiated with the same fluence. The sample M113 was submitted to the same treatment as IAR, and then it was annealed (735 K for 168 h) again; its denomination is IARA. The samples have been cut to a size of $3 \text{ mm} \times 3 \text{ mm}$ having a thickness of 1 mm.

Table 4.3

Neutron fluence and temperature treatment for the samples. Φ is the neutron fluence.

Treatments JRQ samples	1 st irradiation Φ (cm ⁻²)	1 st treatment T (K) t (h)	2 nd irradiation Φ (cm ⁻²)	2 nd treatment T (K) t (h)
REF_JRQ (LM3)	-	- -	-	- -
I (K116)	5×10^{19}	- -	-	- -
IA (K612)	5×10^{19}	735 168	-	- -
IAR (M646)	0.85×10^{19}	735 18	0.85×10^{19}	- -
IARA (M113)	0.85×10^{19}	735 18	0.85×10^{19}	735 168

4.1.3 Kernkraftwerk Gösgen (KKG) samples

The material investigated is an iron based ferritic steel designated here as KKG. The chemical composition of the material is given in Table 4.4. The samples were provided by the nuclear power plant of Gösgen (Däniken, Switzerland).

Table 4.4

Elemental composition of the KKG steel material. The iron fraction is the balance.

Elem	C	Al	Si	P	S	V	Cr	Mn	Ni	Cu	Mo
Wt%	0.18	0.02	0.14	0.006	0.008	0.009	0.40	0.81	0.96	0.09	0.32
At %	0.78	0.04	0.26	0.01	0.013	0.01	0.43	0.84	0.89	0.08	0.20

An unirradiated reference sample, here denominated REF_KKG, and three differently irradiated samples have been obtained. All these samples had been submitted to the same pre-treatments (e.g. $\sim 10 \text{ h}$ at $\sim 880 \text{ K}$). For irradiation, the surveillance samples were positioned close to the reactor core. The samples, inside capsules, were placed at 2 m from the axial core centre and roughly 25 cm below the mid core level. Because of the shorter distance to the core, the fluence is enhanced by a certain factor, reducing time for obtaining representative irradiation damage. Consequently, the fluence recorded on these surveillance samples was about 12 times larger than the fluence recorded on the actual reactor pressure vessel. The samples were exposed to the same temperature as that of the reactor water, i.e. $\sim 575 \text{ K}$, for this reason they are named HI which means hot irradiated.

The 3 surveillance samples were irradiated for 1, 3 and 4 years, thus to distinguish them, they are denominated HI1, HI3 and HI4, respectively (see Table 4.5).

Table 4.5

Neutron fluence and temperature of the samples. The actual reactor pressure vessel was submitted to an average neutron flux of $6.75 \times 10^{18} \text{ cm}^{-2} \text{ a}^{-1}$ ($E \geq 0.821 \text{ MeV}$); the surveillance samples were submitted to a neutron flux 12 times larger. The active samples are named HI (Hot Irradiated) because the irradiation was performed in a nuclear power plant. The numbers (1,3,4) refer to the years of irradiation.

KKG Samples	Irradiation, n fluence ϕ (cm^{-2})	Thermal conditions	
		T (K)	t (a)
REF_KKG	0	~300	10
HI1	4.75×10^{18}	575	1
HI3	1.09×10^{19}	575	3
HI4	2.60×10^{19}	575	4

4.2. Samples analysis

4.2.1. EXAFS at ANKA (FKZ)

The samples were analyzed at the XAS beamline at ANKA at the Forschungszentrum Karlsruhe (FZK). No specific requirements with respect to the beam were needed. This analysis was performed in a cryostat at 15 K. A 5 elements Ge solid state fluorescence detector was applied to record spectra data. The detector was perpendicular to the beam; the sample and the sample holder formed an angle of 45° with the beam and with the detector. During this beamtime the inactive binary alloys were investigated as well as the REF_JRQ and REF_KKG reference samples.

4.2.2. EXAFS at SLS (PSI)

The XAFS experiments were performed at the micro-XAS beamline of the Swiss Light Source (SLS) synchrotron facility. SLS is a third generation synchrotron, and the main information are summarized in Table 4.6 [72]. In this section a short description of the experiment set up is given.

Table 4.6

Main information of the storage ring of the Swiss Light Source (SLS). For more details see Ref. [72].

Storage ring parameter	Units	Value
Reference energy	GeV	2.4
Circumference	m	288
Current	mA	400
Emittance	nm	5

The electron current in the storage ring is around 400 mA and at 12 keV 3×10^{12} photons/s are expected on the sample while the optical elements used ensure an energy resolution of $\Delta E/E < 10^{-4}$ [73]. The beamline is constituted of different hutches. In the optical hutch there is a double crystal monochromator to select the required energy. Three different pairs of crystals are available: Si (111), Si (311) and Ge (111); in this thesis only the Si (111) was used. "A bendable toroidal horizontally deflecting mirror is used to collimate the beam in vertical dimension, to allow for dynamic demagnification in horizontal

dimension and to act as low-pass filter [73]”. The use of several slits allows an accurate selection of the beam size up to $\sim 1 \times 1 \mu\text{m}^2$.

In the experimental hutch, special precautions had to be taken to avoid radiation damage and a thick iron shield was used (see Fig 4.1): with the shielding, a dose rate of less than 20 mSv per week can be assured (with specimen dose rate in mSv/h range).

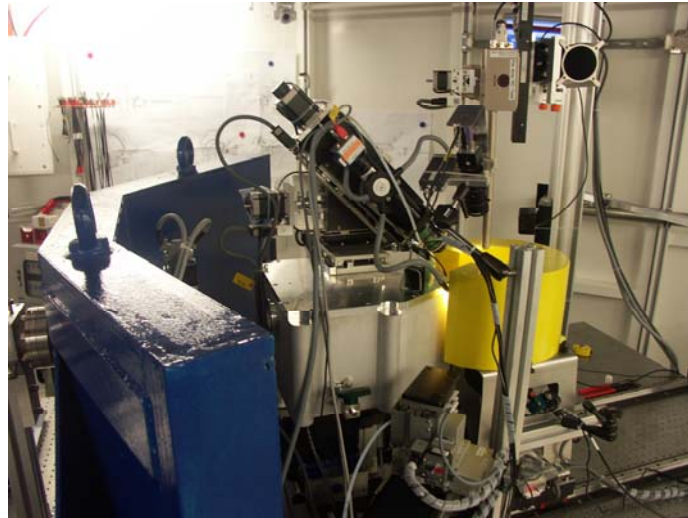


Figure 4.1: view of the set up for the radioactive sample XAFS experiments at the micro-XAS beamline.

The experiments were performed in fluorescence yield mode because the dilution of the solute elements did not allow transmission mode. The detection apparatus involved two instruments: the incident x-ray intensity was measured by means of an ultra-thin silicon based diode, a self made x-ray-eye, and a 32-elements Ge solid state fluorescence detector (see Fig 4.2).

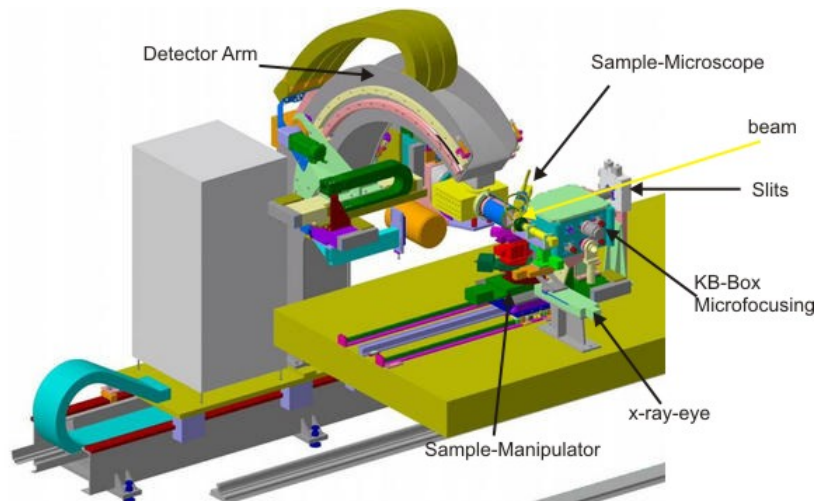


Figure 4.2: The geometry of the detectors in the experimental hutch.

A many-elements detector is mandatory in order to collect data of good quality in a reasonable time. Cu, Ni, Fe and Mn K-edges were investigated for the sample JRQ [71], while only Cu and Ni K-edges for the KKG samples.

The specimens were held at room temperature. The detector system and the sample manipulator allow the analysis of the sample with much different geometry. The experiments were all performed with the geometry shown in Fig 4.2: the sample was perpendicular to the beam on the electron orbit, so if the beam was parallel to the 'y' axis (that means parallel to the vector [010]), the detector was on the negative part of the 'x' axis (that means parallel to the vector [-100]). With this configuration the sample order was perpendicular to the vector [-111]. Several spectra (> 4) were collected for each K-edge and for each sample to obtain a better average result. The beamline allows also highly sophisticated micro x ray fluorescence mapping, micro-XRD and micro-XAFS, but these techniques were not used because the clusters embedded in the samples were expected to be smaller than 5 nm, so much smaller than the resolution of the techniques, and with the same crystallographic structure as the matrix. As it was unnecessary to use the micro-focused beam spots, experiments were conducted with a spot size of $250 \times 250 \mu\text{m}^2$.

4.2.3. TEM at LNM, PSI

TEM was applied only to sample D (see Tab 4.1) because this technique it is not sensitive to nano-clusters (~ 1 nm) which have the same structure as the matrix and with a similar atomic number. The sample was electro-polished at 250 K. The surface of the sample was slightly grinded to remove oxide before electro-polishing. A JEOL2010 operating at 200 kV (with a LaB₆ filament) equipped with an Oxford Instrument energy dispersive x-ray spectrometer (EDS) and INCA software was used.

4.2.4. XRD at SLS

Only the binary (Fe,Cu) samples are investigated by XRD because this technique can provide interesting information about clusters and clusters distribution only if they do not have the same structure as the matrix. The samples were mechanical polished and cut in small pieces in order to be filled in a capillary. XRD data acquisition was performed at the powder station of the X04SA-Materials Science beamline of the Swiss Light Source synchrotron at the Paul Scherrer Institut. The beam was monochromatic x-rays of 25 keV. Fluorescence suppression was achieved setting the discrimination threshold to 16 keV. For better linearity, Debye-Scherrer geometry has been used, with thin slices (0.1 mm wide, 0.05 mm thick, 3 mm long) of Cu-containing iron sheet enclosed in rotating glass capillaries. The Mythen II detector - acquiring simultaneously 29440 channels in 115° with high efficiency - allowed extreme high statistic patterns to be collected in minutes, see Fig 4.3. For more details see Ref. [74].

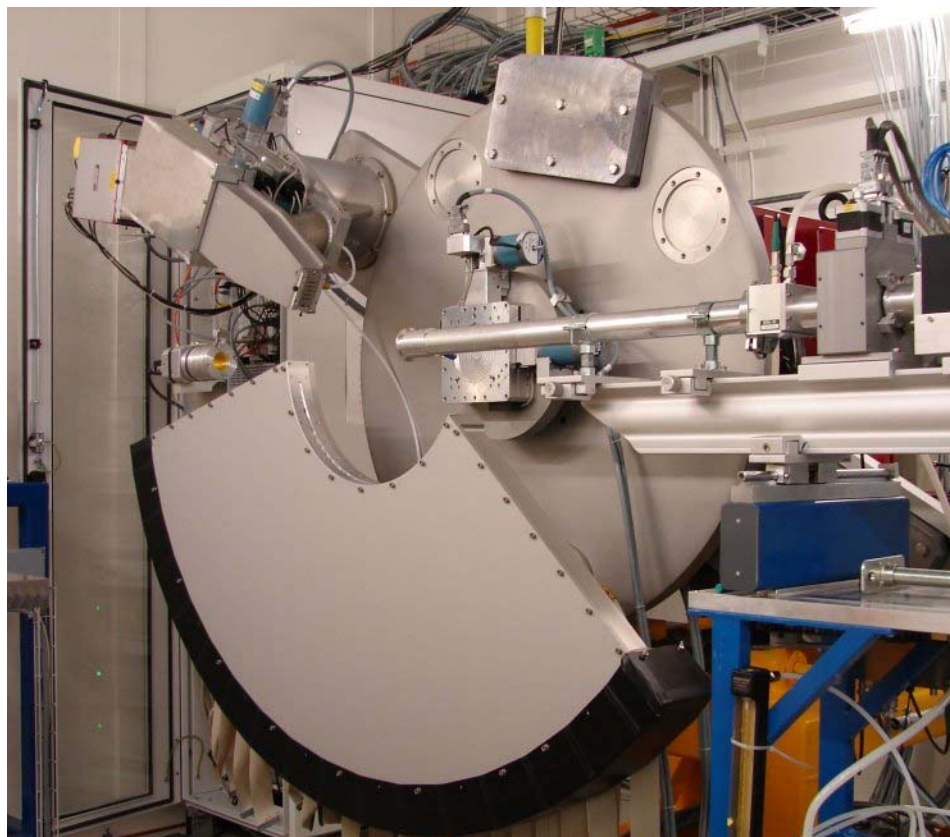


Figure 4.3: The Mythen II strip detector is composed of 30'720-elements, covering 120°.

4.2.5. Software

The data analysis was performed with the HORAE package, an EXAFS software including ATHENA and ARTEMIS [55-57]. In the data analysis, the Fourier transform (FT) of the EXAFS spectrum of an adapted theoretical model is fitted to the FT of the EXAFS spectra extracted from the experimental data. The applied models varied according to the sample composition and phase and they are introduced Chapter 3.

5. Results

In this chapter are introduced the results obtained during this thesis. In the 5.1 part the results from inactive binary alloy are introduced [34] with a special regard for the clusters size distribution. The part 5.2 concerns the Japanese Reference Quality (JRQ) [71] samples provided by the International Atomic Energy Agency (IAEA) on the local matrix damage [75]. Section 5.3 deals with the clusters formation [76]. The last part, 5.4, concerns the Kernkraftwerk Gösgen (KKG) surveillance samples provided by a real Nuclear Power Plant [77]. All the results presented in this chapter are obtained by x ray absorption fine structure spectroscopy (XAFS) except in section 5.1 where are used also transmission electron microscopy (TEM), energy dispersive spectrometry (EDS) and x ray diffraction (XRD).

5.1 Binary alloy

The binary alloy Fe 1.34 at % Cu is presented in the Section 4.1.1 and the applied model in Section 3.1.4.

5.1.1 EXAFS results

The normalized absorption spectrum (XANES) and the FT of the extracted EXAFS spectra of the samples A, B, C and D are shown in Figures 5.1A and 5.1B. For comparison in Figure 5.1 B also the absorption spectrum of Fe bulk and Cu bulk are presented. In Figure 5.1 A it can be clearly seen that samples A and B annealed for 2.5 and 8.0 h respectively look very similar to the Fe bulk. The FT of their EXAFS signals, represented in Figure 5.1 B, have similar structures: the first main peak has the same amplitude, while the following peaks between 3 and 5 Å of sample B are progressively smaller than those of sample A. This implies an increasing amount of disorder in sample B while still retaining the bcc structure.

Sample C was annealed for 115 h and contributions of the fcc precipitates are expected to increase. The absorption spectrum of sample C differs slightly from the spectra of samples A and B because the oscillations after the white line peak at around 8997 eV look smoother: a more disorder structure is expected. This characteristic is evident looking at Figure 5.1 B: the first main peak is significantly smaller then that of all the others samples and no peaks occur after the first.

Sample D, annealed for 312 hours, shows all the main structures of bulk Cu in Fig 5.1 A. From Figure 5.1 B it can be concluded that most of the Cu atoms reside in a fcc structure typical of Cu. The structure is a well defined fcc even at larger distances from the absorber. This situation is due to the formations of large precipitates. In Table 5.1 the variations of the threshold energy are introduced. Such variation is not reputed significant.

Table 5.1

ΔE_0 Threshold energy shift compared to Cu bulk (8979.0 eV). The experimental threshold energies are not significantly larger than the reference threshold energy.

Cu K-edge	REF	Sample A	Sample B	Sample C	Sample D
ΔE_0 (eV)	-0.5	-0.5	-0.4	-0.6	-0.1

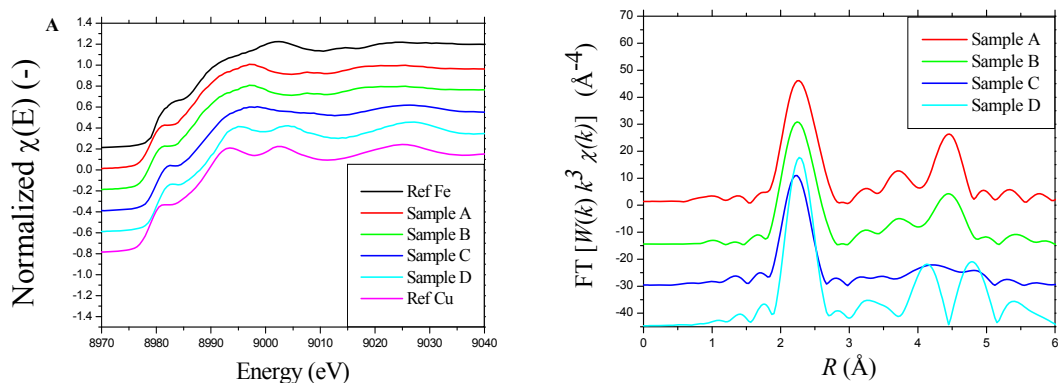


Figure 5.1 A: XANES spectra of the reference of Fe, Cu and of the four samples A, B, C and D. The references were analyzed at room temperature, the samples at 15 K. The reference of Fe is shifted to the Cu K edge. **5.1 B:** FT of the EXAFS signal of samples A, B, C and D. The samples A and B show a bcc structure, the sample D has a well defined fcc structure while the sample C shows an intermediate structure. Hanning function: $2 < k < 14 \text{ \AA}^{-1}$, $dk = 0.5 \text{ \AA}^{-1}$, k -weight = 3.

In order to evaluate the amount of Cu in bcc and fcc phases, linear combination fits (LCF) were performed on the absorption spectra of the samples B and C using the spectra of samples A and D instead of using Cu- and Fe-foil absorption data. The linear combinations are shown in Figure 5.2, revealing a significantly higher fit quality compared to the fits using the pure metal references. It means that, despite the well defined fcc peaks, sample D cannot be though a representative fcc sample.

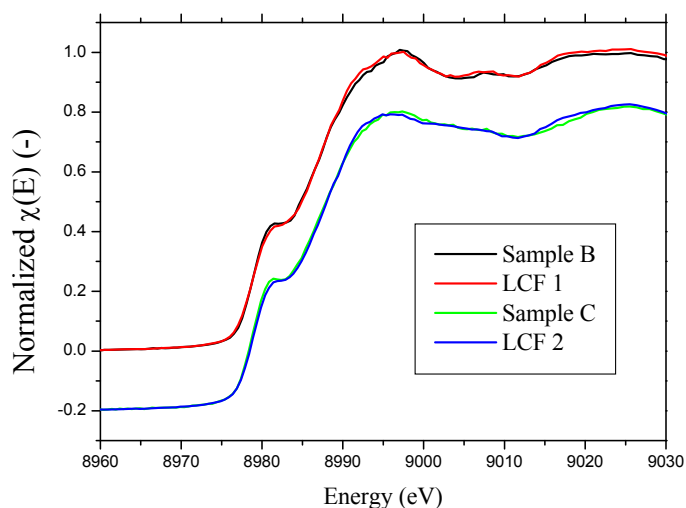


Figure 5.2: XANES spectrum of sample B fitted with the Linear Combination Fit (LCF 1) curve obtained with a contribution of sample A ($87 \pm 2 \%$) and samples D ($13 \pm 2 \%$). XANES spectrum of the sample C fitted with the Linear Combinations Fit (LCF 2) curve obtained with a contribution of sample A ($58 \pm 2 \%$) and sample D ($42 \pm 2 \%$).

The linear combination fits give some important quantitative information about the structure of samples B and C. The contributions of sample A, mainly based on bcc Fe-like structures, are $87 \pm 2\%$ and $58 \pm 2\%$ for the sample B and C respectively. The contributions of sample D mainly based on a fcc Cu-like structure are $13 \pm 2\%$ and $42 \pm 2\%$ for sample B and C respectively. The results of the EXAFS analysis are shown in Table 5.2.

It has to be pointed out that only the first main peak of the FT of the EXAFS signal was analyzed. This peak corresponds to the first and second shells in the bcc structure and only the first shell in fcc crystal. In order to reproduce the first peak of the FT, two input files (feff.inp) were used. Both of them were based on a mix structure of Cu and Fe atoms: the first had a pure bcc structure with the same parameters of Fe bulk (coordination number, distances) the second had a pure fcc structure with the same parameters of Cu bulk. The two phases are weighted by ' n^{bcc} ' and ' n^{fcc} ' (see Eq. 3.5-3.8) while the proportions between Cu-Fe and Cu-Cu first neighbors are weighted by ' x ' in the bcc and ' y ' in the fcc phase. Different Debye-Waller (DW) factors are assigned at the two phases [54].

Table 5.2

Cluster atom fractions (%) in the 1st (& 2nd) shell(s) around Cu for the sample A, B, C and D. Note that the fraction sum of the 'bcc phase' and 'fcc phase' is 100%, while 'Cu in bcc' and 'Cu in fcc' concern a fraction of the 'bcc phase' and 'fcc phase' respectively (see parameters in Eq. 3.5-3.8).

Atom fraction around Cu (%)	Sample A (2.5 h)	Sample B (8.0 h)	Sample C (115h)	Sample D (312h)
' n^{bcc} ' as bcc phase (1 st & 2 nd shells)	99 ± 1	87 ± 2	58 ± 1	1 ± 1
' $1-x$ ' as Cu in bcc (1 st & 2 nd shells)	0 ± 9	30 ± 9	88 ± 4	0*
' n^{fcc} ' as fcc phase (1 st shells)	1 ± 1	13 ± 2	42 ± 1	99 ± 1
' $1-y$ ' as Cu in fcc (1 st shell)	0*	96 ± 30	94 ± 4	92 ± 7

*Means below the detection limit (1%).

In order to reduce the large amount of free parameters that affect mainly the amplitude of the EXAFS signal FT (S_0^2 [54], n^{bcc} , n^{fcc} , x , y , all the DW factors), some simplifications are introduced. The data analysis of the first peak revealed that the amount of fcc and bcc phase, in samples A and D respectively, was below the detection limit (1%). Consequently the input files that concern the less important phases have been removed from the data analysis, with a strong reduction of the free parameters. In case of samples B and C, two input files were used, and the parameters ' n^{bcc} ' and ' n^{fcc} ' (see Eq. 3.5-3.8) have been set to the value found by LCF as shown above.

Despite these simplifications, the analysis could not be extended over the first FT peak, because the fit errors increase and quickly they can become larger than the data itself. Moreover some parameters are not constant over all shells, but they change. For example in samples A, B and C, ' x ', the fraction of iron atoms in the first two shells of bcc, increases up to '1' (100%) in the forth and fifth shells. This behavior is expected because of the limited size of bcc Cu clusters; consequently the iron matrix contribution becomes more and more important analyzing peaks far from the absorber such as those generated by the forth and fifth shell.

The high data quality and low temperature used (15 K) enable to investigate the difference between the Cu-Cu and Cu-Fe bonds only for the first FT peak. A similar

analysis has already been performed [76, 77] but because of the different experimental conditions (room temperature, more complex compositions and treatments of the samples) the determined error bars were much higher.

The fit results are compiled in Table 5.2 and it is possible to state that:

1. sample A shows a perfect Cu dilution with a purely iron-like structures;
2. sample B shows bcc and fcc clusters, they are small;
3. sample C shows that large clusters occur with high density of Cu atoms both bcc and fcc;
4. sample D shows that all Cu atoms are in a fcc structure, large and well defined clusters are expected.

5.1.2 TEM and EDS analysis

Sample D has been qualitatively analyzed by TEM and EDS and the results are shown in Fig 5.3. The TEM image (Fig 5.3) reveals the presence of a second phase with a darker contrast that can be considered as precipitates or large clusters rich in Cu, as shown in the upper EDS spectrum in Fig 5.4. Basically these are the clusters that were suggested by EXAFS (Section 3.1.3). Analyzing the EDS spectrum of the matrix (lower spectrum in Figure 5.4) it is possible to see that the copper signal is absent or only present as a trace, which proves that the matrix is almost copper free.

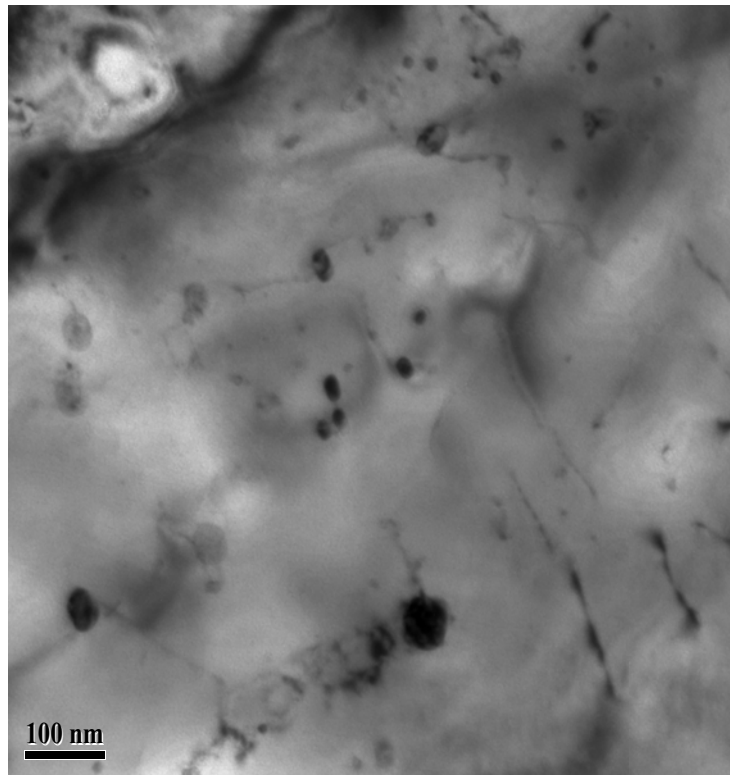


Figure 5.3: TEM bright field contrast image of sample D. Black spots are Cu clusters.

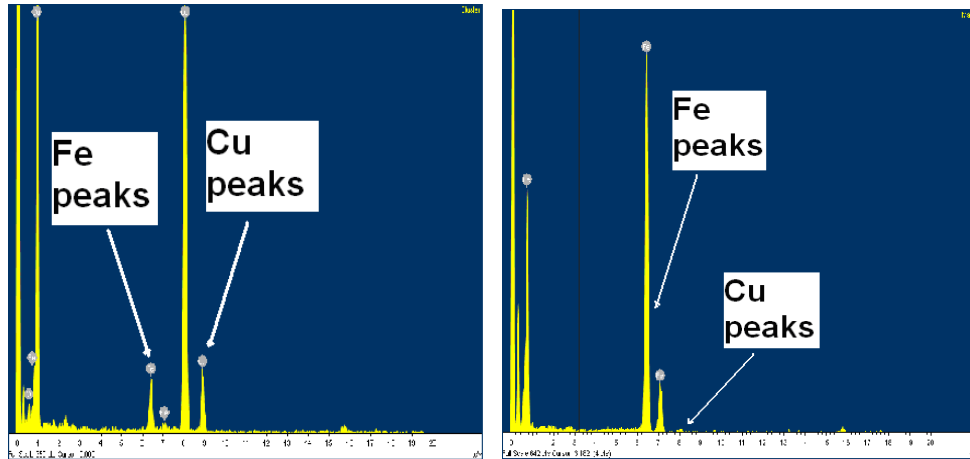


Figure 5.4: Qualitative EDS spectra of the copper precipitates (left) and of the matrix (right). Cu is absent in the matrix as confirmed by XAFS.

5.1.3 XRD data analysis and simulations

XRD is applied on all four samples. The XRD analysis is on preliminary results obtained by TEM analysis on sample D, such as: estimation of the maximum cluster size (~60 nm), cluster shape, amount of copper atoms in the matrix (EDS). Full-pattern XRD fits have been performed on the data. The bcc Fe Bragg peaks are modeled by Voigtian profiles [78]. Gaussian and Lorentzian widths are modelled with a generalized Cagliotti dependence, with additional corrections for the Finger-Cox-Jephcoat detector width effects [79]. This adds small anisotropic contributions on peaks at small diffraction angle. Nanometer-sized fcc-Cu clusters were modeled as in [48], assuming near-spherical clusters with a log-normal diameter distribution, in agreement with TEM results. Diameters ranged from 0.28 to 102 nm with 0.56 nm step. Lattice parameters of Fe and Cu resulted practically at nominal values (0.286609 nm and 0.361547 nm, respectively). Determination of fcc-Cu concentration was complicated by the high degree of texture in the Fe substrate. However, having collected data up to $Q = 4\pi (\sin \theta) / \lambda \approx 220 \text{ nm}^{-1}$, practically including all scattering from the sample, the problem was tackled by the powder pattern power theorem [80]. In the fcc richest sample D, mass concentration of fcc-Cu could be estimated to $0.434 \pm 0.013\%$. Of course it accounts only for the coherent domains, and especially the larger clusters. In other samples, preliminary estimations give $0.13 \pm 0.02\%$ (sample C, 115 h annealing), $0.09 \pm 0.02\%$ (Sample B, 8.0 h annealing) and $0.01 \pm 0.02\%$ (sample A, 2.5 h annealing) as shown in Table 5.3.

Table 5.3

Fcc phase found in the samples by XRD. In the second row is reported the fraction of the fcc phase found in each sample. In the third row is shown as the percentage of Cu in fcc: 100% would mean that all copper atoms are in fcc phase which would correspond to 1.34 at % of the alloy.

Fraction of	Sample A	Sample B	Sample C	Sample D
fcc (%)	0.01 ± 0.02	0.09 ± 0.02	0.13 ± 0.02	0.434 ± 0.013
Cu in fcc (%)	1 ± 2	7 ± 2	10 ± 2	33 ± 1

XRD analysis reveals that the size distribution in sample D is apparently very broad, with a number-averaged diameter of 8.4 nm and a variance of 40.3 nm^2 , extending to diameters well above 40 nm. Apparently this situation is similar in all samples, of course

with slight differences. Debye-Waller factors for the fcc-Cu phase seem reasonable, with an r.m.s. thermal displacement of 0.013 nm, pointing to a good degree of order in the fcc phase. As mentioned, the lattice parameters ratio between Fe and Cu is practically nominal, i.e. the difference is less than 10^{-4} . Due to the nearest neighbor bond length ratio of 1.03 (Fe/Cu), the presence of Fe in the fcc phase would change the lattice parameter according to Vegard's law, which suggests a concentration of Fe in fcc to be below 1%. The XRD patterns are shown in Figure 5.5 $12^\circ < 2\theta < 28^\circ$ with a special regard to the fcc peaks, while a complete XRD scan of the sample A is represented in the inset.

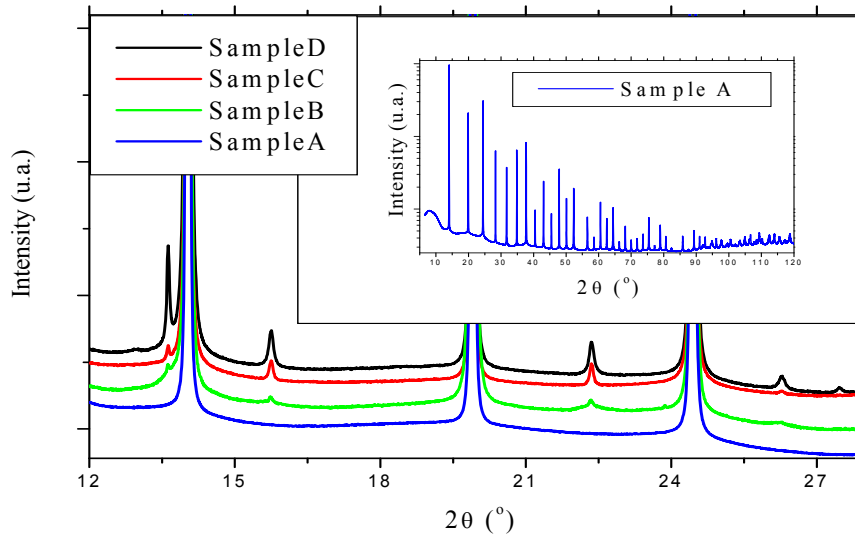


Figure 5.5: XRD spectra of samples A, B, C and D are reported in a linear scale. The main peaks are those of the bcc phase, while all the small peaks are those of the fcc phase. In the insert: complete spectrum of the sample A which is purely bcc (intensity in Log_{10} scale).

5.2 JRQ samples: matrix damage

This section concerns the investigation of the matrix damage by x ray absorption spectroscopy (XAFS). The matrix damage is investigated locally by the study of spectra collected at different K edges in order to underline differences. As presented in section 2.2.6 the defects, above all vacancies, are not expected to be uniformly distributed in the matrix, because the ‘bound’ between vacancy (or vacancies) and solute atoms are not the same for all the elements.

A reference sample, named REF_JRQ, and four active samples, named I (irradiated), IA (irradiated and annealed), IAR (irradiated, annealed and re-irradiated) and IARA (irradiated, annealed, re-irradiated and re-annealed) are presented. REF_JRQ, I and IA spectra are collected at the Mn, Fe, Ni, Cu K edge and of the IAR and IARA sample at the Cu and Ni K edge. Since Fe atoms are the main component of the matrix (~95 at %), the matrix damage is not expected to have a strong influence on the EXAFS spectra at the Fe K edge, while Mn, Ni and above all Cu K edges are more sensitive. This behavior points out the differences of each solute element giving also a confirmation of what found by positron annihilation spectroscopy and introduced in 2.2.6.

5.2.1. Atomic environment around Fe

The Fe K-edge EXAFS results, obtained for the high fluence I and IA specimens, are presented in this section. The results are shown in Figures 5.6 A and B. The left panel in the figure reports Fe K-edge XAS spectra. The lower panel plots FT data and the best-fitted curves. The EXAFS oscillations (inset in Figure 5.6 A) and the corresponding FT (inset in Figure 5.6 B) of I sample have similarities with those of IA specimen. Prolonged annealing after the neutron irradiation shows no influence on the Fe first- and second-nearest neighbor shells, although a small change in the higher order shells (third to fifth) of iron can be observed. Also, the Fe environment, reflected in both oscillation and FT data from the REF_JRQ sample (not shown here), is very similar to the results presented in Figure 5.6 B. Results of the first coordination shell fitting parameters obtained for I sample are: an Fe–Fe coordination number of 7.5 ± 0.3 at a distance $2.52 \pm 0.02 \text{ \AA}$, $\sigma^2 = (59 \pm 7) \times 10^{-4} \text{ \AA}^2$ and $\Delta E_0 = 9.6 \text{ eV}$; whereas the corresponding values for the second shell are $N_2 = 6.6 \pm 0.3$, $R = 2.89 \pm 0.02 \text{ \AA}$, $\sigma^2 = (59 \pm 7) \times 10^{-4} \text{ \AA}^2$ and $\Delta E_0 = 9.6 \text{ eV}$. The estimated errors are the standard ones for EXAFS. These values are in agreement with the parameters known in the literature [81] for a bcc unit-cell of an Fe lattice. Describing the situation for the annealed one (IA specimen), the best fit is obtained with similar values for first two shells. The main structural difference between the two samples is the Debye Waller factors of higher order shells. For the third shell we measure $\sigma^2 = (77 \pm 6) \times 10^{-4} \text{ \AA}^2$ in sample I, and in IA $\sigma^2 = (69 \pm 5) \times 10^{-4} \text{ \AA}^2$. Theoretical FEFF calculations [82] indicate the expected larger value of σ^2 observed for this shell. In fact, from the data measured at the Fe K-edge and their analyses, no essential structural changes in the first two near-neighbor shells are observed between the REF_JRQ and irradiated steel specimen. Nevertheless, following few remarks may be relevant in connection with the results obtained here.

In recent years, several studies of defect evolution in irradiated Fe and Fe–Cu alloys from atomistic simulations have been undertaken describing the role of intracascade point defects clustering including correlated recombination [83, 84], defect transport properties [85], and binding as well as stability of vacancy-solute clusters [86]. Representative experimental study [87] of Fe irradiated at 310 K by neutrons showed consistent results: in almost all the microstructures resolved by the TEM technique were interstitial type dislocation loops, and no vacancy type defect was observed. Vacancies introduced by cascades in the Fe lattice form clusters by primarily agglomerating in small regions, but such formed clusters are not stable at temperatures that is close to the RPV operation temperature of 563 K. Specific computer simulations of the cascade and defect microstructure evolution have predicted results also in the same direction: the size and fraction of self-interstitial atoms clusters are larger in Cu than in Fe [88]. The vacancies on the other hand, are in Cu mostly in the form of clusters, while they do not form clusters in Fe [89].

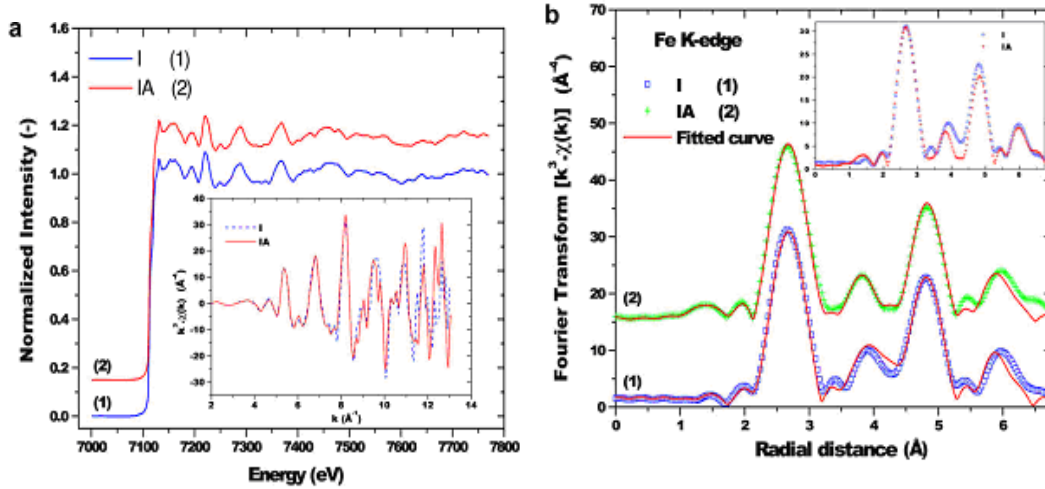


Figure 5.6 A and B: Normalized absorption spectra at the Fe k edge (a) of the sample I and IA. The corresponding radial distribution (b) phase-shift corrected. In the insets experimental FT data of the two samples are shown in the overlap mode.

5.2.2 Atomic environment around Mn, Ni and Cu

Examples of measured absorption spectra at the Mn, Ni and Cu K edges from the reference (i.e., unirradiated, REF_JRQ) RPV steel sample are shown in Figures 5.7 A, B and C. The data presented in the inset of Figures 5.7 A, in the insets of Fig 5.9 A and B and 5.10 A and B, clearly indicate good quality EXAFS in the spectral k range of 2-10.5 \AA^{-1} .

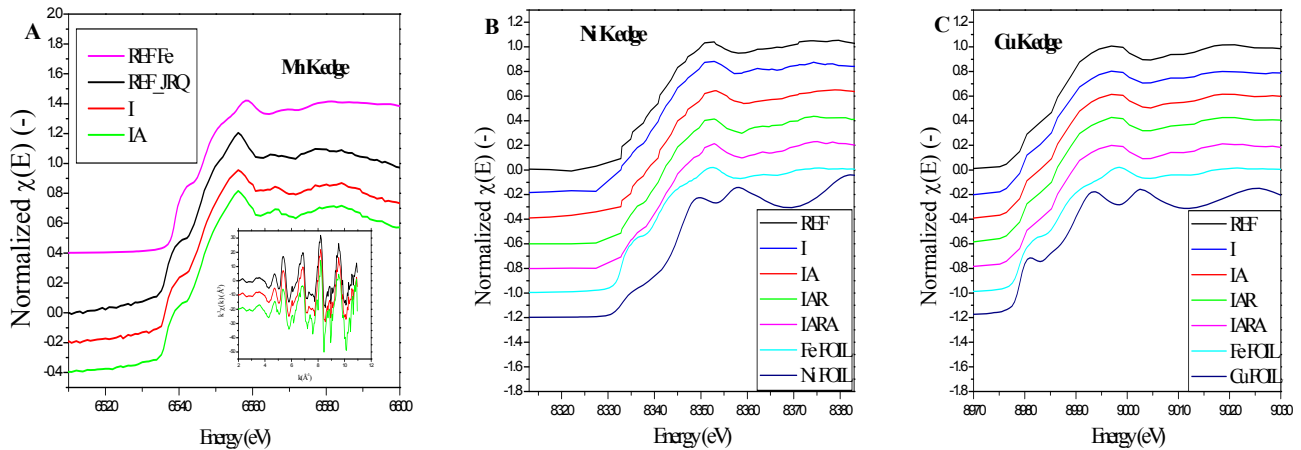


Figure 5.7 A, B and C: The normalized absorption spectra of Fe foil, REF_JRQ, I and IA samples collected at the Mn (A) at the Ni (B) and at the Cu K-edge (C). For better comparability, the energy of the Fe K-edge (7112 eV) is shifted to the energy of the Mn, Ni and Cu K-edge.

Figures 5.8 A, B and C plot Fourier transformed EXAFS spectra for the REF sample as well as that of four neutron-irradiated and annealed RPV steels. In all cases the EXAFS data was weighted by a Hanning window and the range transformed extends with $3.0 < k < 10.5 \text{ \AA}^{-1}$. The spectra drawn with symbols and solid lines are the measured and

corresponding best-fitted one, respectively. Table 5.4 contains the analyzed numerical results for all these specimens. In the insets in Figures 5.8 A, B and C, experimental FT data of all samples for each absorber element are shown in the overlap mode to identify structural differences from a preliminary inspection of the data. Information about the local structure in this REF sample is, therefore, obtained by fitting these data with corresponding atomic scattering functions calculated using FEFF [82].

Table 5.4

Results of the EXAFS analysis on Cu, Ni and Mn sites in neutron irradiated RPV steels. The EXAFS result of the unirradiated REF_JRQ sample is also shown for a comparison. S_0^2 denotes the amplitude reduction factor, α is the scaling factor and σ^2 represent the Debye Waller factor. See the text for further details.

Absorber atom	Samples	Over all scaling factor (α)	$\sigma_{1,2}^2 (\times 10^{-4})$ (\AA^2) 1 st and 2 nd shell	$\sigma^2 (\times 10^{-4})$ (\AA^2) 3 rd shell	$\sigma^2 (\times 10^{-4})$ (\AA^2) 4 th shell	Quality factor $\mathcal{R}(\%)$
Cu	REF_JRQ	(1.00)	45 (± 6)	59	42	1.5
	I	0.73	50	82	63	1.6
	IA	0.80	43	77	46	0.9
	IAR	0.83	46	67	59	1.7
	IARA	0.88	49	82	67	0.3
Ni	REF_JRQ	(1.00)	42	69	109	0.5
	I	0.73	38	79	157	0.7
	IA	0.89	57	65	85	0.5
	IAR	0.92	42	71	85	0.9
	IARA	0.92	42	78	106	0.3
Mn	REF_JRQ	(1.00)	32	68	68	1.4
	I	0.76	36	86	87	1.8
	IA	0.83	29	74	74	1.0

The analysis using FEFF model of the bcc Fe lattice structure yielded a good fit to the experimental data. The starting FEFF model comprises all single scattering paths within the fit range and all multiple scattering paths up to 6.0 \AA . The single scattering peaks around Cu, Ni and Mn sites are surrounded by 8 Fe atoms at 2.49 \AA , 6 at 2.87 \AA , 12 at 4.06 \AA , 24 at 4.76 \AA and 8 at 4.97 \AA in the first five consecutive neighbor shells. The refined values (see Table 5.4) obtained from the curve fit give realistic DW factors, correct order for the bonds, and appropriate coordination for the first five consecutive neighbor shells. All data in Figures 5.8 (A, B and C) have also been corrected for electron phase shifts using the 1st shell-path from FEFF and therefore the FT peaks should correspond directly with the true bond distances of the near neighbors. At this point let us remind that Cu and Ni atoms, if compared to Fe in terms of their sizes, behave as equivalent backscatters, and indistinguishable from the XAS point of view. Therefore, in our present analysis, the local environment of solute atoms (i.e., Cu, Ni and even Mn) has been deduced assuming only one kind of neighbor for the central atom residing in a bcc-cluster of Fe lattice. Thus, the contributions from Cu-Fe correlation (for example) in the FT peak imply the results of Cu-Fe (Cu, Ni or Mn) atoms-shell in practice, Cu being the central atom. Dealing with neutron irradiated samples, the RDFs exhibit remarkable differences in many respects. Significant radiation damage effects are readily apparent in

the raw data. An overall similarity of Cu, Ni and Mn atomic environment in the iron matrix is observed.

Preliminary fits to the data from these irradiated samples showed that the decrease in amplitude is due to both a decrease in the amplitude reduction factor S_0^2 and an increase in each atom of the mean square relative displacement σ^2 with total neutron fluence. Since the EXAFS amplitude for a given shell is proportional to both $N_{l,2}$ and $1/\sigma$, damping due to disorder results from the disorder-induced increase of the DW factor and the decrease of coordination numbers in each shell. To quantify this damage resulting from neutron irradiation effects, we therefore introduce in our analysis an overall scaling factor (α) multiplied to the term S_0^2 . This parameter α should describe the damaged fraction in the irradiated RPV steel lattice. The fits to the EXAFS spectra of irradiated samples were done in R-space. In the fitting procedure the coordination number was fixed to the nominal value for each scattering path. The amplitude reduction factor S_0^2 was also constrained to be the best-fit values of 0.85, 0.83 and 0.87 for Cu, Ni and Mn K-edge data, respectively. These values were derived from the data of REF_JRQ sample. The data were analyzed in two steps. First, a two-shell fit for the nearest Cu-Fe (also similar for Ni and Mn edge data) coordination was done in the R range of $1.5 < R < 3.5$ Å by varying bond lengths R , DW factor, and shift of the energy origin ΔE_0 . Second, in the fits for higher shells in the R range from 3.5 to 6.0 Å, σ^2 and R for each path were treated as adjustable parameters, while ΔE_0 was fixed to the best-fit value for the first two shells. In this way, the correlation between R and ΔE_0 was reduced, and hence the number of free parameters in the fits. This approximation is reasonable, since Cu (or Ni) and Fe have the similarity in their ionic radii, and have very close values of electronegativity [90]. Therefore, the electrostatic potentials induced by charge transfer between Cu and Fe atoms can be neglected, and the approximation of neutral absorber atom assumed by FEFF is valid, so that an overall ΔE_0 is enough for all scattering events. The overall fitting results are shown in Figures 5.8 (A, B and C) as continuous lines superimposed on the data points. The best-fit structural parameters are summarized in Table 5.4. The values for interatomic distances R are not mentioned in Table 5.4 as they were found not being affected by the neutron irradiations and within the experimental uncertainties. Considering the information derived from EXAFS analyses following conclusions can be drawn from Table 5.4. The main difference in the local structural parameters due to irradiations is a systematic change in overall scaling factor α that relates changes in the coordination numbers in nearest-neighbor atomic shells, and an increase in the DW factors upon irradiation and post-irradiation annealing. These results are not graphically depicted since they are also partly evident in the RDFs spectra shown in Figure 5.8 (A, B and C) (see the insets). The progressive decrease of the nearest-neighbor peak-amplitude is indicative of an increase in the number of displaced atoms (point defects) in the vicinity of the absorbing atoms, produced by a primary knock-on atom (PKA) with a given kinetic energy. During prolonged neutron irradiations the creation of these primary point defects (in terms of vacancies and interstitials atom) is extremely high, and they also have a much higher probability of reacting with themselves. This means, in the case of an interstitial and a vacancy reaction simply results in annihilation but in the case of vacancies can result in the production of the di-vacancy or higher order vacancy complexes. Moreover vacancies form tight bonds with Cu atoms as reported in Chapter 2 (see Ref [25]). Consequently a local large disorder near the absorber (Ni and Cu) is

expected. Therefore, it is reasonable to consider that the decrease in the coordination numbers in next neighbor shells upon irradiation is caused, at least partly, by simple point defects and/or their agglomerates associated with each of the constituent solute atoms in RPV steel. Upon post-irradiation-annealing at higher temperatures, the vacancy- and interstitial-like defects that do not recombine may, respectively, preferentially diffuse to void like sinks and self-anneal through bond rearrangements with nearest neighbors. A reduced fraction of defects will thus retain within the bulk. During formation of these defects, copper together with other alloying elements leads to precipitation of nano-precipitates, and also induces matrix hardening and embrittlement. This precipitation effect is expected to saturate due to the progressive reduction of available precipitable elements in solid solution, copper in particular. Furthermore, other light elements, like phosphorus or sulphur, can segregate inside the grains interacting with matrix defects (i.e., vacancies, interstitials, dislocation loops), or migrate to grain boundaries, or may be attracted to the Cu-type precipitates. Diffusion of segregates also plays a role. One can furthermore note from Table 5.4 that changes in σ^2 , or equivalently, the mean-square relative displacement of the interatomic distance distribution, is more pronounced in the higher shells (third to fifth). Apparent changes upon relaxations observed in σ^2 for the first two shells are not significant in the irradiated samples relative to the REF_JRQ sample, yielding an average value of 0.0046, 0.0044 and 0.0032 Å² for the Cu, Ni and Mn atomic neighbors, respectively. In contrast, σ^2 is increased from 0.0059 to 0.0082 Å² in the third shell in high fluence 5.0×10^{19} cm⁻² sample, with a significantly lesser change apparent due to post-irradiation annealing. Similar behavior can be also observed for the lowest dose IAR and IARA samples. These trends remain consistent in the measured σ^2 data of fourth- and fifth-shells neighbors. In all cases of the annealed specimens the structures are not well-ordered beyond the first two coordination shells. While it is difficult to propose a unique structural model accounting the actual lattice positions of all Cu, Ni and Mn atoms in Fe, and it is highly probable that in these irradiated steels Cu, Ni and Mn are present in a number of different local configurations (e.g., strained and/or distorted lattice positions, ultrafine clusters in a bcc environment etc.), the following remarks may be relevant in connections with our results obtained from EXAFS experiments. The accumulated local damage after irradiation in sample I is measured as about 26% from the point of view of each of the constituent solute atoms in RPV steel. This amount of radiation damage is obtained from the value of α , which was found to decrease greatly on irradiation that is from 1.0 to 0.74 (an average value calculated from the Cu, Ni and Mn data) in this sample. Thermal annealing at 735 K for duration of 168 h induces a local ordering and improves the crystallinity in this sample as manifested by a reduced damage fraction close to 16%. The estimated damage in the lowest dose IAR and IARA (measured only at the Cu and Ni K-edges) samples vary between 10% and 12%. These values of the retained damage are not directly correlated with the dpa parameter for characterizing the radiation damage level in these samples. The local matrix damage enhancement, while possibly indicating more defects than expected, may also indicate significantly more defect-induced lattice strain and distortions. Therefore, it is important to mention that the matrix damage reported here should be interpreted as a collection of surviving point defect clusters resulting from vacancies and self-interstitial atoms, loops and nano-voids, as evolved with temperature and time, and interacting with solute atoms

and elements of the microstructure to promote formation and growth of the mentioned nano-scale features [75, 91, 92].

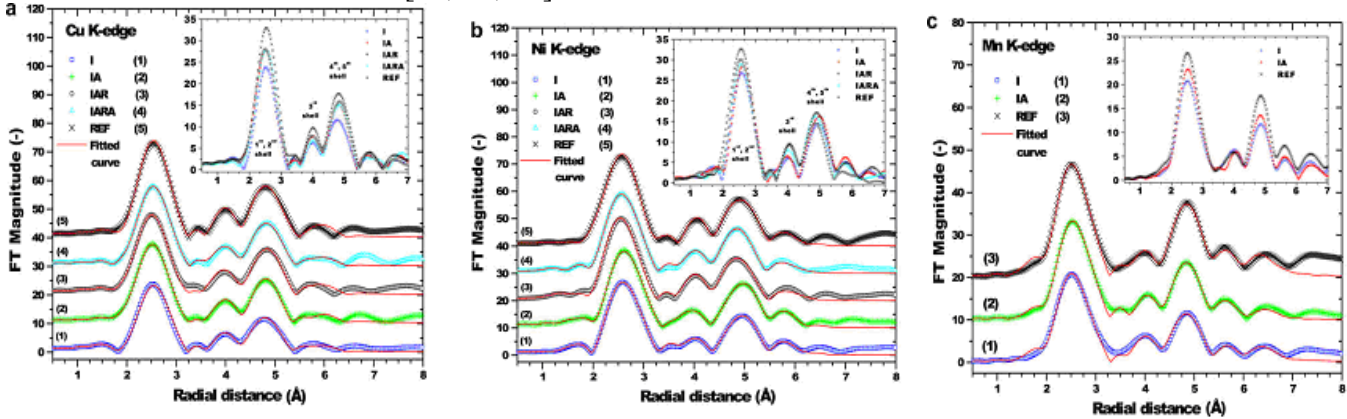


Figure 5.8 A, B and C: the FT of the Cu edge data (a), Ni edge data (b) and Mn edge data (c). are shown; $3.0 < k < 10.5 \text{ \AA}^{-1}$. The data points are provided with symbols and continuous lines represent the best fit to the data. In the insets experimental FT data of all samples are shown in the overlap mode.

5.3 JRQ samples: cluster formation

This section concerns the XAFS results of the reference sample REF_JRQ, I (irradiated), IA (irradiated and annealed), IAR (irradiated, annealed and re-irradiated) and IARA (irradiated, annealed, re-irradiated and re-annealed), collected at the Ni and Cu K edge. The sample composition and treatment are introduced in detail in section 4.1.2. In the previous section the matrix damage is introduced and the local disorder is calculated near the absorbing atoms. Here a detailed investigation of the chemical composition near the absorbing atoms is provided in order to detect high local concentration of solute atoms. Local high density of solute atoms brings to cluster formation and it is important to verify which elements are the most involved.

Since the most important solute elements in reactor pressure vessel steels are Cu and Ni and since they crystallize in fcc structure while Fe does in bcc, XAFS spectroscopy can provide very sensitive information about eventual phase changes.

5.3.1 XANES: Cu and Ni K-edge

XANES analysis provides a fingerprint of the atomic environment of Cu and Ni in the iron matrix. In fact a significant change in the absorption edge energy and/or shape could be due to a change in the crystallographic structure. Phase changes were observed in previous studies in the case of annealed ternary and quaternary Fe-based alloys [18].

The XANES spectra at the Ni and Cu K-edge are presented in Figures 5.7 B and C respectively. The samples spectra look rather similar: significant energy shifts (for both Cu and Ni) were not detected (see Table 5.5) and the shape of the K-edge is very similar to that of the Fe pure foil. This means that the crystallographic structure around the absorber is very close to the body centred cubic of pure iron. No phase changes are detected. The fcc crystallographic structure of pure Cu and Ni foils is expected to yield two typical maxima on the top of the absorption edge [93]. However, these peaks are not detected in the present work as shown in Figures 5.7 B and C.

Table 5.5

ΔE_0 Threshold energy shift compared to Cu bulk (8979.0 eV) and to Ni bulk (8333.0 eV). The experimental threshold energies are not significantly larger than the reference threshold energy.

	REF	I	IA	IAR	IARA
Cu K-edge, ΔE_0 (eV)	0.2 ± 0.1	0.3 ± 0.2	0.3 ± 0.2	0.3 ± 0.2	0.3 ± 0.2
Ni K-edge, ΔE_0 (eV)	0.2 ± 0.1	0.0 ± 0.2	0.3 ± 0.2	0.3 ± 0.2	0.4 ± 0.2

5.3.2 EXAFS: Cu K-edge

The experimental data gained from the Cu K-edge analysis are displayed in Figures 5.9A and B, and the results are shown in Table 5.6. The analysis of the reference sample was (independently) performed on the two set of experimental data collected at 15 K (measured at ANKA) and at room temperature (measured at SLS). Only data collected under the same experimental conditions can be compared. Unfortunately, the irradiated samples could not be analyzed at 15 K. The data collected at 15 K show a lower background noise. They reveal the same amount of Cu and Ni atom in the first and second shells as the reference sample analyzed at RT. Consequently the RT reference analysis was performed setting the x, y values, the same as at 15 K. For the irradiated samples analysis the parameters from the reference REF measured in SLS at RT were used: S_0^2 and $E-E_0$.

The energy shifts (ΔE_0) are too small to be significant for both XANES and EXAFS analysis. Two quality factors \mathcal{R} are reported in Table 5.6. \mathcal{R}_{Fe} is the quality factor estimated for an atomic environment composed only of iron around the Cu absorber while $\mathcal{R}_{Fe,Cu}$ is used for a binary environment composed of iron and copper [17]. It is commonly accepted that the decrease of $\mathcal{R}_{Fe,Cu}$ is physically significant if $\mathcal{R}_{Fe}/\mathcal{R}_{Fe,Cu} > 2$, and in this case the importance of number of Cu (or Ni) atoms in the 1st and 2nd shell is fundamental to get a result closer to the real sample structure. In the case of Cu K-edge the gap between \mathcal{R}_{Fe} and $\mathcal{R}_{Fe,Cu}$ is not as large as in the case of Ni K-edge. This different behaviour is due to the small amount of Cu compared to Ni. Δr is the difference in atomic distances between the absorber and the 1st and 2nd shell atoms (see Table 5.6). The Debye Waller factor $e^{-2k^2\sigma^2}$ is a function of the mean square relative displacement σ^2 , the measure of oscillation around the equilibrium position due to thermal and statistic disorders. σ^2 for the first shell is lower than the σ^2 for the second shell. This change is due to interstitials, and to the complex composition of the samples compared to the theoretical model applied. It has to be pointed out that σ^2 for the 1st shell is correlated to σ^2 for the 2nd shell, so the recorded disorder is common to both shells. Moreover, the comparison between the REF samples, measured at 15 K and at room temperature, has to take into account the high correlation between the first and second shell atoms. This high correlation makes any consideration on a single shell difficult without considering the other one. For instance, the σ^2 for the first shell of the REF sample at 15 K is larger than all the other first shell σ^2 measured at room temperature; this can be understood only considering the second shell σ^2 value. Considering the average between the first and second shell σ^2 an increase of the noise is observed as expected.

Table 5.6

Comparison of quality factor (\mathcal{R}_{Fe} , $\mathcal{R}_{\text{Fe,Cu}}$), distance shift (Δr), the mean square relative displacement (σ^2), number of atoms in the first and second shell (N) and number of Cu and Ni atoms in the two first shells at the Cu K-edge ($N_{\text{Cu,Ni}}$). The distance shift Δr is compared to the theoretical model (first shell distance: 2.539 Å; second shell distance: 2.932 Å).

Cu K-edge	shell	REF (15 K)	REF (RT)	I	IA	IAR	IARA
\mathcal{R}_{Fe}		0.0003	0.0022	0.0064	0.0043	0.0077	0.0046
$\mathcal{R}_{\text{Fe,Cu}}$		0.0001	0.0014	0.0049	0.0034	0.0055	0.0026
Δr (Å)	1 st	-0.06 ± 0.02	-0.06 ± 0.01	-0.05 ± 0.01	-0.06 ± 0.01	-0.06 ± 0.07	-0.06 ± 0.01
σ^2 (Å ²)		0.005 ± 0.001	0.002 ± 0.001	0.003 ± 0.004	0.003 ± 0.001	0.003 ± 0.001	0.002 ± 0.001
Δr (Å)	2 nd	-0.11 ± 0.01	-0.09 ± 0.01	-0.09 ± 0.02	0.02 ± 0.03	-0.02 ± 0.04	-0.05 ± 0.04
σ^2 (Å ²)		0.005 ± 0.002	0.013 ± 0.002	0.019 ± 0.005	0.018 ± 0.005	0.018 ± 0.006	0.028 ± 0.007
$N_{1,2}$	1 st &	14.0 ± 0.1	14.0 ± 0.1	12.5 ± 0.4	13.3 ± 0.4	13.3 ± 0.5	13.3 ± 0.4
$N_{\text{Cu,Ni}}$	2 nd	1 ± 1	1 ± 1	0 ± 3	9 ± 2	7 ± 4	8 ± 3

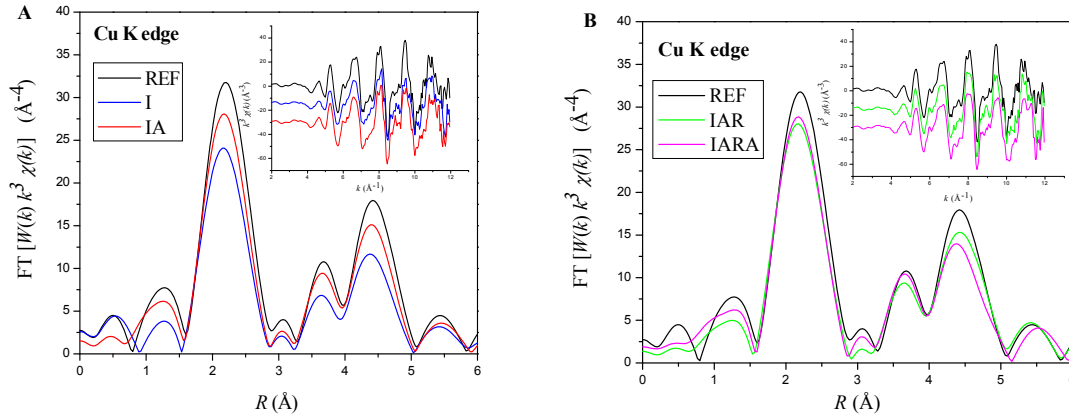


Figure 5.9 A and B: The Fourier transform of the reference samples (REF), the irradiated (I) and the irradiated and annealed (IA) samples (Fig 5.9A). The FT of the reference samples REF, the irradiated, annealed and re-irradiated (IAR), and the irradiated, annealed and re-irradiated and re-annealed (IARA) sample (Fig 5.9B). Conditions: $W(k)$ is the Hanning function $4 < k < 10.3 \text{ \AA}^{-1}$, $dk = 0.5 \text{ \AA}^{-1}$; conditions see Table 5.6.

5.3.3 EXAFS: Ni K-edge

The experimental data gained from the Ni K-edge analysis are displayed in Figures 5.10 A and B, and the results are shown in Table 5.7. These data were collected only at room temperature. From the analysis of the reference sample S_0^2 and $E-E_0$ have been determined and they have been introduced in the irradiated sample analysis, as it was done for the Cu K-edge. The difference between \mathcal{R}_{Fe} and $\mathcal{R}_{\text{Fe,Cu}}$ is significant. The larger amount of Ni increased the quality of the data. Consequently $\mathcal{R}_{\text{Fe,Cu}}$, calculated at the Ni K-edge, is smaller than the $\mathcal{R}_{\text{Fe,Cu}}$ at Cu K-edge for all the samples. Moreover the $N_{\text{Cu,Ni}}$ uncertainty at Ni K-edge is smaller than $N_{\text{Cu,Ni}}$ at the Cu K-edge (with the only exception of sample IA).

Table 5.7

Comparison of quality factor (\mathcal{R}_{Fe} , $\mathcal{R}_{\text{Fe,Cu}}$), distance shift (Δr), the mean square relative displacement (σ^2), the number of atoms in the first and second shells (N) and numbers of Cu and Ni atoms in the two first shells at the Ni K-edge ($N_{\text{Cu,Ni}}$). The distance shift Δr is compared to the theoretical model (first shell distance: 2.539 Å; second shell distance: 2.932 Å).

Ni K-edge	shell	REF (RT)	I	IA	IAR	IARA
\mathcal{R}_{Fe}		0.0017	0.0019	0.0058	0.0025	0.0017
$\mathcal{R}_{\text{Fe,Cu}}$		0.0007	0.0008	0.0012	0.0002	0.0002
Δr (Å)	1 st	-0.07 ± 0.02	-0.07 ± 0.01	-0.08 ± 0.01	-0.09 ± 0.01	-0.09 ± 0.01
σ^2 (Å ²)	1 st	0.005 ± 0.001	0.007 ± 0.001	0.005 ± 0.001	0.006 ± 0.001	0.006 ± 0.001
Δr (Å)	2 nd	-0.11 ± 0.01	-0.10 ± 0.01	-0.10 ± 0.01	-0.12 ± 0.01	-0.10 ± 0.01
σ^2 (Å ²)	2 nd	0.006 ± 0.001	0.005 ± 0.005	0.012 ± 0.001	0.005 ± 0.001	0.006 ± 0.001
$N_{1,2}$	1 st &	14.0 ± 0.1	12.5 ± 0.4	13.3 ± 0.3	13.3 ± 0.3	13.3 ± 0.1
$N_{\text{Cu,Ni}}$	2 nd	0 ± 1	0 ± 3	7 ± 3	7 ± 1	6 ± 1

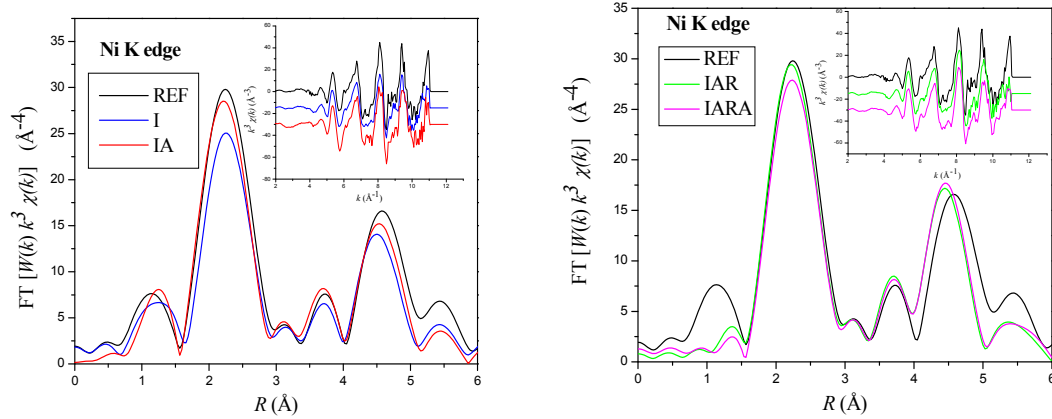


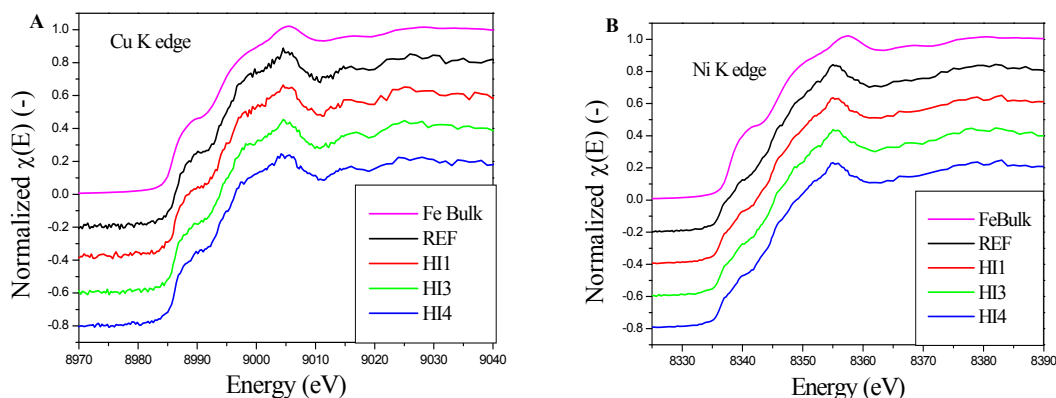
Figure 5.10 A and B: The FT of the reference samples REF, the irradiated (I) and irradiated and annealed (IA) (Fig 5.10A). The FT of the reference sample REF, the irradiated, annealed and reirradiated sample (IAR) and finally again annealed sample (IARA) are represented in (Fig 5.10B). Conditions: $W(k)$ is the Hanning function $4 < k < 10.3 \text{ \AA}^{-1}$, $dk = 0.5 \text{ \AA}^{-1}$; conditions see Table 5.7.

5.4 KKG samples: cluster formation

In this section the samples introduced in section 4.1.3 and provided by the Gösgen Power Plant are analyzed by EXAFS.

5.4.1 XANES: Cu and Ni K edge

The theoretical spectrum is calculated with feff.inp, an input file based on crystallographic assumptions. Firstly it was assumed that the steel matrix has the same crystallographic structure as pure iron which is ~ 97 % of the steel. This assumption was confirmed to be correct from the shape of the absorption edge (Figures 5.11 A and B). Two different environments were used, Fe-Cu and Fe-Ni. For both, the same results were obtained and finally the environment Fe-Cu was chosen with which all the data were analyzed. As previously noted it is not possible to differentiate between Cu and Ni. Consequently $N_{\text{Cu,Ni}}$ is the sum of Cu and Ni atoms in the two first shells.

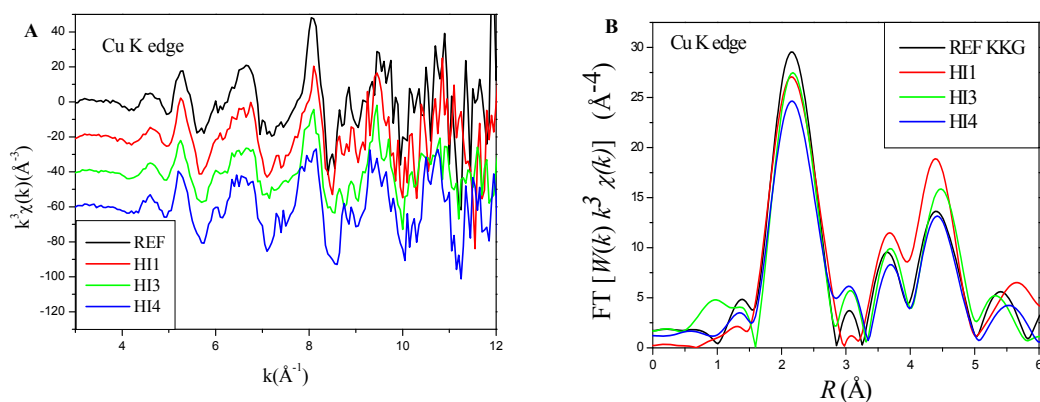


Figures 5.11 A and B: The spectra of Fe bulk of REF, HI1, HI3 and HI4 at the Cu (left) and Ni (right) K edge. Fe spectra were shifted manually to Cu and Ni K edge.

5.4.2 EXAFS: Cu K-edge

Experimental EXAFS spectra, their FT and the results obtained from the detailed analysis at the Cu K-edge are shown in Figures 5.12 A and B and Table 5.8. The analysis of the reference sample was (independently) performed on the two sets of experimental data collected at 15 K (measured at ANKA) and at room temperature (measured at SLS). Only data collected under the same experimental conditions can be directly compared because of the thermal expansion of the lattice and the temperature dependence of the lattice vibrations. Unfortunately, it was not possible to investigate the irradiated samples at 15 K, which would have been favourable because the EXAFS oscillations are more pronounced due to the reduced amplitude of the lattice vibrations at low temperatures.

As major results, however, the experiments at cryogenic temperature and at room temperature reveal the same amount of Cu and Ni atoms in the first and second shells. Consequently the RT reference analysis was performed setting the x, y values to those values which were obtained at 15 K. The data analysis was performed on the Fourier Transform of the EXAFS signal (Figures 5.12 A and B). The EXAFS spectra were firstly increased by a factor k^3 to point out the contribution at high k and then filtered by a Hanning window $W(k)$ with $4 \text{ \AA}^{-1} < k < 11 \text{ \AA}^{-1}$, $dk = 0.5 \text{ \AA}^{-1}$ (Figures 5.12 A and B).



Figures 5.12 A and B: The EXAFS spectra $\chi(k)$ of the sample REF, HI1, HI3 and HI4 at the Cu K edge. $\chi(k)*k^3$ is used to increase the contribution at large k (Fig 12 A). The FT of REF, HI1, HI3 and HI4 at the Cu K edge are represented in Fig 12 B. The conditions of the windows are: $W(k)$ is the Hanning function $4 \text{ \AA}^{-1} < k < 11 \text{ \AA}^{-1}$, $dk = 0.5 \text{ \AA}^{-1}$.

As can be seen in Figure 5.12 B, the overall shape of the FT data is unchanged but reduced in amplitude after irradiation of the RPV steels. Due to the limited data quality, investigations of the 3rd shell and beyond were not performed here because the results would be affected by large uncertainties. However, the results determined by a detailed analysis of the two first shells have reasonable error limits. In Table 5.8, the most important parameters obtained from the detailed data analysis are compiled. Δr is the difference in the atomic distances for the 1st and 2nd shell atoms, determined by the fit and the model structure which was the basis for the ab-initio calculation of the EXAFS by FEFF. The Debye Waller factor $e^{-2k^2\sigma^2}$ is a function of the mean square relative displacement σ^2 , the measure of the variation around the equilibrium position due to thermal and static disorders. σ^2 for the first shell is lower than the σ^2 for the second shell. This change is due to interstitials, and to the complex composition of the samples compared to the theoretical model applied. It has to be pointed out that σ^2 for the 1st shell is correlated to σ^2 for the 2nd shell, so the recorded disorder is common to both shells. Moreover, the comparison between the REF samples, measured at 15 K and at room temperature, has to take into account the high correlation between the first and second shell atoms. This high correlation makes any consideration on a single shell difficult without considering the other one. For instance, the σ^2 for the first shell of the REF sample at 15 K is larger than all the other first shell σ^2 measured at room temperature; this can be understood only considering the second shell σ^2 value. Considering the average between the first and second shell σ^2 an increase of the noise is observed as expected.

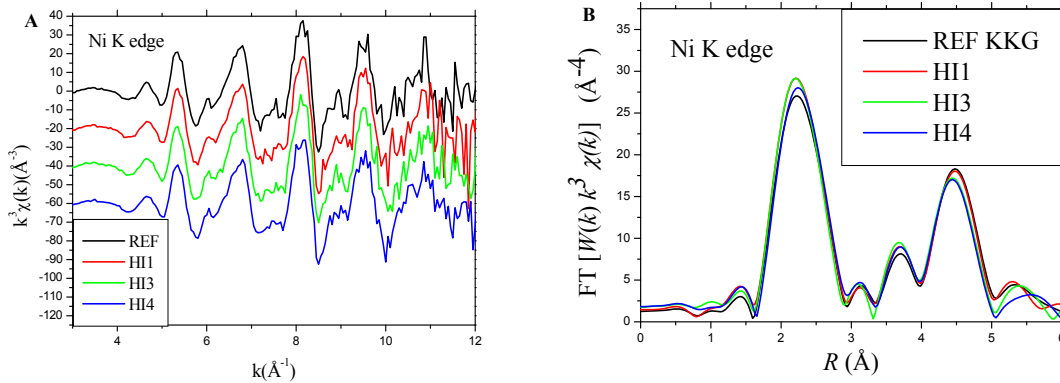
Table 5.8

Comparison of the distance shift (Δr), the mean square relative displacement (σ^2), number of atoms in the first and second shell (N) and number of Cu and Ni atoms in the two first shells at the Cu K-edge ($N_{Cu,Ni}$) as determined by a fit of the measured EXAFS. The distance shift Δr is compared to the theoretical model (first shell distance: 2.482 ± 0.001 Å; second shell distance: 2.867 ± 0.001 Å for bcc Fe).

Cu K-edge	shell	REF (15K)	REF (RT)	HI1	HI3	HI4
Δr (Å)	1 st	-0.030 ± 0.005	-0.008 ± 0.002	-0.019 ± 0.004	-0.019 ± 0.007	-0.01 ± 0.01
σ^2 (Å ²)		0.006 ± 0.001	0.003 ± 0.001	0.004 ± 0.001	0.004 ± 0.001	0.004 ± 0.001
Δr (Å)	2 nd	-0.063 ± 0.002	-0.019 ± 0.009	-0.025 ± 0.008	-0.02 ± 0.01	-0.05 ± 0.01
σ^2 (Å ²)		0.002 ± 0.001	0.010 ± 0.002	0.007 ± 0.001	0.012 ± 0.002	0.011 ± 0.002
$N_{1,2}$	1 st &	14.0 ± 0.1	14.0 ± 0.1	14.0 ± 0.5	13.9 ± 0.4	13.5 ± 0.4
$N_{Cu,Ni}$	2 nd	1 ± 1	1 ± 1	0 ± 3	1 ± 3	5 ± 3

5.4.3 EXAFS: Ni K-edge

The EXAFS spectra experimentally determined by the x-ray absorption experiments at the Ni K-edge are shown in Figure 5.13 A and their FT in Figure 5.13 B. The fit results are compiled in Table 5.9. These data were collected only at room temperature. Compared to the experiments at the Cu K-edge, those at the Ni K-edge are significantly facilitated by the higher Ni content of the RPV steel (i.e. 0.89 at.% Ni compared to only 0.08 at.% Cu), leading to higher count rates in the fluorescence detector and better counting statistics accordingly. Consequently the $N_{1,2}$ and $N_{Cu,Ni}$ uncertainty estimated by the evaluation software at Ni K-edge are smaller compared to those determined at the Cu K-edge (with the only exception of sample REF because $N_{1,2}$ and $N_{Cu,Ni}$ uncertainty is the same as REF measured at 15 K).



Figures 5.13 A and B: The EXAFS spectra $\chi(k)$ of the sample REF, HI1, HI3 and HI4 at the Ni K edge. $\chi(k) \cdot k^3$ is used to increase the contribution at large k (Fig 5.13 A). The FT of the EXAFS signal of REF, HI1, HI3, and HI4 at the Ni K edge is represented in Fig 5.13.B. Conditions: $W(k)$ is the Hanning function $4 \text{ \AA}^{-1} < k < 11 \text{ \AA}^{-1}$, $dk = 0.5 \text{ \AA}^{-1}$.

Table 5.9

Comparison of distance shift (Δr), the mean square relative displacement (σ^2), the number of atoms in the first and second shells (N) and numbers of Cu and Ni atoms in the two first shells at the Ni K-edge ($N_{Cu,Ni}$). The distance shift Δr is compared to the theoretical model (first shell distance: 2.482 ± 0.001 Å; second shell distance: 2.867 ± 0.001 Å).

Ni K-edge	Shell	REF (RT)	HI1	HI3	HI4
Δr (Å)	1 st	-0.025 ± 0.004	-0.029 ± 0.003	-0.026 ± 0.002	-0.004 ± 0.003
σ^2 (Å ²)		0.007 ± 0.001	0.005 ± 0.001	0.005 ± 0.001	0.005 ± 0.001
Δr (Å)	2 nd	-0.034 ± 0.003	-0.034 ± 0.004	-0.041 ± 0.006	-0.018 ± 0.004
σ^2 (Å ²)		0.004 ± 0.001	0.005 ± 0.001	0.006 ± 0.001	0.005 ± 0.001
$N_{I,2}$	1 st &	14.0 ± 0.1	13.9 ± 0.3	13.7 ± 0.4	13.6 ± 0.3
$N_{Cu,Ni}$	2 nd	1 ± 2	2 ± 2	1 ± 2	1 ± 2

6. Discussion

This chapter concerns the comparisons and discussion of results presented in Chapter 5 and those from literature presented in Chapter 2. Interpretations are also developed because of crucial importance for the understanding of the RPV behaviour. Basically this Chapter is composed of four parts: one about the binary alloy and the precipitate distribution; the second about the JRQ [71] samples and the confrontation between APT [94] and EXAFS [76] results, with a brief comment about re-irradiation and post annealing treatments; the third is about the difference between the results collected at the Ni and Cu K edge on KKG samples. The last section concerns the main questions that were posed at the beginning of this study and their answers.

6.1 Binary alloy

6.1.1 Comparison of precipitate size distribution

This section concerns the results obtained by XRD, TEM (see Fig 6.1) and EXAFS and a comparison with the results found in the literature. The apparent disagreement between the fractions of Cu in fcc phase in Tables 5.2 and 5.3 reflects the analytical difference between EXAFS and XRD concerning their resolutions. While EXAFS provide an average information around Cu absorbers (range of Å), XRD is more sensitive to large crystalline domains (range of nm).

It is important to point out another difference concerning EXAFS and XRD results: in sample B and C, bcc and fcc clusters have been detected by EXAFS. Since Cu and Fe atoms have a similar atomic number, it is not possible to distinguish their contribution if they are in a bcc matrix by XRD, because the Cu bcc signal would be superimposed in the Fe bcc peaks. Basically it means that Cu bcc clusters can be detected only by EXAFS and not by XRD.

In Figure 6.1 the normalized density of particles (clusters and precipitates) of sample D are plotted as a function of the diameter. The size distributions reported here are also compared with that found in the literature for similar samples and conditions determined by TEM [95].

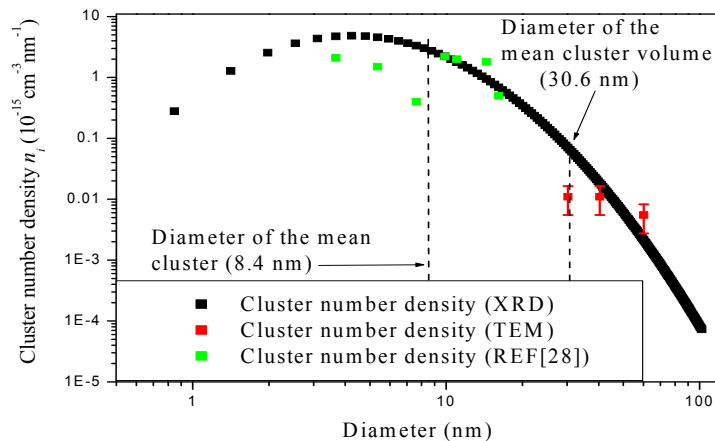


Figure 6.1: Comparison of the particle size distributions for sample D; XRD data are black, TEM data are red (Data extracted from Fig 5.3) and green data from literature [95].

These size distributions have two important implications:

1. the volume of the precipitates is proportional to the integrated XRD intensity, it is clear that most of the contribution of the fcc peaks (Fig 5.5) comes from the minority of large precipitates (while the majority of small precipitates do not emerge in the analytical signal).
2. if the fcc peak intensity could be calculated by using simply precipitates with a single size in sample D, the mean precipitate diameter (8.4 nm) would not yield reasonable intensities while the diameter of the mean cluster volume (30.6 nm) would be more satisfying.

Consequently for sample D, one third of the copper (see Table 5.3) forms a population of large precipitates; the other two third compose smaller precipitates not detectable by XRD. This result it is not obtained just by XRD, because, as said, XRD cannot investigate small clusters. Therefore the size distribution of Fig 6.1 is obtained by analytical XRD simulations based on the results, found by EXAFS, confirmed by TEM-EDS, that all Cu atoms reside in fcc phase.

The size distribution result, obtained from TEM and shown in Fig 6.1, is obtained by counting the precipitates in Fig 5.3 A and estimating their concentration for a sample thickness of ~ 20 nm (± 50 %). These indicative results are based on a rather small number of precipitates that make the statistical data imprecise. From TEM results only three classes have been considered in Fig 6.1. The particle size that can be derived from the EXAFS data may be deduced from the average number of Cu next neighbors in the 1st shells. This allows estimating the average number of Cu atoms in the particle and consequently its average size [37]. For precipitates larger than 1 nm the relative uncertainty rises quickly, i.e. clusters of 2000 atoms (diameter 3.6 nm) have the same number of atoms in the first shell as comparable Cu bulk material (within an uncertainty of 10 %). Sample D average cluster has ~ 28000 atoms (~ 5 nm).

Figure 6.1 also compares the size distribution from a former study (TEM data) [95]. The sample is a Fe 1.1 at% Cu after 10 h ageing at 820 K. These data are comparable with the data presented in this work.

6.2 RPV steel

6.2.1 JRQ samples (EXAFS and APT)

The Japanese Reference Quality (JRQ) samples [71] are characterized by XAFS and have been earlier analyzed by Miller *et al.* [94] using atom probe tomography (APT). APT provides information about the distribution of a specific element in the matrix and the atom density in the clusters through an atom imaging procedure. Although APT is sensitive to sub-nano-structures and is an element selective technique, it is not an equivalent to EXAFS and some results might be slightly different. For instance, Miller *et al.* used a ‘maximum separation method’ to define a cluster: atoms would belong to a cluster if their distance is within 6 Å. Additionally, a cluster should contain minimum 5 atoms in its neighbourhood. This allows identification of clusters even when they are much diluted in the matrix. It has also to be pointed out that APT is an element selective technique but it does not provide information about vacancies. In the present work [76], the EXAFS analysis was performed on the first and second neighbour shell (< 3 Å). For the reference sample, APT did not reveal any clusters [94]. The number of Cu and Ni atoms in the first and second shell $N_{\text{Cu,Ni}}$ determined by EXAFS is 1 ± 1 at the Cu K edge and 0 ± 1 at the Ni K edge. There is consequently an agreement between the two analyses within the experimental error.

For the irradiated sample (I), the APT study shows that the number density of clusters is $3 \times 10^{23} \text{ m}^{-3}$. Moreover these clusters are small and the amount of Cu in the matrix is reduced from 0.12 at% to 0.07 at% compared with the unirradiated sample. The average radius is larger than 1 nm. The most significant result gained by EXAFS is the reduction of the neighbour number N from 14 to 12.5 (Table 5.6). This means that some vacancies (or their clusters) must have formed around the absorbers. In the sample I (neutron fluence $5 \times 10^{19} \text{ cm}^{-2}$) EXAFS analysis reveals $N_{\text{Cu,Ni}} = 0 \pm 3$ for both Cu and Ni K-edge. Two reasons could explain the difference between APT and EXAFS results. Firstly, Miller *et al.* identified clusters if the distance between Cu or Ni atoms is equal or less than 6 Å. In this case, in EXAFS the absorber atoms which are not in the first 2 shells appear completely isolated and clusters would not be detected. Secondly, the low sensibility of the EXAFS analysis in this case ($N_{\text{Cu,Ni}} = 0 \pm 3$) suggests the possibility of small nano-clusters such as ‘dimes’ (two Cu atoms first neighbours surrounded by Fe atoms).

The sample IA was submitted to a prolonged annealing treatment (735 K, 168 h) after irradiation. A completely different environment was observed by APT with respect to the only irradiated condition: clusters are larger and their number density decreases from 3×10^{23} to $2 \times 10^{22} \text{ m}^{-3}$ (see Table 5.6). The neighbour number N revealed by EXAFS is 13.3 ± 0.4 and 13.3 ± 0.3 and $N_{\text{Cu,Ni}}$ 9 ± 2 and 7 ± 3 , respectively, at Cu and Ni K-edges. This change in the environment after the annealing treatment is connected to the high density of vacancies after the first irradiation. As described by Radiguet *et al.* [20], the vacancies allow Cu (or Ni) atoms to migrate easily and to form clusters. By APT it was

found that Cu atom density decreases in the matrix (from 0.58×10^{26} to $0.5 \times 10^{26} \text{ m}^{-3}$) and the average radius of clusters increases to 1.5 nm [94].

The sample IAR shows the occurrence of clusters ($1.3 \times 10^{23} \text{ m}^{-3}$) and of diluted Cu atoms in the matrix ($0.75 \times 10^{26} \text{ m}^{-3}$) as expected [94]. The average cluster radius is 0.9 ± 0.4 nm, almost the same size found for the sample I by APT. With respect to EXAFS, the sample IAR and IARA do not show a big difference to IA. Even though there is a small increase of $N_{\text{Cu,Ni}}$ during the last annealing step (IAR \rightarrow IARA) in the case of the Cu K-edge and a small decrease in the case of the Ni K-edge, these samples have practically the same coordination number N and both have a high $N_{\text{Cu,Ni}}$ value. For the sample IARA, Miller *et al.* found a decrease of the number of density of clusters. It was finally revealed an increase of the average radius and of the density of the atoms in the clusters

6.2.2 RPV cluster size evaluation

The evaluation of the mean cluster size by EXAFS is a serious issue because of the limitation of the technique for nanostructures larger than 1 nm. This issue has been deeply investigated [37, 68, 69] and even during this thesis (see [35]). Even if it is not possible to provide with high accuracy the number of atoms in a cluster, some studies provide semi-empirical [37] and theoretical formula [36]. These formulas correlate the number of atoms in the first and second shell (found experimentally) with the total number of atoms in a cluster. All the studies presented in this section are based on clusters in vacuum. Especially the results found in [36] can be applied to bcc clusters. In this case two bcc clusters are investigated: with a cubic and with an octahedron shape. Since the clusters in RPV are expected to be sphere like, the number of atoms in the cluster is calculated as composed of 50% of cubic and 50% of octahedron clusters. The number of Cu (and Ni) atoms $N_{\text{Cu,Ni}}$ in the first and second shell used to calculate the average cluster size is taken from the sample IAR (7 ± 1 at the Ni K edge). The model presented in [36] considers only the $N_{\text{Cu,Ni}}$ for the first shell but not for the second. Since by EXAFS it is not possible to distinguish the contribution of the first and second shell in bcc cluster, the model can be applied only normalizing $N_{\text{Cu,Ni}}$ with the number of total atoms in the first two shells experimentally determined (13.3 ± 0.3). With simple calculation it is possible to determine the number of atoms per cluster. The average number of atoms involved in the clusters is 15, with an average diameter of ~ 0.6 nm. This result has to be considered as the average cluster size in case of bcc clusters in vacuum. Moreover, the model presented in [36] considers only monoatomic clusters while in RPV samples the Fe contribution in the cluster is relevant (see Chapter 2 and [21]). It is worth to remind that $N_{\text{Cu,Ni}}$ considers the number of atoms of Cu and Ni in the first two shells: a high value of $N_{\text{Cu,Ni}}$ points out the high concentration of solutes atoms near the absorbers. Nevertheless this concentration might occur in two cases: with a very small pure cluster or with a larger cluster but not pure. In the first case there would be a high ratio between the number of atoms on the surface and on the core. The atoms in the core would be completely surrounded by solute atoms while the atoms on the surface (the majority for small clusters) would be mostly by Fe atoms. In this case $N_{\text{Cu,Ni}}$ would be strongly influenced by the surface atoms. These are the clusters investigated by [36]. In the second case larger clusters occur: the number of atoms in cluster core is the majority, but they are not completely surrounded by solute atoms, the large amount of Fe atoms in

the core of the cluster contributes to the $N_{\text{Cu,Ni}}$ limitation. The surface atoms, since they are the minority, have a weaker influences on $N_{\text{Cu,Ni}}$. This second case is found in all RPV samples [76]. So it is clear that the cluster size found by [36] is expected to be underestimated compared to what was found by APT shown in Table 6.1. The incertitude of the cluster size diameter is calculated from the relative incertitude of $N_{\text{Cu,Ni}}$ and N and does not consider the underestimation explained above.

Table 6.1

Comparison of EXAFS data at Cu and Ni K-edges and APT data [94]. Cu atom density is equal to $1 \times 10^{26} \text{ m}^{-3}$ for (Fe 0.12at%Cu). Miller *et al.* did not found clusters in the reference sample; $< 10^{19} \text{ m}^{-3}$ refers to the minimum detectable density. $\rho^{Cluster}$ is the density of clusters (m^{-3}), $\rho_{\text{Cu}}^{Matrix}$ is the density of Cu atoms in the matrix $\pm 10 \%$ (m^{-3}), d_{av} is the average cluster radius (nm), $\rho_{\text{Cu}}^{Cluster}$ is the density of Cu atoms in clusters (m^{-3}).

Analysis		REF	I	IA	IAR	IARA
APT	$\rho^{Cluster} \text{ (m}^{-3}\text{)}$	$< 10^{19}$	3×10^{23}	2×10^{22}	1.3×10^{23}	1×10^{22}
	$\rho_{\text{Cu}}^{Matrix} \text{ (m}^{-3}\text{)}$	1×10^{26}	0.58×10^{26}	0.50×10^{26}	0.75×10^{26}	-
	Cluster diameter d (nm)	$< 1.2^*$	2.2 ± 0.2	3.0 ± 0.2	1.8 ± 0.8	3.2
	$\rho_{\text{Cu}}^{Cluster} \text{ (m}^{-3}\text{)}$	$< 10^{19}$	0.42×10^{26}	0.50×10^{26}	0.25×10^{26}	-
EXAFS Cu K edge	N 1 st & 2 nd shells	14.0 ± 0.1	12.5 ± 0.4	13.3 ± 0.4	13.3 ± 0.5	13.3 ± 0.4
	$N_{\text{Cu,Ni}}$ 1 st & 2 nd shells	1 ± 1	0 ± 3	9 ± 2	7 ± 4	8 ± 3
EXAFS Ni K edge	N 1 st & 2 nd shells	14.0 ± 0.1	12.5 ± 0.4	13.3 ± 0.3	13.3 ± 0.3	13.3 ± 0.1
	$N_{\text{Cu,Ni}}$ 1 st & 2 nd shells	0 ± 1	0 ± 3	7 ± 3	7 ± 1	6 ± 1
Cluster diameter d_{av} (nm)		0	0	0.6 ± 0.3	0.6 ± 0.1	0.5 ± 0.1

*in [94] the measure of the radius was < 0.6 nm which is actually below the detection limit. The diameter indicated here so has to be considered either below the detection limit.

6.2.3 Post annealing treatment

Aging of reactor pressure vessel steel is a well-known effect. The safe operation of RPVs is controlled by the use of surveillance samples coming from the nuclear power plants. However, some important scientific questions, concerning formation and morphology of the irradiation induced clusters and/or precipitates, are still open. These questions play a role with respect to extended reactor operation (late in life precipitation of Ni- or Mn-atoms together with Cu-clusters) and the success of possible additional heat treatment as healing measure. Another research topic is the material behaviour concerning post-irradiation heat treatment as healing measure and subsequent re-irradiation after such an annealing [11, 96]. It is questionable whether annealing increases, decreases or does not change the re-embrittlement tendency. Several structural analysis techniques are used to obtain a reliable prediction of re-irradiation behaviour.

In another study on JRQ [71] samples [94] the effects of the annealing, post-annealing treatment, irradiation and post irradiation where investigated through the variation of the mechanical properties and APT; it was observed that the deterioration of the mechanical properties is not only reduced by annealing but re-embrittlement is slowed down as well. The mechanical tests showed that the re-annealing (annealing treatment performed after having irradiated the sample in the reactor) is useful to decrease the shift in the ductile-brittle temperature, but the presence of clusters does not seem to be affected by it and actually the clusters seem to increase in size and density of impurities (Cu, Ni, Mn...).

It has been shown that unirradiated steel submitted by large neutron fluence ($5.0 \times 10^{23} \text{ cm}^{-2}$) is affected by a significant shift of the ductile to brittle temperature (96°C). An irradiated steel, recovered with an annealing treatment after the first irradiation and then re-irradiated a second time with neutron fluence almost 6 times smaller ($0.85 \times 10^{23} \text{ cm}^{-2}$ sample IAR), obtains a rather high shift of the ductile to brittle temperature (56°C) [94]. Basically the embrittlement looks much faster in the case of re-irradiation. This behavior might be expected because an annealing treatment at 735 K is necessary to prevent large matrix damage (large amount of interstitial atoms and vacancies which recombine faster at high temperature) but it does not prevent clusters formation.

6.2.4 KKG samples: effect of irradiation at 575 K

Four RPV surveillance samples have been analyzed in detail by EXAFS investigations, three irradiated in the reactor and one unirradiated as reference. Considering the total number of atoms in the first and second shell N , it is important to note that at the Cu K-edge N does not change significantly for the samples HI1 and HI3 (14.0 ± 0.5 and 13.9 ± 0.4 respectively) with respect to REF (14.0 ± 0.1). A significant difference was found for the sample HI4 (13.5 ± 0.4). Similar results have been obtained at the Ni K-edge with 13.9 ± 0.3 and 13.7 ± 0.4 atoms in the first and second shell around the absorber for HI1 and HI3, whereas HI4 has 13.6 ± 0.3 atoms. The decrease of the number of atoms in the first and second shell around the absorber is due to the neutron irradiation: the production of point defects is faster than the recombination of vacancies and interstitials even at the elevated irradiation temperature of 575 K. Within the accuracy of the experiments, the gained results suggest that the vacancies are similarly distributed around both the absorbers Cu and Ni as can be more clearly seen in Fig 6.2. Such a result is expected because the original bcc-lattice structure of the steel is maintained after the irradiation, and both Cu- and Ni-atoms are supposed to be mainly located on regular bcc-lattice sites. Thus, the average number of point defects created in the vicinity of each atom should be similar and only depending on the applied irradiation fluence.

Considering the number of Cu and Ni atoms $N_{\text{Cu,Ni}}$ around the copper and nickel absorbers (Figure 6.3), the gained results suggest that both species do not behave in the same way. Although affected by a large error, it was found that Cu and Ni are enriched in the vicinity of the Cu atoms, while the composition of the first and second shell around Ni seems to be independent from the applied neutron irradiation. On a first glance, these findings seem to be contradicting. However, it is important here to remember that Cu and Ni atoms are not distinguishable when they both belong to the environment; their backscattering amplitudes are very similar. Assuming that copper and nickel are randomly distributed in the first and second coordination shells of both copper and nickel, the EXAFS analysis should show the similar behaviour, e.g. a decrease or an increase of $N_{\text{Cu,Ni}}$ for both edges investigated. Therefore, these observations have to be interpreted in terms of an accumulation of Cu in the atomic environment of Cu-atoms, i.e. a formation of small Cu-clusters despite its lower concentration in the RPV-steel. Thus, most of the $N_{\text{Cu,Ni}}$ around Cu seems to be Cu, while the opposite is true for Ni, i.e. the local environment of Ni is mainly formed by Ni and not by Cu. This is consistent with the more or less constant value of $N_{\text{Cu,Ni}}$ determined from the experiments at the Ni K-edge. This is a quite surprising result since the concentration of Ni in the RPV-steel matrix is about 11 times higher compared to Cu. The Cu atoms seem to exhibit an extremely high

mobility in the steel lattice, and in parallel, they seem to pin each other, leading to nano-sized precipitates even during the early stages of neutron irradiation. This underlines the prominent role of copper observed in the embrittlement of RPV steels [17, 20].

Table 6.2

Comparison of the distance shift (Δr), the mean square relative displacement (σ^2), number of atoms in the first and second shell (N) and number of Cu and Ni atoms in the two first shells at the Cu K-edge ($N_{Cu,Ni}$) as determined by a fit of the measured EXAFS. The distance shift Δr is compared to the theoretical model (first shell distance: 2.482 ± 0.001 Å; second shell distance: 2.867 ± 0.001 Å for bcc Fe).

Cu K-edge	shell	REF (15K)	REF (RT)	HI1	HI3	HI4
Δr (Å)	1 st	-0.030 ± 0.005	-0.008 ± 0.002	-0.019 ± 0.004	-0.019 ± 0.007	-0.01 ± 0.01
σ^2 (Å ²)		0.006 ± 0.001	0.003 ± 0.001	0.004 ± 0.001	0.004 ± 0.001	0.004 ± 0.001
Δr (Å)	2 nd	-0.063 ± 0.002	-0.019 ± 0.009	-0.025 ± 0.008	-0.02 ± 0.01	-0.05 ± 0.01
σ^2 (Å ²)		0.002 ± 0.001	0.010 ± 0.002	0.007 ± 0.001	0.012 ± 0.002	0.011 ± 0.002
N	1 st & 2 nd	14.0 ± 0.1	14.0 ± 0.1	14.0 ± 0.5	13.9 ± 0.4	13.5 ± 0.4
$N_{Cu,Ni}$		1 ± 1	1 ± 1	0 ± 3	1 ± 3	5 ± 3
d_{av} (nm)		0	0	0	0	$\sim 0.4 \pm 0.3$

In Tab 6.2 is shown also an estimation of the diameter of the mean cluster in case of pure and mono-dispersive distribution. The estimation is calculated by [9] and as it has to be considered a rough estimation.

Table 6.3

Comparison of distance shift (Δr), the mean square relative displacement (σ^2), the number of atoms in the first and second shells (N) and numbers of Cu and Ni atoms in the two first shells at the Ni K-edge ($N_{Cu,Ni}$). The distance shift Δr is compared to the theoretical model (first shell distance: 2.482 ± 0.001 Å; second shell distance: 2.867 ± 0.001 Å).

Ni K-edge	Shell	REF (RT)	HI1	HI3	HI4
Δr (Å)	1 st	-0.025 ± 0.004	-0.029 ± 0.003	-0.026 ± 0.002	-0.004 ± 0.003
σ^2 (Å ²)		0.007 ± 0.001	0.005 ± 0.001	0.005 ± 0.001	0.005 ± 0.001
Δr (Å)	2 nd	-0.034 ± 0.003	-0.034 ± 0.004	-0.041 ± 0.006	-0.018 ± 0.004
σ^2 (Å ²)		0.004 ± 0.001	0.005 ± 0.001	0.006 ± 0.001	0.005 ± 0.001
N	1 st & 2 nd	14.0 ± 0.1	13.9 ± 0.3	13.7 ± 0.4	13.6 ± 0.3
$N_{Cu,Ni}$		1 ± 2	2 ± 2	1 ± 2	1 ± 2

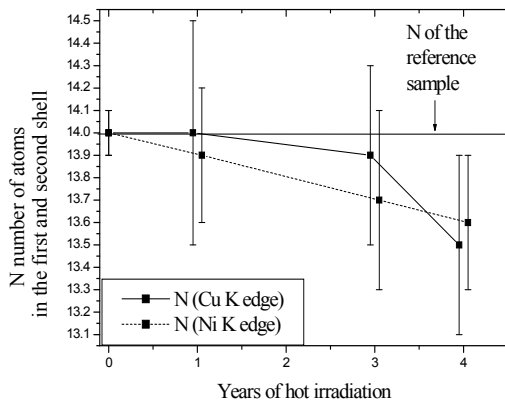


Figure 6.2: Number of atoms in the first and second shell of the absorbers at the Cu and Ni K edge. Note that the years of irradiation are slightly shifted to avoid annoying overlap

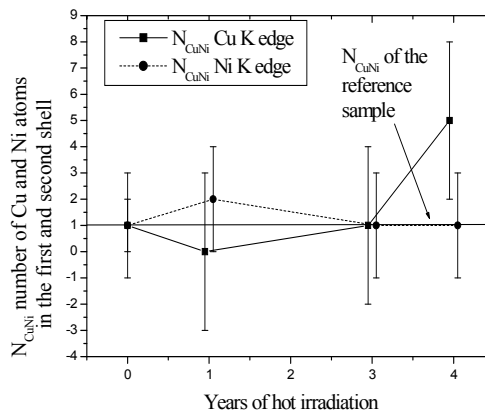


Figure 6.3: Number of the atoms of Cu and Ni in the first and second shell around the absorber at the Cu and Ni K edge. Note that the years of irradiation are slightly shifted to avoid annoying overlap

Since the cluster size of RPV material cannot be evaluated by EXAFS with high accuracy (see 6.2.2) because of the coexistence of many elements diluted in clusters, which are not considered by the theoretical model [36], another method is needed. The mean cluster size of sample HI4 can be evaluated considering the cluster sizes of JRQ [71] samples (see Table 6.1): in the samples IA, IAR and IARA, $N_{Cu,Ni}$ is equal to 9 ± 2 , 7 ± 4 and 8 ± 3 respectively. These sizes correspond roughly to sphere-like clusters within a radius of 1.6 nm (diameter of 3.2 nm) as seen by APT. Consequently, the clusters of samples HI4, which show 5 ± 3 Cu (and Ni) atoms in the first and second shell, are expected to be slightly smaller. This behaviour is fully understandable because the sample KKG is not submitted to any post annealing treatment at high temperature. In Figure 6.4 a qualitative representation of the cluster sizes of all samples is shown. The diameter and the number of atoms represented are calculated according to the density of Cu and the crystalline structure of Cu. According to the heat treatment, the concentration of solute clusters changes phase in different moment [97]: this is the reason behind the different behaviour found for the binary alloy FeCu and JRQ [71] and KKG sample. Moreover it is already pointed out that RPV clusters do not form pure clusters but they are a mix of solute atoms (Cu and Ni) and iron even after a long annealing treatment. For this reason they do not switch to fcc structure. The binary alloy presented in this work has a high concentration of solute atoms: bcc clusters can become pure (free of Fe) faster than RPV and crystallize in fcc as well.

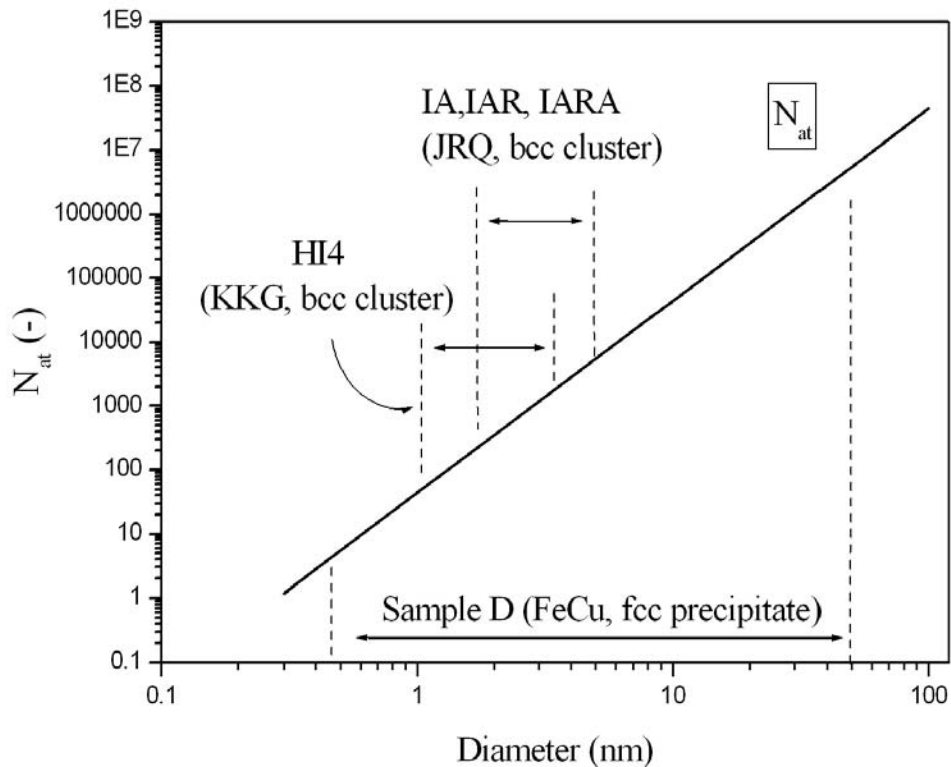


Figure 6.4: A qualitative representation of the distribution of the cluster sizes in the KKG (HI4), JRQ (IA, IAR, IARA), FeCu (sample D) samples. For JRQ samples the cluster diameter limits are estimation mainly based on the APT results shown in Table 6.1. For sample HI4 the cluster diameter limits are estimation (see text). For the sample D the limits are taken from Figure 6.1.

6.3 Key questions

A few questions were posed when the project started. Their answer has been given during in the previous chapters and here a short overview is provided.

6.3.1 Do very small aggregates already exist in the as received, solution annealed alloys as indicated by preliminary EXAFS tests and which are not detectable with small angle neutron scattering, transmission electron microscopy, positron annihilation spectroscopy or atom probe?

Small cluster does not occur in the as ‘received samples’. In case of JRQ samples [71], this is shown in Table 5.6, 5.7 and 6.1. For KKG sample this is shown in Table 5.8. In case of JRQ samples it was confirmed even by Miller *et al* [94]

6.3.2 How do the precipitates form (solid solution \Rightarrow small clusters \Rightarrow precipitates)?

As shown in the Chapter 5 and in Section 6.3.1 in the as 'received samples' solute atoms are in a homogeneous solid solution with the same crystallographic phase as the bulk material. Many factors help the clusters formations:

1. solute concentration (Cu, Ni, Mn...);
2. high temperature and long annealing treatment;
3. neutron irradiation.

All these three points have been already considered in Chapter 2, 3 and 5 and here they are summarized.

Solute concentration is probably the most important characteristic of steel because it can easily modify the rate of the cluster formation, the size of the clusters as well as their phase. The samples investigated in this thesis present a low amount of solute Cu: ~ 0.1 at % for the RPV steel and 1.34 at % for the inactive alloy (see Chapter 4 for more details).

As seen, only during an annealing treatment clusters grow. Long annealing treatments and high temperatures have been investigated in Section 5.1 for the binary alloys. It was shown that copper atoms in the first stage form bcc clusters and, whether enough large, may switch phase. In the last stage of clustering, all the clusters are in the fcc phase. The clusters size distribution is represented in Fig 6.1 and it important to point out that small clusters (~ 1 nm) can already switch from bcc to fcc. Fortunately in RPV steel, the concentration of Cu atoms is too small and clusters do not succeed in changing phase.

In case of RPV steels the neutron irradiation plays a fundamental role. Neutron irradiation causes atoms cascades and they contribute to re-arrange the position of atoms with the formation of interstitial atoms and vacancies. Studies based on PAS introduced in Chapter 2, shows the strong 'bounds' between Cu atoms and vacancies. Basically at low concentration of Cu (0.1 at % or less) the formation of clusters significantly is helped by the irradiation: irradiation can produce clusters of vacancies which are very suitable for the Cu atoms [20].

6.3.3 How do other atoms, e.g. Ni, Mn, influence the formation of the Cu precipitates?

Cu and Ni K edge were analyzed in detail and a rich literature deals with this topic. Concerning literature Maury *et al.* [18] show by EXAFS that in ternary alloys Fe,Cu,Mn (Fe 1.26 at % Cu and 1.37 at % Mn) Mn atoms have an active role in Cu clustering even if they are not completely involved in the process. The study was performed at Cu and Mn K edges. While the XANES spectra, as well as the EXAFS FT, at the Cu K edge show a change more pronounced with the increasing of the annealing time, at the Mn K edge this change is not observed in the XANES and neither in the EXAFS FT. A slight change of the amplitude of the first peak of the EXAFS FT was not considered significant even if it might have interpreted as a presence of a increasing of the disorder in a system (because of the coexistence of two different phase bcc and fcc). The reason of it resides in the non-perfect quality of their data and because probably their software was not so developed. Anyway the most important results are obtained comparing FeCu (Fe 1.34 at % Cu) and the FeCuMn alloy: both samples show, at the Cu K edge, the presence of the fcc Cu clusters.

The concentration of Cu atoms in fcc clusters is larger if Mn is present although at the Mn K edges no fcc clusters were found. Basically a fraction of Mn atoms contributes to the copper clusters formation, but the involved amount of Mn atoms involved is small enough that their contribution is covered by most of the Mn atoms which are still diluted in the Fe matrix. This explication finds a confirmation in [21] (see also Section 2.2.5) where a composition profile of a cluster in RPV steel is given by APT. Mn atoms show to be present (~ 12 %) in the border of the Cu cluster (see Figure 2.2), but if EXAFS was performed at the Mn K edge, the contribution of Mn atoms would be easily covered behind the contribution of the Mn atoms diluted in the matrix, which are the majority.

The Ni contribution in the formation of Cu clusters was investigated and the results are shown in Chapter 5 and 6. Briefly, Ni atoms form clusters and help Cu atoms to form clusters in the case of a post-annealing treatment (168h, 735K) on a sample previously strongly irradiated (Sample IA). This behaviour occurs because many defects are produced by the first irradiation (see N 1st & 2nd shells in Table 6.1 for samples REF, I and IA) which are partially recovered by cluster formations. The presence of a large number of defects is very important in order to form clusters as seen, in Section 2.2.5 and [20]. As it has been shown in Section 5.4 Cu and Ni do not behave in same way if the samples are irradiated in the reactor. This is shown and explained in detail in section 6.3. Basically Ni atoms need point defects to form clusters. The irradiation provided by Gösgen Nuclear Power Plant is not able to produce such the level of point defects that Ni needs.

6.3.4 How do the precipitates behave on post-irradiation thermal annealing and re-irradiation?

The post-irradiation annealing treatment (735 K for 168 h) shown in this thesis pointed out that a thermal treatment is mandatory to reduce the matrix damage but it does not have any influence in dissolving clusters. The results are shown in 5.2 and are explained briefly in 6.2.2. The main point concerns the presence of the clusters: if they cannot get dissolved at ordinary post irradiation annealing treatment (735 K), then they promote a quicker increase of the DBT temperature. As shown in Section 2.2.6 by Nagai *et al.* [24] affirm that the widely accepted conditions for the post annealing treatment [26] (735 K for 168 h) are not enough. One of the most important results of Nagai *et al* concerns the temperature of the post annealing treatment: microvoids (cluster of vacancies) disappear with an annealing treatment at 675 K. Copper precipitates recovery depends on the copper concentration: for the sample Fe 0.045 at % Cu it is at 875 K for the Fe 0.27 at % it is at 925 K. These recovery temperatures of the precipitates are consistent with the solubility limit of Cu in Fe [27].

This result is consistent with what found by Miller *et al.* [94]: the re-embrittlement is much faster if the sample is re-irradiated, because clusters do not disappear for a long annealing treatment at 735 K.

The post-irradiation annealing treatment (sample IARA) does not seem to affect strongly the structure of clusters: by EXAFS no particular changes are detected, the clusters look as large as are those in sample IAR even if by APT a slightly increase of the size was detected [94].

6.3.5 What is the limiting size and concentration of aggregates-precipitates markedly affecting the mechanical proprieties?

Two of the most important mechanical properties for RPV steels are the DBT temperature and the Fracture Toughness. It is well known that during the operation time there is an increase of the DBT temperature and a decrease of the Fracture Toughness. These mechanical properties are affected by a combination of nano-phenomena: cluster formation and matrix damage.

It is very difficult to evaluate the DBT temperature, for instance, caused from the two nano-phenomena separately. As seen in 6.3.4 these two phenomena have different recover temperature. It is generally easier to recover the matrix damage than the precipitate damage which needs higher temperature. Moreover to split the contribution of the nano-phenomena, the main approach is semi-empirical and it was already discussed in the Chapter 2. A semi-empirical approach hides two main problems:

1. it is based on an attempt to find an equation that can be applied to a reduced amount of experimental data. Basically it means that a model of good quality gives satisfactory results only if applied to the small group of samples where was tested;
2. a semi-empirical method is not based on a solid theory. For example in one of the examples shown in the Chapter 2 [11], some developed equations are based on a few parameters which do not have a physical meaning.

7 Conclusion

This project deals with the study of the reactor pressure vessel (RPV) steel used in nuclear power plants as main component of the nuclear reactor. The RPV steel is exposed to neutron fluence and to prolonged high temperature treatments due to operation time of the reactor. The focus of this study is mainly on the understanding of the degeneration of the mechanical properties of the RPV steel which can significantly modify the lifetime of the reactor. The degeneration of the steel can be investigated macroscopically by Charpy test to verify the variation of the toughness of the steel or by the variation of the Seebach coefficient. A decrease of the toughness is correlated to the increase of the ductile to brittle transition temperature (ΔT_{DBT}), which provides a strong limitation of the power plant lifetime. The re-annealing treatment of the steel at high temperature (735 K) is the common procedure to reduce the ΔT_{DBT} , prolonging the lifetime of the reactor. The degeneration of the RPV steel is caused by two strictly-connected phenomena: matrix damage mainly caused by the neutron irradiation and the clusters formations. As requested at the beginning of the project, it was verified that the unirradiated RPV reference does not show any clusters. Moreover it has been shown that Cu is the most involved element in the clusters formation despite its low concentration ($< 0.1\%$). The clusters formation does not involve only Cu, also Mn and Ni atoms have to be considered. Cu clusters become larger if Mn is diluted in the matrix, while Ni atoms, under special conditions, form clusters similarly to Cu's behavior. In agreement with studies, presented in section 2.2.6, it was verified that a re-annealing treatment at 735 K, although useful to decrease the ΔT_{DBT} temperature by the recovering of the matrix damage, does not limit the clusters growth: cluster dissolution needs much higher temperature.

The cluster formation in steels is one of the main topics of the thesis. Usually clusters are composed mainly of copper and they have the same crystallographic structure as the iron matrix (bcc). Under special conditions, above all connected to the Cu concentration and to the temperature treatments, these clusters can change phase (from bcc to fcc). In the first part of the thesis, inactive binary alloy samples are investigated with particular regard to the phase change. The second concerns the analysis of reference and real reactor pressure vessel steels provided by the International Atomic Energy Agency (IAEA) and by a power plant respectively and it underlines matrix damage, clusters formation and the particular role of Ni atoms.

In case of inactive samples, x-ray absorption fine structure (XAFS) spectroscopy, x ray diffraction (XRD), transmission electron microscopy (TEM) and energy dispersive x ray spectrometry (EDS) have been successfully performed on a FeCu binary alloy (1.3 at % Cu) to gain information about the local structure of the Cu clusters and to understand the Cu cluster formation. Even with very low amount of Cu, these clusters ($> \sim 1$ nm) are found to switch easily from bcc to fcc Cu structure if the number of copper atoms in the clusters are sufficiently high concentrated. Annealing for long time and at high temperature is found to affect the clustering. Four samples named A, B, C and D annealed at 775 K for 2.5, 8, 115 and 312 hours, respectively, are analyzed by XAFS spectroscopy at the Cu-K edge and by XRD. These four samples show the development of 4 different stages of fcc clusters diluted in a bcc matrix. Sample A, annealed for 2.5

hours at 775 K, shows a good dilution of Cu atoms in the Fe matrix, while sample D, annealed for 312 h at 775 K, has large fcc Cu clusters.

By linear combination of the structure of the normalized x ray near edge spectra (XANES), it is possible to estimate that sample B, annealed for 8 hours at 775 K, has clusters coherent with the matrix and a small percentage of clusters in fcc phase. Sample C, annealed for 115 hours at 775 K, shows the coexistence of coherent and incoherent (bcc and fcc) clusters with an increase of the fcc phase. Since the linear combination of XANES of samples B and C, annealed for 8 and 115 h, are based on samples A and D, annealed 2.5 and 312 h respectively, the investigation of sample D became a priority of this work. Transmission electron microscopy and energy dispersive x ray spectrometry allow obtaining information about the phases in this sample and reveal occurrence of clusters with a size of up to 60 nm. These clusters are verified to be composed of pure Cu, while the matrix, that surround them, of pure Fe. In order to complete the view on the size distribution, XRD is performed, revealing a broad cluster size distribution: one third of Cu atoms form large clusters (~ 30 nm), two third of the Cu atoms are included in too small clusters to affect the XRD peaks shape. The average cluster size was calculated to be ~ 8.4 nm.

The study of active steel on IAEA samples involves investigation of the matrix damage and of the clusters formation. Five samples one inactive and four active samples are analyzed. Their composition (see Chapter 4) is similar to the usual composition of the RPV steels. The irradiation was performed to high doses in order to reproduce the conditions of the RPV steel after many years of operation. The four irradiated samples are submitted to different neutron irradiation and annealing treatment: the sample I is irradiated, IA is irradiated as I and annealed in order to reproduce the conditions of post-irradiation treatments. The samples IAR is irradiated, annealed and re-irradiated and the sample IARA is submitted to the same treatment as IAR and then re-annealed a second time in order to reproduce the treatment as done in a nuclear power plant to recover the matrix damage.

The characterization of the matrix damage of a reactor pressure vessel (RPV) IAEA reference steel samples has been performed through EXAFS spectroscopy studies. EXAFS spectra, collected at the K-edge of Cu, Ni and Mn, show that these atoms reside in a closed-packed arrangement similar to that of bcc Fe. A quantitative analysis, based on an environment of pure Fe, has been done by analyzing the Fourier-transformed EXAFS data, and adopting a best-fit simulation procedure in order to determine the near neighbor atomic environment around these absorber atoms. The main difference in the local structural parameters due to irradiations is a systematic change in the coordination numbers in nearest-neighbour atomic shells, and an increase in the Debye Waller (DW) factor upon irradiation and post-irradiation annealing. Such changes in the coordination numbers are however not apparent in the EXAFS data measured at the Fe K-edge; here only a slight increase in the DW factor is observed from the data analysis. The results are attributed to the involvement of point defects and their equilibrium population in the vicinity of these absorber elements. These results trigger further experimental work as well as theoretical model calculations for the atomic-scale description of lattice damage to clarify their possible influence on technological applications of neutron irradiation into RPV material.

The same IAEA reference steel samples (JRQ [71]) have been analyzed by XAFS in order to investigate Cu (or Ni) clusters providing quantitative data within the first and the second neighbour shells. In comparison to the previous study, in this work an environment composed of Cu (Ni) and Fe is used instead that an environment of pure Fe. Both Cu and Ni atoms reside in a bcc environment as in the case of the Fe matrix. Neutron irradiation and annealing treatments do not induce any structural phase change under the given conditions. The neutron irradiation leads to a reduction of the number of next neighbours. The combination of neutron irradiation and annealing treatment is important: the changes in the first and second shell environment around the absorber are much larger in the IA (irradiated and annealed), IAR (irradiated, annealed and re-irradiated) and IARA (irradiated, annealed, re-irradiated and re-annealed) samples than in those recorded for the only irradiated sample. The EXAFS analysis have demonstrated the increase of the number $N_{\text{Cu,Ni}}$ of Cu and Ni atoms around the absorber. With respect to the precipitates, the results are in agreement within experimental error with previous studies using atom probe tomography.

Finally, three RPV surveillance samples, irradiated in the nuclear power plant of Gösgen (Switzerland) for 1, 3 and 4 years, as well as unirradiated reference material have been analyzed by EXAFS at the Cu and Ni K-edges. Both Cu and Ni atoms reside in a bcc environment, similar to the Fe matrix. Neutron irradiation in the reactor at 575 K did not induce any major lattice type change under the given conditions. However, neutron irradiation in reactor leads to small changes of the local atomic environment around the investigated Cu and Ni atoms, since a slight reduction of the number of next neighbours in the bcc-structure around Cu and Ni in the steel matrix was observed. This reduction is likely to be proportional to the number of years of irradiation in reactor, and thus, most of the local structural changes are obtained for the sample with the longest irradiation time. It can be expected that the elevated temperature of the reactor partially helps the refilling of the irradiation induced vacancies by a kind of annealing processes. The detailed EXAFS analysis has demonstrated that the number of Cu atoms in the local vicinity of copper is enriched during irradiation at elevated temperature, while the local atomic environment around nickel seems to be more or less unaffected.

The results shown here and a detailed literature research provide a complete answer to the questions presented in Section 6.3. Since XAFS spectroscopy had never been applied to RPV steels, this work is particularly valid because it shows clearly the difference and similarities with other techniques. Moreover the RPV steel from a Swiss power plant was analyzed in detail.

Reference

1. Odette, G.R., Lucas, G.E., J. Mater., 2001. **53**: p. 18.
2. Miller, M.K., Russell, K.F., Sokolov, M.A., Nanstad, R.K., J. Nucl. Mater., 2003. **320**: p. 177.
3. Niffenegger, M., Reichlin, K., Kalkhof, D., Nucl. Eng. Des., 2005. **235**: p. 1777.
4. Wirth, B.D., Glade, S.C., Odette, G.R., Asoka, P., Sterne, P.A., proceeding of: 22nd American Society for Testing and Materials, Symposium on Effects of Radiation on Materials, Boston, 2004.
5. Fujii, K., Fukuya, K., Nakata, N., Hono, K., Nagai, Y., Hasegawa, M., J. Nucl. Mater., 2005. **340**: p. 247.
6. Koík, J., Keilová, E., Lek, J., Procházka, I., J. Nucl. Mater., 2002. **303**: p. 52.
7. Miller, M.K., Wirth, B.D., Odette, G.R., Mater. Sc. Eng., 2003. **A353**: p. 133.
8. Fukuya, K., Ohno, K., Nakata, H., Dumbill, S., Hyde, J. M., J. Nucl. Mater., 2003. **312**: p. 163.
9. Carter, R.G., Soneda, N., Dohi, K., Hyde, J. M., English, C. A., Server, W. L., J. Nucl. Mater., 2001. **298**: p. 211.
10. Debarberis, L., Sevini, F., Acosta, B., Kryukov, A., Nikolaev, Y., Amaev, A.D., Valo, M., Int. J. Pres. Ves. Pip. 2002. **79**: p. 637.
11. Debarberis, L., Acosta, B., Sevini, F., Kryukov, A., Gillemot, F., Valo, M., Nikolaev, A., Brumovsky, M., J. Nucl. Mater., 2005. **336**: p. 210.
12. Miloudi, S., PhD Thesis, Université d'Orsay, 1997.
13. Byun, T.S., Farrell, K., J. Nucl. Mater., 2004. **326**: p. 86.
14. Grosse, M., Böhmert, J., Viehrig, H.W., J. Nucl. Mater., 1994. **326**: p. 177.
15. Böhmert, J., Viehrig, H.-W., Ulbricht, A., J. Nucl. Mater., 2004. **334**: p. 71.

16. Debarberis, L., Acosta, B., Sevini, F., Chernobaeva, A., Kryukov, A.M., J. Nucl. Mater, 2006. **350**: p. 89.
17. Kuri, G., Degueldre, C., Bertsch, J., Rothe, J., J. Nucl. Mater 2007. **362**: p. 274.
18. Maury, F., Lorenzelli, N., Mathon, M.H., de Novion, C.H., Lagarde, P., J. Phys.: Condens. Mater., 1994. **6**: p. 569.
19. Stern, E.A., Newville, M., Ravel, B., Yacoby, Y., Haskel, D., Physica B 1995. **117**: p. 208.
20. Radiguet, B., Barbu, A., Pareige, P., J. Nucl. Mater., 2007. **360**: p. 104.
21. Pareige, P., Stoller, R.E., Russell, K.F., Miller, M.K., J. Nucl. Mater. , 1997. **249**: p. 165.
22. Hautojaärvi, P., Corbel, C., Dupasquier, A., Mills Jr, A.P., proceedings of: International School of Physics, Course CXXV, Italian Physical Society, Bologna, 1995.
23. Asoka-Kumar, P., Alatalo, M., Ghosh, V.J., Kruseman, A.C., Nielsen, B., Lynn, K.G., Phys. Rev. Lett., 1996. **77**: p. 2097.
24. Nagai, Y., Tang, Z., Hasegawa, M., Kanai, T., Saneyasu, M., Phys. Rev. B, 2001. **63**: p. 134110.
25. Nagai, Y., Takadate, K., Tang, Z., Ohkubo, H., Sunaga, H., Takizawa, H., Hasegawa, M., Phys. Rev. B, 2003. **67**: p. 224202.
26. Reinhart, D.E., Kumar, A. S., Gelles, D. S., Hamilton, M. L., Rosinski, S. T., proceeding of: 18th American Society for Testing and Materials, Symposium on Effects of Radiation on Materials, Philadelphia, 1999.
27. Salje, G., Feller-Kniepmeier, M., J. Appl. Phys., 1977. **84**: p. 1833.
28. Glade, S.C., Wirth, B.D., Odette, G.R., Asoka-Kumar, A., J. Nucl. Mater., 2006. **351**: p. 197.
29. Hyde, J.M., English, C.A., Lucas, G.E., Snead, L., Kirk Jr., M.A., Ellima, R.G., proceeding of: Material Research Society, Fall meeting, Symposium R: Microstructural Processes in Irradiated Material, San Francisco, 2000.

30. Miller, M.K., Russell, K.F., J. Nucl. Mater., 2007. **371**: p. 145.
31. Orthen, P.J., Jenkins, M.L., Smith, G.D.W., Phythian, W.J., Phil. Mag. Lett, 1991. **64**: p. 383.
32. Edwards, A.B., Roberts, K.J., Pizzini, S., Phythian, W.J., Phil. Mag. Lett., 1999. **79**: p. 1295.
33. Orthen, P.J., Jenkins, M.L., Smith, G.D.W., Phil. Mag. A, 1994. **70**: p. 1.
34. Cammelli, S., Degueldre, C., Cervellino, A., Abolhassani, S., Kuri, G., Bertsch, J., Lützenkirchen-Hecht, D., Frahm, R., Nucl. Instrum. Method B in press.
35. Cammelli, S., Lützenkirchen-Hecht, D., Degueldre, C., Bertsch, J., Frahm, R., J. of Phys.: Conf. Ser., 2009. **190**: p. 012027.
36. Shandiz, M.A., Phys. Lett. A 2009.
doi:10.1016/j.physleta.2008.07.011.
37. Jentys, A., Phys. Chem. Chem. Phys., 1999. **1**: p. 4059.
38. Schilling, P.J., He, J. H., Cheng, J., Ma, E., Appl. Phys. Lett., 1996. **68**: p. 767.
39. Eckert, J., Holzer, J. C., Johnson, W. L., J. Appl. Phys., 1993. **73**: p. 131.
40. Eckert, J., Holzer, J. C., Johnson, W. L., J. Appl. Phys., 1993. **73**: p. 2794.
41. Fultz, B., Ahn, C. C., Spooner, S., Hong, L. B., Eckert, J., Johnson, W. L., Metall. Mater. Trans., 1996. **27A**: p. 2934.
42. Hong, L.B., Fultz, B., Acta Mater., 1998. **46**: p. 2937.
43. Hounslow, M.J., Ryall, R.J., Marshall, V.R., AIChE J., 1988. **34**: p. 1821.
44. Lifshitz, I.M., Slyozov, V.V., J. Phys. Chem. Solid. 1961. **19**: p. 35.
45. Wagner, C., Z. Elektrochem., 1961. **65**: p. 581.
46. Ardell, A.J., Acta Metall., 1972. **20**: p. 61.

47. Wang, K.G., Glicksman, M.E., Rajan, K., *Comput. Mater. Sci.*, 2005. **34**: p. 235.
48. Cervellino, A., Giannini, C., Guagliardi, A., Ladisa, M., *Phys. Rev. B*, 2005. **72**: p. 035412.
49. Kiss, L.F., Söderlund, J., Niklasson, G. A., Granqvist, C. G., *Nanotechnology*, 1999. **10**: p. 25.
50. Victoreen, J.A., *J. Appl. Phys.*, 1948. **19**: p. 855.
51. Schütz, G., Wagner, W., Wilhelm, W., Kienle, P., Zeller, R., Frahm, R., Materlik, G., *Phys. Rev. Lett.*, 1987. **58**: p. 737.
52. Schütz, G., Frahm, R., Mautner, P., Wienke, R., Wagner, W., Wilhelm, W., Kienle, P., *Phys Rev. Lett.*, 1989. **62**: p. 2620.
53. Lee, P.A., Citrin, P.H., Eisenberger, P., Kincaid, B.M., *Rev. Mod. Phys.*, 1981. **53**: p. 769.
54. Rehr, J.J., Albers, R.C., *Rev. Mod. Phys.*, 2000. **72**: p. 621.
55. Newville, M., *J. Synchrotron Rad.*, 2001. **8**: p. 322.
56. Ravel, B., *J. Synchrotron Rad.*, 2001. **8**: p. 314.
57. Ravel, B., Newville, M., *J. Synchrotron Rad*, 2005. **12**: p. 537.
58. Beni, G., Platzmann, P.M., *Phys. Rev. B*, 1976. **44**: p. 1514.
59. Maradudin, A.A., Montroll, E.W., Weiss, G.H., Ipatova, I.P., *Theory of Lattice Dynamics in the Harmonic Approximation*, Academic, New York, 2001.
60. Sevillano, E., Meuth, H., Rehr, J.J., *Phys. Rev. B*, 1979. **20**: p. 4908.
61. Ankudinov, A.L., Nesvizhskii, A.I., Rehr, J.J., *Phys. Rev. B* 2003. **67**: p. 115120.
62. Stern, E.A., Newville, M., Ravel, B., Yacoby, Y., Haskel, D., *Physica B*, 1995. **208&209**: p. 117.
63. Stern, E.A., *Phys. Rev. B* 1993. **48**: p. 9825.
64. Bevington, P.W., *Data Reduction and Error Analysis for the Physical Sciences*, McGraw-Hill, New York, 1969.

65. Hansen, L.B., Stoltze, P., Nørskov, J.K., Clausen, B.S., Niemann, W., Phys. Rev. Lett., 1990. **64**: p. 3155.
66. Clausen, B.S., Topsøe, H., Hansen, L.B., Stoltze, P., Nørskov, J.K.; Catal. Today, 1994. **21**: p. 49.
67. Gordon, M.B., Cyrot-Lackmann, F., Desjonquères, M. C., Surf. Sci., 1979. **80**: p. 159.
68. Bazin, D., Sayers, D. A., Rehr, J. J., J. Phys. Chem., 1997. **101**: p. 11040.
69. Bazin, D., Rehr, J. J., J. Phys. Chem. B 2003. **107**: p. 12398
70. Moonen, J., Slot, J., Lefferts, L., Bazin, D., Dexpert, H., Physica B, 1995. **208&209**: p. 689.
71. JRQ: Reference manual on the IAEA JRQ correlation monitor steel for irradiation damage studies.
72. More details are available in,
<http://sls.web.psi.ch/view.php/accelerators/desc/sr/index.html>
73. Borca, C.N., Grolimund, D., Willmann, M., Meyer, B., Jefimovs, K., Vila-Comamala, J., David, C., J. Phys.: Conf Ser. 2009. **186**: p. 012003.
74. More details are available in,
<http://sls.web.psi.ch/view.php/beamlines/ms/pd/endstation/index.html>
75. Kuri, G., Cammelli, S., Degueldre, C., Bertsch, J., Gavillet, D., J. Nucl. Mater., 2009. **385**: p. 312.
76. Cammelli, S., Degueldre, C., Kuri, G., Bertsch, J., Nucl. Instrum. Method B 2008. **266**: p. 4775.
77. Cammelli, S., Degueldre, C., Kuri, G., Bertsch, J., Lützenkirchen-Hecht, D., Frahm, R., J. Nucl. Mater., 2009. **385**: p. 319.
78. Poppe, G.P.M., Wijers, C. M. J., Association for Computing Machinery, Trans. Math. Software, 1990. **16**: p. 38.
79. Prince, E., Toby, B. H., J. Appl. Cryst, 2005. **38**: p. 804.
80. Warren, B.E., Addison Wesley: Menlo Park, 1969. **13**: p. 251.

81. Harris, V.G., Kemner, K.M., Das, B.N., Koon, N.C., Ehrlich, A.E., Kirkland, J.P., Woicik, J.C., Crespo, P., Hernando, A., Escorial, A.G., Phys. Rev. B 1996. **54**: p. 6929.
82. Rehr, J.J., Leon, J.M.D., Zabinsky, S.I., Albers, R.C., J. Am. Chem. Soc., 1991. **113**: p. 5135.
83. Arokiam, A.C., Barashev, A.V., Bacon, D.J., Osetsky, Yu, N., Phys. Rev. B 2005. **71**: p. 174205.
84. Ortiz, C.J., Caturla, M.J., Phys. Rev. B 2007. **75**: p. 184101.
85. Marian, J., Wirth, B.D., Caro, A., Sadigh, B., Odette, G.R., Perlado, J.M., Diaz de la Rubia, T., Phys. Rev. B 2002. **65**: p. 144102.
86. Takahashi, A., Soneda, N., Ishino, S., Yagawa, G., Phys. Rev. B 2003. **67**: p. 024104.
87. Victoria, M., Baluc, N., Bailat, C., Dai, Y., Luppo, M.I., Schaublin, R., Singh, B.N., J. Nucl. Mater., 2000. **276**: p. 114.
88. Pythian, W.J., Stoller, R.E., Foreman, A.J.E., Calder, A.F., Bacon, D.J., J. Nucl. Mater., 1995. **223**: p. 245.
89. Caturla, M.J., Soneda, N., Alonso, E., Wirth, B.D., Diaz de la Rubia, T., Perlado, J.M., J. Nucl. Mater., 2000. **276**: p. 13.
90. Alonso, J.A., Girifalco, L.A., Phys. Rev. B, 1979. **19**: p. 3889.
91. Xu, Q., Yoshiie, T., Sato, K., Philos. Mag. Lett., 2007. **87**: p. 65.
92. Xu, Q., Yoshiie, T., Sato, K., Philos. Mag. Lett., 2008. **88**: p. 353.
93. Frahm, R., Barbee Jr., T.W., Warburton, W., Phys. Rev. B, 1991. **44**: p. 2822.
94. Miller, M.K., Nanstad, R.K., Sokolov, M.A., Russel, K.F., J. Nucl. Mater, 2006. **351**: p. 216.
95. Golubov, S.I., Osetsky, Yu. N., Serra, A., Barashev, A.V., J. Nucl. Mater., 1995. **226**: p. 252.
96. Miller, M.K., proceeding of: The Minerals, Metals & Materials Society, Annual Meeting, San Francisco, 2005.

97. Monzen, R., Jenkins, M.L., Sutton, A.P., Philos. Mag. A, 2000. **80**: p. 711.

9. Variable indexes and symbols

Symbol	Unit	
A	mol^{-1}	Avogadro constant (6.022×10^{23})
d_0	nm	Diameter of the smallest cluster taken in account (0.3nm)
d_i	nm	Diameter of the i^{th} cluster
T_{DBT}	K	Ductile to brittle transition temperature
D_{max}	nm	Maximum distance in a cluster according to the “maximum separation method” see 3.1.3
E_0	eV	Threshold energy
$E_0^{M_i}$	eV	Threshold energy of M_i
$ F_i(k) $	-	Modulus of the backscattering amplitude of the i^{th} shell
I	s^{-1}	Intensity of the beam detected in the second ionic chamber
I_0	s^{-1}	Intensity of the beam detected in the first ionic chamber
k	\AA^{-1}	Wave number
$\mu(E), \mu(k)$	μm^{-1}	Absorption coefficient in function of energy, wave vector
ℓ	μm	Thickness of a sample
N_i	-	Number of atoms in the i shell
N_{M_i, M_j}	-	Number of atoms M_i and M_j in the first and second shell
N_{at}	-	Number of atoms in a cluster
n_i	$\text{nm}^{-1} \text{m}^{-3}$	Size normalized cluster concentration
$n_{M_0}^{bcc}$	-	Fraction of the number of M_0 atoms in bcc phase
$n_{M_1}^{bcc}$	-	Fraction of the number of M_1 atoms in bcc phase
$n_{M_0}^{fcc}$	-	Fraction of the number of M_0 atoms in fcc phase
$n_{M_1}^{fcc}$	-	Fraction of the number of M_1 atoms in fcc phase
m_i	g	Mass of the i^{th} cluster
\mathcal{M}		Molecular weight of a compound
\mathcal{M}_{M_i}		Molecular weight of M_i
r_i	\AA	Modulus of the distance \bar{r}_i between absorber and i^{th} shell atoms
s_{min}	-	Minimum number of atoms used to define a cluster see 3.1.3
S_0^2	-	Amplitude reduction factor
t	s	Time
V_i	nm^3	Volume of the i^{th} cluster
V_0	nm^3	Volume of the smallest cluster taken in account (~ 0.014)
$u(r_0)$	\AA	Displacement vector of the absorber
$u(r_i)$	\AA	Displacement vector of an atom at a distance of r_i from absorber
x	-	Fraction of M_0 atoms in the first shell
y	-	Fraction of M_0 atoms in the second shell
Z	-	Atomic number
Z_{M_i}	-	Atomic number of the element M_i
α	\AA^{-2}	Scaling factor see: 3.1.1

$\chi(E)$	-	EXAFS signal in function of energy. See 3.2.1
$\delta_i(k)$	rad	Central atom partial phase shift of the final state
$\lambda(k)$	Å	Mean free path of the photoelectron
ρ_{Cl}	g cm ⁻³	Cluster density in the sample
ρ	g cm ⁻³	Mass density
σ_i	Å	Mean square relative displacement of the i shell
$\Omega(E)$	cm ⁻²	Cross section

Acronyms

APT	Atom Probe Tomography
CEA	Commissariat à l'Énergie Atomique
DBTT	Ductile to Brittle Transition Temperature
DC	Displacement Cascade
DPA	Displacements Per Atom
DW	Debye Waller
EDS	Energy Dispersive x ray Spectrometry
EXAFS	Extended X ray Absorption Fine Structure
FNR	Ford Nuclear Reactor
FT	Fourier Transform
FZK	Forschungszentrum Karlsruhe
HI	Hot Irradiated (irradiated in the reactor)
I	Irradiated (sample)
IA	Irradiated and Annealed (sample)
IAEA	International Atomic Energy Agency
IAR	Irradiated, Annealed and Re-irradiated (sample)
IARA	Irradiated, Annealed, Re-irradiated and re-Annealed (sample)
JRQ	Japanese Reference Quality, see Ref [71]
LCF	Linear Combination Fit
SRMA	Service de Recherches Métallurgiques Appliquées (CEA)
LNM	Laboratory for Nuclear Materials
KKG	Kernkraftwerk Gösgen
ORNL	Oak Ridge National Laboratory
PAS	Positron Annihilation Spectroscopy
PKA	Primary Knock-on Atom
PSI	Paul Scherrer Institut
RDF	Radial Distribution Function
REF	Reference (sample)
RPV	Reactor Pressure Vessel
RT	Room Temperature
SANS	Small Angle Neutron Scattering
SCK-CEN	Studiecentrum voor Kernenergie – Centre d'Etude de l'énergie Nucléaire
SLS	Swiss Light Source
TEM	Transmission Electron Microscopy

XRD	X-Ray Diffraction
XAFS	X-Ray Absorption Fine Structure
XANES	X-Ray Absorption Near Edge Spectroscopy
XAS	X-Ray Absorption Spectroscopy

10. Acknowledgements

First acknowledgements go necessarily to Prof. Dr. Claude Degueldre and Dr. Johannes Bertsch at the Paul Scherrer Institute, who have followed me for three years in a manner that I could not wish for better. I need also to thank them for the time they have always found for me and for this project to optimize efforts and results. Although the distances do not help, I am very glad of having worked with Prof. Dr. Ronald Frahm and Dr. Dirk Lützenkirchen-Hecht from Wuppertal University because it has been a privilege to learn and to work with such high competent scientists and their help has been invaluable. During these three years I had the possibility to work with many others people at PSI. They have taught me many things and, without their help, this work would be much poorer. So I am happy to thank: Dr. Annick Froideval, Dr. Goutam Kuri, Dr. Sousan Abolhassani and Dr. Antonio Cervellino. Moreover precious help came from Dr. Daniel Grolimund, Dr. Camelia Borca, Dr. Stefan Mangold, Dr. Manuel Pouchon, Eugenia Minikus, Andrej Bullemer, Matthias Martin, Robert Zubler, Christian Proff and all the LNM (LWV...).

Finally I would like to thanks all the friends who made these three years at PSI much funnier: Christian, Per, Matthias, Paul, Fatima, Andrej, Hagreeva, the huge Greek, Italian and Polish communities...

Last but not least, those who helped me for *everything else*: Matteo & Marta, Guido, Salvatore & Hanna, Giovanni, Costanza, Fabio, Ilaria, Marco, Atzuko, Teodoro, Ludovica, Ana, Agi and all the "Züriker".

Of course I cannot forget the swissnuclear for having supported the project.

Publications:

[6] In press.

[1] F. Loglio; M. Innocenti; A. M Telford; E. Salviotti; G. Pezzatini; **S. Cammelli**; F. D'Acapito; R. Felici; A. Pozzi; M. L. Foresti: *Ternary Cd_xZn_{1-x}Se nanocrystals deposited on Ag(111) by ECALE: AFM and EXAFS Characterization*, *Electrochimica Acta*, 53, (2008), 6978-6987;

[2] **S. Cammelli**, C. Degueldre, G. Kuri, J. Bertsch; *Study of a neutron irradiated reactor pressure vessel steel by X-ray absorption spectroscopy*, *NIM B* 266 (2008) 4775–4781;

[3] **S. Cammelli**, C. Degueldre, G. Kuri, J. Bertsch, D. Lützenkirchen-Hecht, R. Frahm, *Study of atomic clusters in neutron irradiated reactor pressure vessel surveillance samples by extended X-ray absorption fine structure spectroscopy*, *J of Nucl Mater* 385 (2009) 319–324;

[4] G. Kuri, **S. Cammelli**, C. Degueldre, J. Bertsch, D. Gavillet, *Neutron induced damage in reactor pressure vessel steel: An X-ray absorption fine structure study*, *J. of Nucl. Mater.* 385 (2009) 312–318;

[5] **S. Cammelli**, D. Lützenkirchen-Hecht, J. Bertsch, C. Degueldre, R. Frahm; *Polydispersity and EXAFS simulations*, *Journal of Physics: Conference Series*, 190, (2009) 012027.

[6] **S. Cammelli**, C. Degueldre, A. Cervellino, S. Abolhassani, G. Kuri, J. Bertsch, D. Lützenkirchen-Hecht, R. Frahm, *Cluster formation, evolution and distribution in FeCu alloy: analysis by XAS, XRD and TEM*. NIMB from Symposium R, EMRS 2009. In press.